

Diffusion Tensor Imaging of Myelin Water

by

Alexandru Vlad Avram

Department of Biomedical Engineering
Duke University

Date: _____

Approved:

Allen W. Song, Supervisor

Chunlei Liu

Gregg Trahey

Craig Henriquez

Jeffrey Petrella

Dissertation submitted in partial fulfillment of
the requirements for the degree of Doctor of Philosophy in the Department of
Biomedical Engineering in the Graduate School
of Duke University

2011

ABSTRACT

Diffusion Tensor Imaging of Myelin Water

by

Alexandru Vlad Avram

Department of Biomedical Engineering
Duke University

Date: _____

Approved:

Allen W. Song, Supervisor

Chunlei Liu

Gregg Trahey

Craig Henriquez

Jeffrey Petrella

An abstract of a dissertation submitted in partial
fulfillment of the requirements for the degree
of Doctor of Philosophy in the Department of
Biomedical Engineering in the Graduate School
of Duke University

2011

Copyright by
Alexandru Vlad Avram
2011

Abstract

In recent years, the emergence of diffusion tensor imaging (DTI) has provided a unique means via water diffusional characteristics to investigate the white matter integrity in the human brain, and its impact on neuronal functions. However, since the characterization of white matter integrity using DTI often lacks tissue specificity, most research studies report changes in anisotropy that are not explicitly correlated with particular cellular origins. To improve the utility of DTI in translational neuroimaging, it is critical to develop DTI acquisition techniques that are quantitative and tissue specific.

There are, nevertheless, existing methods for tissue specificity. For example, myelin water images can be generated using multiple echo time (TE) or magnetization transfer techniques. These techniques can detect changes in the concentration of myelin associated markers, but not in their spatial organization. Most white matter pathologies however start with early microstructural changes in the myelin sheaths during which the tissue contents remain similar and are thus not differentiable on a conventional MR image. Thus, the ability to construct a diffusion tensor that is myelin specific can have an immediate impact on our better understanding myelin physiology and pathophysiology during brain development.

Unfortunately, the myelin water signal decays rapidly because of its short transverse relaxation time constant ($T_2 < 50$ ms), especially in DTI experiments where

the echo time (TE) can be as large as 100ms. Even in special cases where the TE is shorter, the lack of myelin selectivity in conventional DTI techniques makes assessment of myelin microstructure extremely challenging. Thus we need to develop a DTI methodology that will greatly shorten the TE and allow myelin selectivity.

To preserve more signal from myelin water we shortened the echo time in DTI by using a stimulated echo (STE) diffusion encoding scheme. In our initial approach we integrated the STE-DTI sequence with magnetization transfer (MT) preparation to achieve additional differentiating sensitization to myelin water and derive a myelin water weighted (MWW) diffusion tensor. Our results indicate that, compared to conventional diffusion tensor, MWW-DTI has the same principal diffusion direction (parallel to the fiber orientation), but larger fractional anisotropy (FA) due to significantly smaller radial diffusivity. The limited myelin water specificity and high radio frequency (RF) power deposition of MT-DTI can however restrict its applicability to certain clinical populations.

To improve sensitivity to myelin water we minimized the echo time by implementing a segmented spiral readout trajectory for the STE-DTI sequence. We integrated reconstruction strategies for inherently and dynamically correcting both shot-to-shot motion induced phase errors and off-resonance effects due to magnetic field inhomogeneities (including eddy currents) to obtain images with high spatial accuracy and excellent signal-to-noise ratio (SNR). We conducted an unprecedented multi-TE DTI

experiment in vivo, collecting diffusion tensor images at multiple echo times (as short as 18ms) and characterized the dependence of diffusion anisotropy on white matter T_2 components (e.g. myelin water) thereby confirming the diffusion characteristics of myelin water previously observed using MT-DTI.

Building on this improved understanding, we designed an integrated MWW-DTI solution for clinical examinations based on the simultaneous acquisition of two DTI images at different echo times. It is hoped that the new MWW-DTI methodology will find wide applications to investigate the origins of many myelin and white matter pathologies in pediatric brain disorders or to allow early detection of myelin microstructural changes in demyelination diseases in adults (e.g. multiple sclerosis).

Dedication

The author wishes to dedicate this dissertation to his parents

Elisabeta Avram

Iancu Gheorghe Avram

Contents

Abstract	iv
List of Tables	xii
List of Figures	xiii
Acknowledgements	xviii
Chapter 1: Emergence of Diffusion Tensor Imaging for studying white matter microstructure	1
1.1 Microscopic Brownian motion.....	1
1.2 The diffusion coefficient	4
1.3 The Bloch Equations.....	7
1.4 The magnetic relaxation time constants	11
1.5 Spatial encoding in MRI	15
1.6 The NMR diffusion experiment	17
1.7 Diffusion Tensor Imaging	21
1.7.1 The emergence of DTI for studying white matter changes	25
1.7.2 Advanced DTI methods	28
1.7.3 Limitations of DTI and the need for increased tissue specificity.....	30
Chapter 2: Importance of Imaging Myelin Microstructure and Strategies for Myelin Specific DTI.....	32
2.1 The role of myelin in neuronal signaling	32
2.1.1 Myelin microstructure	34
2.1.2 The function of myelin in nerve electrophysiology.....	37

2.2 Changes in myelin microstructure during neurological disorders of white matter origin and normal brain development	38
2.3 Myelin Imaging.....	40
2.3.1 Strategies for Myelin Contrast Imaging in MRI.....	42
2.4 Need and feasibility of myelin specific DTI in developmental and translational neuroimaging.....	45
2.5 Significance of myelin specific DTI in neurological disorders of white matter origin and normal brain development	47
Chapter 3: Initial effort toward myelin specific DTI using Magnetization Transfer preparation and stimulated echo.....	50
3.1 Reducing the echo time in DTI using stimulated echo	50
3.2 Sensitizing DTI to myelin water using magnetization transfer	53
3.3 Pulsed Magnetization Transfer for in vivo Myelin Water Weighting	56
3.4 Magnetization Transfer prepared stimulated echo DTI pulse sequence.....	60
3.5 Processing strategy for robust Myelin Water Weighted (MWW) DTI.....	62
3.6 In vivo myelin water weighted (MWW) DTI has larger diffusion anisotropy compared to conventional DTI.....	63
3.7 Myelin Water Weighted DTI can better differentiate between WM lesions in multiple sclerosis patient.....	69
3.8 Need for Improved Specificity and Increased Sensitivity	72
Chapter 4: Technical development of short-TE Diffusion Tensor Imaging for clinical applications.....	75
4.1 Minimizing echo time using a spiral-out readout trajectory.....	75
4.2 Inherent motion correction in high resolution DTI using self-navigated interleaved spiral (SNAILS) acquisition.....	78

4.3 Magnetic field inhomogeneities and gradient eddy currents degrade DTI images	81
4.4 Integrated solution for short-TE DTI using Stimulated Echo SNAILS DTI with dynamic and inherent correction for motion and field inhomogeneities.....	85
4.5 Image reconstruction using simultaneous motion and off-resonance correction .	89
4.6 Short-TE DTI with high spatial resolution and accuracy	92
4.7 Short-TE DTI as a new clinical tool for analyzing diffusion anisotropy of T ₂ components of white matter	97
Chapter 5: Characterizing the TE dependence of white matter diffusion anisotropy in vivo.....	99
5.1 Myelin water diffusion in animal specimen and the need for in vivo human WM studies	100
5.2 Cardiac Gated multi-TE DTI pulse sequence with a wide range of short TEs	102
5.3 In vivo multi-TE DTI reveals changes in anisotropy at short echo times.....	104
5.4 Partial volume effects and the need for T ₂ spectrum analysis	108
5.5 Robust T ₂ spectrum analysis of diffusion tensor images	110
5.5 White matter T ₂ spectrum analysis confirms larger diffusion anisotropy of myelin water.....	115
5.6 Need and feasibility of myelin water sensitization for clinical DTI applications	118
Chapter 6: Integrated and efficient myelin water weighted (MWW) DTI using a two-TE acquisition.....	121
6.1 Myelin water weighted DTI using two images with different echo times.....	121
6.2 Efficient acquisition of myelin water weighted DTI for clinical applications	124
Chapter 7: Conclusions and Future Work	130
7.1 Short-TE DTI for investigating diffusion anisotropy of myelin water	130

7.3 Integrating short-TE DTI with advanced diffusion models	131
7.2 Limitations of myelin water weighted DTI	132
7.4 Monitoring myelination during healthy brain development.....	134
Appendix A: Glossary of Terms	136
References	142
Biography	167

List of Tables

Table 1: Myelin water weighted diffusion tensor obtained using the magnetization transfer prepared stimulated echo DTI sequence can better differentiate between white matter lesions (LP - left posterior, RP - right posterior, LA - left anterior) in multiple sclerosis..... 71

Table 2: Average diffusion characteristics calculated over a region of 1,452cm³ of white matter containing the major fibers 117

List of Figures

- Figure 1: Carr-Purcell-Meiboom-Gill (CPMG) pulse sequence for measuring T_2 's of substances. A train of 180 pulses is applied to repetitively refocus the signal and reduce diffusion effects due to inherent magnetic field inhomogeneities..... 14
- Figure 2: Pulse sequence diagram showing a Stejskal-Tanner diffusion weighted pulse gradient spin echo (PGSE) pulse sequence with echo-planar imaging EPI readout, which uses two identical gradient pulses on either side of a refocusing pulse. The diffusion sensitization (Equation 1.22) is a function of the duration δ and amplitude G of the gradient pulses, as well as their separation Δ 19
- Figure 3: Pulse sequence diagram for a stimulated echo based diffusion weighted pulse sequence with EPI readout. The pulsed gradient stimulated echo (PGSTE) diffusion encoding scheme significantly can increase the diffusion time allowing for larger diffusion sensitization, or b-value. 21
- Figure 4: Eigenvalue decomposition of diffusion tensor. For every voxel, the diffusion tensor can be decomposed along three orthotropic axes related to the underlying tissue orientation. 22
- Figure 5: Microanatomy of white matter. A. Myelin is formed as an extension of the oligodendrocyte bi-lipid plasma membrane tightly wrapping around the axons (credit Steven Gschmeissner / Science Photo Lab). B. The complex white matter microstructure makes it difficult to disentangle diffusional changes of myelin (pink) or axonal (yellow) origins using conventional diffusion tensor techniques. 35
- Figure 6: A. Electron microscopy image of myelin microstructural changes adapted from (Novak et al., 2011). B. The spacing between adjacent layers of myelin is determined by the electrostatic interaction between myelin proteins and lipids adapted from (Min et al., 2009). Conventional myelin contrast MR imaging can investigate changes in myelin content, but are not sensitive to the gradual loosening of myelin layers (A) associated with early stages of demyelination pathologies. 37
- Figure 7: Comparison of minimum achievable echo time dependence on diffusion sensitization for clinical twice refocused spin echo (TRSE) EPI (black) and stimulated echo (STE) EPI (red) pulse sequences. A maximum gradient amplitude of 5 G/cm and slew rate of 120 T/m/s were used. For the stimulated echo the mixing period of T_M was

120ms. For the EPI readout, a 12 ms delay from the beginning of the acquisition window was used..... 52

Figure 8: Pulse sequence schematics for the magnetization transfer prepared stimulated echo DTI. Spatially non- selective Fermi-shaped MT pulse is played out with a repetition time of 300ms in a multi-slice stimulated echo acquisition with diffusion weighting; TE/TM/TR = 34/135/4500 ms, 15 slices, $b = 600 \text{ sec/mm}^2$. The colors correspond to the MT crushers (blue), diffusion encoding (red), slice selection (green) and readout (orange) gradients. A spatial-spectral pulse (not shown here) was used for excitation..... 57

Figure 9: Pulse sequence schematics for the magnetization transfer prepared stimulated echo DTI. Spatially non- selective Fermi-shaped MT pulse is played out with a repetition time of 300ms in a multi-slice stimulated echo acquisition with diffusion weighting; TE/TM/TR = 34/135/4500 ms, 15 slices, $b = 600 \text{ s/mm}^2$. The colors correspond to the MT crushers (blue), diffusion encoding (red), slice selection and readout (orange) gradients. A spatial-spectral pulse (not shown here) was used for excitation. 61

Figure 10: In white matter tracts, the main directions of diffusion are similar for the TRSE-DT (A), the STE-DT (B), and the Myelin Weighted Water tensor (C). Due to the very small MT effect in regions of the ventricles with large CSF partial volume, the MWW tensor was derived from very low signal levels and therefore the FA values for these regions exhibit large variations as shown. 64

Figure 11: Fractional anisotropy and radial diffusivity ($\mu\text{m}^2/\text{ms}$) maps for white matter. Top row FAs, bottom row radial diffusivities (from left to right TRSE-DT, STE-DT, and MWW tensor respectively). MWW diffusion tensor shows larger FA, mainly due to a significantly smaller radial diffusivity..... 65

Figure 12: FA and Radial diffusivity along a path through the splenium of corpus callosum. Myelin water tensor (red) shows larger FA and smaller radial diffusivity than the either STE DTI tensor (green) or clinical DSE DTI tensor (blue) 67

Figure 13: Myelin Water Weighted Diffusion Tensor Imaging in Multiple Sclerosis patient. Three lesions - left posterior (LP), right posterior (RP) and left anterior (LA) - shown in blue, cyan and yellow respectively, as well as normal appearing white matter (NAWM) in red were identified based on the T2W and MTR (A) maps. The colored FA maps for MWW-DTI (C) shows more heterogeneity across lesions, when compared to the colored FA of the conventional DTI (B), suggesting that the MWW-DT might provide a better characterization of WM lesions in multiple sclerosis (MS)..... 70

Figure 14: A. Minimum echo time achievable with twice refocused spin echo (TRSE) EPI DTI (black) and STEAM spiral DTI (red). B. Theoretical normalized white matter SNR comparison between the clinical TRSE EPI DTI and STEAM spiral DTI. For STEAM spiral DTI the duration of the longitudinal period was assumed to be 120 ms, while for TRSE EPI DTI a 14 ms echo delay from the end of diffusion encoding was used to accommodate for the partial Fourier acquisition. Standard gradient hardware parameters were assumed: maximum gradient strength= 50 mT/m, maximum slew rate= 200 T/m/s 77

Figure 15: Analytical design of a self-navigated spiral trajectory (Kim et al.). α is a parameter for controlling the change in density, n the number of turns, $\lambda = N/(2 \cdot FOV)$, sm is the maximum slew rate, gm the maximum gradient amplitude; $Ts2a$ the transition time from slew rate limited to amplitude limited region, and Tes is the time to end of slew rate limited trajectory. The trajectory is rotated by an angle $\theta = 2\pi/NL$ in order to acquire NL interleaves..... 80

Figure 16: STEAM DTI pulse sequence with inherent and dynamic field-map acquisition. Non-spatially selective fat suppression module (blue) precedes slice excitation. Diffusion weighting gradients (purple) cause identical eddy current during the SE and STE readouts. Crusher gradients (green) also act to replicate the same eddy current profile for both STE and SE readouts..... 87

Figure 17: Simultaneous inherent motion and off-resonance correction image reconstruction pipeline. Phase images reconstructed from the symmetric (A1) and asymmetric spin echo (A2) acquisitions are subtracted to obtain a field map (B) which is interpolated (C) and segmented into different bins (D) corresponding to small frequency ranges (~3Hz). The individual readouts acquired on the stimulated echo diffusion weighted pathways are demodulated at each mean bin frequency and gridded on to a 2x oversampled Cartesian grid (E). The inherent oversampled navigator data (F) is used to reconstruct a low resolution full FOV image (G) which is removed from the corresponding interleaf (H) prior to summation. The motion corrected images reconstructed at each demodulation frequency (I) are multiplied by their corresponding frequency masks (D). Following summation across all frequency bins, the motion and off-resonance corrected image (J) is obtained. 91

Figure 18: Top row: field maps acquired dynamically for the baseline image (A) and three diffusion weighted images (B-D) acquired with different orientations. Bottom row: Corresponding eddy current profile estimations (E-H) calculated by subtracting the field

map (A) corresponding to the baseline image from corresponding to the diffusion weighted images (B-D)..... 93

Figure 19: Top row: Baseline (A) and diffusion weighted images (B, C) acquired with STEAM SNAILS DTI and reconstructed with motion correction. Bottom row: The same images (D, E, and F respectively) after simultaneous motion and off-resonance correction with inherently acquired field maps. Local blurring artifacts (yellow arrows) are specifically corrected for each image individually to remove diffusion weighting direction dependent distortions caused by eddy currents..... 94

Figure 20: Fractional Anisotropy (FA) maps with principal diffusion orientation color-coding for three slices. Top row: images reconstructed with motion correction only (A, B, C). Bottom row: images reconstructed with simultaneous motion and off-resonance correction (D, E, F). 95

Figure 21: Schematic representing the pulse sequence diagram for the cardiac gated multi-TE sequence. using a uniform density spiral readout trajectory to acquire images in a single shot. For every TR, by increasing the intervals $\Delta TE/2$ (marked red) the effective echo time is incremented without changing the diffusion sensitization (same diffusion encoding parameters Δ , δ , and G) or the duration of longitudinal relaxation (T_M interval). To ensure consistent voxel composition, looping over echo times was nested inside the loop across different diffusion encoding directions..... 103

Figure 22: FA dependence on echo time. The abrupt decrease of FA in the short TE range from 22ms to 52ms, can be attributed to the diminishing contribution from short T_2 component. Assuming T_2 water components have the same preferred diffusion direction, the FA decreases in the short TE range implies that myelin water has larger anisotropy compared to other white matter T_2 components. At larger echo times, the FA appears to plateau and the measurements become more noisy due to decreasing SNR. 105

Figure 23: Dependence of radial diffusivity on echo time. The increase of radial diffusivity in the short TE range from 22ms to 52ms follows closely the decrease of FA observed in Fig. 22. For larger echo times the radial diffusivity increases slightly, probably due to decreasing SNR. 107

Figure 24: Normalized signal weighting due to transverse relaxation across the T_2 spectrum for images acquired with TE1=22ms (blue), TE2=72ms (black) and the difference signal of these two acquisitions (red) showing increased myelin water ($T_2 < 50ms$) weighting. 122

Figure 26: Pulse sequence diagram for rapid myelin water weighting DTI. Two diffusion weighted images with different TEs are acquired simultaneously ($TE_1=TE$, $TE_2=TE+\Delta TE$). The difference between them can be used to calculate a short T_2 weighted diffusion tensor. Simultaneously, an inherent field map is acquired dynamically from two acquisitions along a secondary coherence pathway with dTE duration of phase accumulation. 123

Figure 26: Fractional anisotropy maps with principal diffusion orientation color-coding overlay for the DTI images acquired with short $TE_1=22ms$, (A) and with clinical $TE_2=72ms$ (B) and the Myelin water weighted (MWW) diffusion tensor (C) computed based on the two DTI acquisitions with different echo times. As expected, all tensors show identical preferred direction of diffusion..... 125

Figure 27: Fractional anisotropy (top row) and radial diffusivity (bottom row) comparison between DTI acquired with short $TE_1=22ms$ (A,D), DTI acquired with clinical $TE_2=72ms$ (B,E) and Myelin water weighted (MWW) DTI (C,F) computed based on the two acquisitions with different echo times. The MWW diffusion tensor has significantly large FA due to a smaller radial diffusivity, suggesting that the diffusion of water between the myelin sheaths is more anisotropic compared to that of axonal/intercellular water. 127

Figure 28: Timeline of myelination in healthy human brain adapted from (Baumann and Pham-Dinh, 2001). Maturation of cognitive abilities occurs in synchrony with myelination of corresponding white matter pathways. 135

Acknowledgements

I could not have completed my Ph.D. without the unwavering support of my advisors, colleagues, family and friends. I am sincerely grateful for everyone who has helped me.

Firstly, I would like to thank my advisor Dr. Allen Song, for his leadership and guidance over the last five years. He granted me the freedom to explore different projects, encouraged me to become an independent researcher, helped me stay focused when necessary.

I am deeply indebted to Dr. Chunlei Liu for inspiring me to pursue diverse projects and for his persistent support in my professional career. I will always cherish our long scientific discussions after hours. I would also like to extend my gratitude to the other members of my dissertation committee: Dr. Craig Henriquez, Dr. Gregg Trahey and Dr. Jeffrey Petrella for their encouragement and sincere interest in my work. The dissertation would have been very different without their critiques, suggestions and reviews.

I am grateful to Dr. Nan-kuei Chen and Dr. Trong-Kha Truong for collaborations that have expanded my MRI expertise, and for helpful discussions during lab meetings. I would also like to thank my fellow graduate students and post-docs in our neuroimaging core at the Brain Imaging and Analysis Center (BIAC): Arnaud Guidon, Anastasia Batrachenko, Dr. Wei Li, Dr. Bing Wu, Dr. Ming-Long Wu, Dr. Bin Chen, Dr.

Hua Guo, Pooja Gaur and PeiHsin Wu. I will always appreciate their enthusiasm during late night scanning sessions, their assistance with pediatric subjects and their help with pulse sequence programming, scanner issues, and computer problems.

Apart from my colleagues and friends at BIAC, I am also grateful to the faculty members of the Biomedical Engineering (BME) Department who have taught me the excitement of interdisciplinary research. Specifically, I would like to thank Dr. Nenad Bursac, Dr. David Katz and Dr. Craig Henriquez for allowing me to assist them on teaching their courses on bioelectricity and biological transport mechanisms. I would also like to thank Kathy Barbour (BME), Amanda Griffin (BIAC) and Coleen Payne (BIAC) for helping me file paperwork and meet various deadlines throughout graduate school.

I am grateful to my collaborators at the Duke University Medical Center: Dr. Jeff Petrella, Dr. Helen Egger and Dr. Mohamad Mikati for their reviews and enthusiasm in setting up clinical studies which are currently underway.

Last but not least I would like to thank my mother Elisabeta, my father Iancu, my twin brother Sorin, and my girlfriend Sarah for their emotional support and encouragements.

Chapter 1: Emergence of Diffusion Tensor Imaging for studying white matter microstructure

The purpose of this chapter is to briefly review the physical principles necessary for understanding diffusion magnetic resonance imaging (MRI) and to discuss the clinical applicability of diffusion tensor imaging (DTI) for studying white matter changes in the human brain. The chapter begins with a brief summary of the historical developments of understanding diffusion at the microscopic (Brownian motion) and macroscopic (Fick's laws) scales. The following sections describe the physical basis of tissue contrast in MRI (T_1 and T_2 magnetic relaxation time constants), the use of gradients for spatial encoding and diffusion sensitization, and the basic DTI methodology for analyzing tissue anisotropy. The last sections discuss the limitations of DTI in tissue specificity and establish the need for development of novel acquisition methods to improve neuronal specificity.

1.1 Microscopic Brownian motion

In 1828 Scottish botanist Robert Brown provided a detailed account on the jittery motion of pollen grains floating in water, observed under a microscope (Brown, 1828). He initially presumed that the incessant irregular oscillatory motion was due to an unknown "living" force acting on the pollen grains long after the death of the plant. However, after replicating the findings using inorganic colloidal particles, he concluded that this motion - which came to be known as "Brownian Motion" - was a fundamental

characteristic of all particles in solution. A mathematical justification for the ubiquitous erratic motion was drafted decades later, with the development of the kinetic-molecular theory of matter and of a statistical understanding of thermodynamics.

The first investigations on the internal frictional forces of fluids can be traced back to 1850, when Sir George Gabriel Stokes, studying the motion of objects immersed in liquids, found that the frictional force (drag) acting on a spherical particle is proportional to the size of the particle, its velocity, and the viscosity of the medium (Stokes, 1850). While this formulation related the macroscopic measure of viscosity to the internal frictional forces inside the liquid, it did not provide any hint as to the driving force behind the random Brownian motion at the microscopic scale.

During the last half of the 19th century, physicists attempted to articulate mechanical models of the theory of heat transport based on the ballistic motion of colliding small particles obeying Newtonian mechanics (Clausius, 1857, 1862). In 1866, James Clerk Maxwell provided a statistical approach to the kinetic theory of gases by relating the temperature of a gas to the velocity distribution of its constituent gas molecules (Maxwell, 1867). Ludwig Boltzmann later generalized Maxwell's velocity distribution of particles in the presence of external forces (Boltzmann, 1875) and formulated the logarithmic connection between entropy and the number of possible microstates corresponding to a given macroscopic state of the system (Boltzmann, 1877). These developments consolidated the understanding of entropy and encouraged

physicists to postulate universal energy metrics describing the general natural tendency of physical systems (Gibbs, 1873).

Despite the compatibility of the new kinetic theory of gasses with the law of conservation of energy (1st law of thermodynamics), its foundation on the time-reversible laws of Newtonian motion at the microscopic level appeared to contradict the irreversibility of heat transfer (2nd law of thermodynamics). This paradox was resolved by Ludwig Boltzmann who demonstrated that, at the macroscopic scale, the irreversibility of heat transport can arise from the *statistical* behavior of numerous mechanical particles. By the end of the century scientists excluded the possibility of external forces driving random particle motion and began to view Brownian motion as the very manifestation of the statistical, rather than absolute nature of the 2nd law of thermodynamics (Gouy, 1889).

Building on this statistical interpretation of microscopic motion, in 1905, Albert Einstein formulated for the first time an experimentally testable hypothesis for the molecular-kinetic theory of matter. He argued that colloidal particles move erratically due to molecules in solution imparting their kinetic energy through random collisions (Einstein, 1905). By equating the osmotic pressure of colloidal particles to Stoke's force of friction, Einstein was able to relate the diffusion coefficient to particle size and the viscosity of the solution. He further used a heuristic approach to predict the linearity

between the mean square displacement $\langle \Delta x^2 \rangle$ and diffusion time τ , thus providing a separate method for experimentally measuring the diffusion coefficient D .

$$\langle \Delta x^2 \rangle = 2\tau D \quad (1.1)$$

The same relation between the diffusion coefficient and mean square displacement was obtained independently by Marian von Smoluchowski (von Smoluchowski, 1906) and a few years later by Paul Langevin (Langevin, 1908), using different derivations. This relation was verified experimentally in 1909, by French scientist Jean Baptiste Perrin who carried out meticulous experiments confirming Einstein's predictions and proving the molecular nature of matter (Perrin, 1908).

While Einstein's hypothesis established a concrete connection between Brownian motion at the microscopic scale and macroscopic diffusion, the latter process had been understood in a phenomenological sense decades earlier. Studying the transport of gases through liquid membranes, Adolf Fick arrived at a simple law that linearly relates the macroscopic concentration gradient to the flux of gas molecules. In the following section we derive Fick's law of diffusion using a thermodynamic argument to illustrate the relation of the diffusion coefficient to the microscopic parameters characterizing Brownian motion.

1.2 The diffusion coefficient

If we consider a closed system consisting of a large number of chemically non-interacting particles freely moving in a container of volume V , at a fixed temperature T ,

then the incremental change in the Gibbs free energy can be written in terms of the entropy S , and incremental pressure dP :

$$dG = -SdT + VdP \quad (1.2)$$

Using the ideal gas law $PV = nRT$ for an isothermal process, we can integrate with respect to pressure:

$$\Delta G = \int_{P_0}^P \frac{nRT}{P} dP = nRT \ln \frac{P}{P_0} \quad (1.3)$$

where R is the gas constant, n is the number of moles and T is the absolute temperature in degrees Kelvin. Defining the concentration as $C = P/P_0$, we can derive the molar chemical potential as:

$$\Delta\mu = \mu_0 + \Delta\mu = \mu_0 + \frac{\Delta G}{n} = \mu_0 + RT \ln C \quad (1.4)$$

where μ_0 is the molar Gibbs free energy at standard pressure of 1 atm.

The average force acting on a single particle in our isothermal closed system (with constant V and T) can then be expressed with respect the gradient of the chemical energy potential:

$$\mathbf{F} = \frac{-\nabla\mu}{N_A} = -\frac{RT\nabla(\ln C)}{N_A} = -k_B T \frac{\nabla C}{C} \quad (1.5)$$

Using Stoke's law, we can obtain a similar expression for the average drag (frictional) force acting on a spherical particle of radius r , moving through a medium of viscosity η with velocity \mathbf{v} : $\mathbf{F}_f = -6\pi r\eta\mathbf{v}$ (Stokes, 1850). By Newton's second law, the (spatial and temporal ensemble) average driving and frictional forces acting on the

particles must be opposite. If that were not the case, the particles would accelerate persistently, eventually violating the thermodynamic equilibrium. Equating the forces we can get an expression for the velocity:

$$\mathbf{v} = -\frac{1}{6\pi r\eta} \frac{RT}{N_A C} \nabla C = -\frac{D}{C} \nabla C \quad (1.6)$$

where the diffusion coefficient D was introduced. This derivation is still valid even for non-spherical particles, as long as the friction force is proportional to the velocity of the particle. Introducing the particle flux, we obtain the expression of Fick's law (Fick, 1855b, a)

$$\mathbf{J} = C\mathbf{v} = -D\nabla C \quad (1.7)$$

Fick's second law can be obtained by applying the continuity theorem (conservation of mass) at each point

$$\frac{dC}{dt} = -\nabla \cdot \mathbf{J} = D\nabla^2 C \quad (1.8)$$

where ∇^2 is the laplacian operator.

Fick originally postulated these laws by simply assuming linearity between the transport velocity and the concentration gradient, in a manner analogous to other transport laws formulated during the same period by Georg Simon Ohm for charge transport (Ohm, 1827) or Jean Baptiste Joseph Fourier for heat transport (Fourier, 1822). This remarkable similarity underlines the general applicability of Fick's laws to many diffusion problems in condensed physics, regardless of the specific properties of the solvent/solute system.

In particular, Fick's laws can be used to describe the self-diffusion of water molecules. The explicit dependence of the diffusion coefficient on the microscopic physical characteristics of the system are revealed by the Stokes-Einstein relation.

$$D = \frac{RT}{6\pi r\eta N_A} = \frac{\langle \Delta r^2 \rangle}{6\tau} \quad (1.9)$$

For water molecules at 37 °C with an average separation of $r = 0.14nm$ and a viscosity of $\eta = 0.7cP = 7 \times 10^{-4} N \cdot s/m^2$ the predicted diffusion coefficient is $D = 2.3 \times 10^{-3} mm^2/s$. Using Einstein's relation between the mean quadratic displacement and the diffusion time we conclude that on average a freely diffusing water molecule is displaced by approximately $14.8\mu m$ during $50ms$.

Diffusion coefficients measured in biological tissues are slightly smaller ($\sim 1 \times 10^{-3} mm^2/s$) due to the interaction of water molecules with anatomical structures at the scale of molecular displacements $\sim 10\mu m$ (e.g. cell membranes). With nuclear magnetic resonance it is possible to quantitatively measure the apparent self-diffusion coefficient of water molecules based on the interaction between 1H water protons and an externally applied magnetic fields.

1.3 The Bloch Equations

To understand the interaction of a proton with an external magnetic field in a classical sense, we must consider both its angular momentum \mathbf{J} (due to rotating mass) and its magnetic dipole moment $\boldsymbol{\mu}$ (or spin) induced by the rotating electric surface

charge of the proton. Assuming that both charge and mass have identical spatial distributions within the proton, we can relate the two quantities $\boldsymbol{\mu} = \gamma \mathbf{J}$ through the magnetogyric ratio γ which, for the hydrogen atom ^1H , has a value of $2\pi \cdot 42.56 \times 10^6 \text{ rad/s/T}$. When placed in an external magnetic field \mathbf{B}_0 , the quantum (Gerlach and Stern, 1922) magnetic dipole moment $\boldsymbol{\mu}$ of the proton assumes one of two possible energy states $U = -\boldsymbol{\mu} \cdot \mathbf{B}_0 = \pm \frac{1}{2} \gamma \hbar B_0$, corresponding to a parallel (low energy) and anti-parallel (high energy) orientations of the magnetic dipole with respect to the direction of the field. Within a spin ensemble at thermodynamic equilibrium, the lower energy state is slightly more populated resulting in a detectable macroscopic magnetization vector \mathbf{M} oriented along the direction of the main field. For example, in $1 \text{ mL} = 1 \text{ cm}^3$ of water at 3 T , the excess spins - approximately 2.28×10^{17} , representing only 3.4 ppm (parts per million) of the total spins - induces a macroscopic magnetization of $M_0 = 9.6 \times 10^{-3} \text{ A/m}$. The application of time varying RF fields oscillating at the resonant frequency corresponding to the difference between the two energy states $f = \Delta E/h = \gamma B_0/2\pi$ can induce transitions between spin energy states of individual molecules (Rabi, 1937). This magnetic resonance effect can also be induced in ensemble of nuclei and used to study magnetic properties of liquids and solids (Bloch et al., 1946, Purcell et al., 1946).

The effect of an oscillating RF field $\mathbf{B}_1(t) = B_1(t)\hat{\mathbf{x}}$, orthogonal to the main field $\mathbf{B}_0 = B_0\hat{\mathbf{z}}$, on the macroscopic magnetization vector in the sample is described by the following equation:

$$\frac{d\mathbf{M}}{dt} = \mathbf{M} \times \gamma(\mathbf{B}_0 + \mathbf{B}_1(t)) \quad (1.10)$$

The contribution of the static field \mathbf{B}_0 is commonly removed, by analyzing the system in a frame of reference rotating with $\boldsymbol{\omega}_0 = \gamma B_0 \hat{\mathbf{z}}$. In this rotating frame of reference the RF irradiation - also referred to as excitation - results in the nutation of the magnetization vector on to a direction perpendicular to $\mathbf{B}_1(t)$. The angle by which the magnetization vector deviates from its equilibrium orientation (flip angle) is given by:

$$\theta = \int_0^t \gamma B_1(\tau) d\tau \quad (1.11)$$

Due to hardware limitations and patient safety (in clinical MRI) generally $B_1 \ll B_0$. For ^1H protons, at $3T$, the Larmor frequency is 128MHz and the wavelength is 2.3m in free space, and $\sim 11\text{cm}$ in brain tissues. The application of a 1ms square RF pulse (modulated at the resonance frequency) with an amplitude of $5.9\mu\text{T}$ will result in a 90° degree flip angle: $\mathbf{M} = -M_0 \hat{\mathbf{y}}$.

After the RF irradiation is stopped, the magnetization will eventually return back to its equilibrium alignment parallel to the main field. This process is characterized by the T_1 relaxation time constant of longitudinal recovery. A different magnetic relaxation time constant called T_2 characterizes the decay of the magnetization vector component in a plane perpendicular to the magnetic field (transverse plane). In liquids (and most biological tissue) the T_2 relaxation time constant is on the order of milliseconds, allowing sufficient time for the detection of the transverse component of the macroscopic

magnetization, oscillating at the resonance frequency, with a resonant RF coil as free induction decay (FID).

The dynamics of the macroscopic magnetization vector, including the relaxation processes, in the rotating frame of reference are summarized by the phenomenological equations called Bloch Equations:

$$\frac{d\mathbf{M}}{dt} = \gamma\mathbf{M} \times \mathbf{B}(t) - \frac{M_x\hat{x} + M_y\hat{y}}{T_2} - \frac{M_z\hat{z} - M_0}{T_1} \quad (1.12)$$

Since the duration of RF excitation is generally much shorter than the relaxation time constants of liquids and most tissues $\tau \ll T_1, T_2$, pulsed NMR is commonly used in practice and the RF excitation (Equation 1.10) and relaxation periods (Equation 1.12 with $\mathbf{B}(t) = 0$) are usually analyzed separately. The temporal succession of RF and gradient pulses is usually represented using a pulse sequence diagram (Fig. 1). The MR signal can be modulated with different sensitization (e.g. to flow, diffusion) and is generally acquired as an echo whose magnitude depends on the timing parameters of the pulse sequence such as echo time TE (interval from excitation to formation of the echo) or repetition time TR (interval between consecutive excitations of the same signal)

$$M_{xy}(TE, TR) = M_0 \left(1 - e^{-\frac{TR}{T_1}} \right) e^{-\frac{TE}{T_2}} \quad (1.13)$$

The exponential dependence in Equation 1.13 renders the MR signal highly sensitive to the T_1 and T_2 relaxation time constants. Delicately tuning the timing parameters TE and TR determines the amount of T_2 -weighting (T2W) and T_1 -weighting

(T1W) in the MR signal and results in an unparalleled ability to differentiate soft tissues. In the next section we will briefly review the molecular basis of magnetic relaxation and the methodological developments to measure T_1 and T_2 .

1.4 The magnetic relaxation time constants

The dominant mechanism for magnetic relaxation in water is the dipole-dipole coupling between the magnetic moment of a water proton ("spin") and that of a neighboring proton or surrounding material ("lattice"). This interaction depends on the distance between the dipole pair and its orientation with respect to the main magnetic field. For example, the effect of the spatially varying magnetic field around a $1H$ nucleus on the neighboring proton within the same water molecule ($0.5mT$) will fluctuate randomly in time as the water molecule rotates. The frequency spectrum $J(\omega)$ of these fluctuations is characterized by the correlation time τ_c which depends on the molecular tumbling of the host and surrounding molecules and plays a key role in determining magnetic relaxation rates.

The spin-lattice relaxation time constant T_1 characterizes the rate at which the excited nuclear-spin dipoles in the non-equilibrium system lose energy through interactions with surrounding magnetic dipoles ("lattice") that have components fluctuating at the resonance frequency ω_0 . The spin-spin relaxation time constant T_2 , on the other hand, characterizes the rate at which energy is redistributed within the spin system through interactions between excited spin dipoles and results in an overall loss

of coherence. For homogeneous liquids, such as pure water, the formalism developed by Nicolaas Bloembergen, Edward Mills Purcell and Robert Pound - the BPP model - can be used to estimate the magnetic relaxation time constants (Bloembergen et al., 1948).

Assuming that the autocorrelation function of the microscopic fluctuations causing the relaxation is proportional to e^{-t/τ_c} , where τ_c is the correlation time of the molecular tumbling motion, the relaxation time constants can be approximated as follows:

$$\frac{1}{T_1} = \frac{3\mu^2}{160\pi^2} \frac{\hbar^2\gamma^4}{r^6} \left(\frac{\tau_c}{1 + \omega_0^2\tau_c^2} + \frac{4\tau_c}{1 + 4\omega_0^2\tau_c^2} \right) \quad (1.14)$$

$$\frac{1}{T_2} = \frac{3\mu^2}{320\pi^2} \frac{\hbar^2\gamma^4}{r^6} \left(3\tau_c + \frac{5\tau_c}{1 + \omega_0^2\tau_c^2} + \frac{2\tau_c}{1 + 4\omega_0^2\tau_c^2} \right) \quad (1.15)$$

Here, $\omega_0 = \gamma B_0$ is the Larmor frequency at the applied field, μ is the magnetic dipole moment, γ is the magnetogyric ratio, and r is the average distance between two nuclei carrying magnetic dipole moment. Using a correlation time of $\tau_c = 5 \times 10^{-12} \text{s}$ for water and a average distance of $r = 0.14 \text{nm}$ between nuclei, we get a value of $T_1 \cong T_2 \cong 2.9 \text{s}$ at 3T, which compares adequately to experimental measurement.

Qualitatively, we appreciate that for pure bulk water (and other non-viscous liquids) $\omega_0\tau_c \ll 1$ and the rapid magnetic field fluctuations for each proton average out yielding large values for $T_1 \cong T_2$. In general however, $T_2 < T_1$, but this difference is especially visible in solids (e.g. ice) where $\tau_c \cong 5 \times 10^{-5} \text{s}$ and $\omega_0\tau_c \gg 1$. In viscous liquids (e.g. fat) $\tau_c \cong 5 \times 10^{-5} \text{s}$ and $\omega_0\tau_c \gg 1$ and T_1 and T_2 are generally shorter than for water. For protons associated with large molecules, such as macromolecules, the tumbling correlation time is significantly reduced and as a result T_1 and T_2 relaxation

times are on the order of hundreds of μs . With increasing temperature, the correlation time of molecular tumbling τ_c decreases and both T_1 and T_2 are expected to become larger. The dependence of the relaxation rates on the magnetic field strength is determined by the components of the frequency spectrum $J(\omega)$ at the resonant frequency $\omega_0 = \gamma B_0$. In bulk water T_1 decreases to a minimum, then increases again, while T_2 continually decreases with increasing magnetic field strength. Finally, even though in complex solutions the BPP model provides only a qualitative estimation of magnetic relaxation rates, it is often used to guide the design of new MR contrast agents. In biological samples, the presence of macromolecules with diverse hydration dynamics often leads to non-monoexponential magnetic relaxation. Nevertheless, tissue averages of T_1 and T_2 values vary sufficiently in vivo to result in excellent soft tissue contrast that is indispensable for many clinical applications.

The quantitative measurement of T_2 relaxation rates and diffusion effects in NMR began in 1950, when E.L. Hahn observed the formation of a second free induction decay at time TE following the application of two consecutive 90° RF pulses at times $t = 0$ and $t = TE/2$ (Hahn, 1950). He noted that the application of the second RF pulse inverts the phase accumulated by a spin system under the effect of inherent background field inhomogeneity gradients in the sample and restores the coherence of static spins to result in the formation of a refocused echo (called spin echo) at time TE . Hahn also discussed the residual magnitude signal loss (loss of coherence) due to the diffusive

motion of spins in the presence of inherent field inhomogeneities, thus inaugurating the impending development of diffusion NMR. While T_2 and diffusion have similar effects of reducing the signal coherence, they differ in that one characterizes local mobility (tumbling) while the latter characterizes spatial mobility (translation).

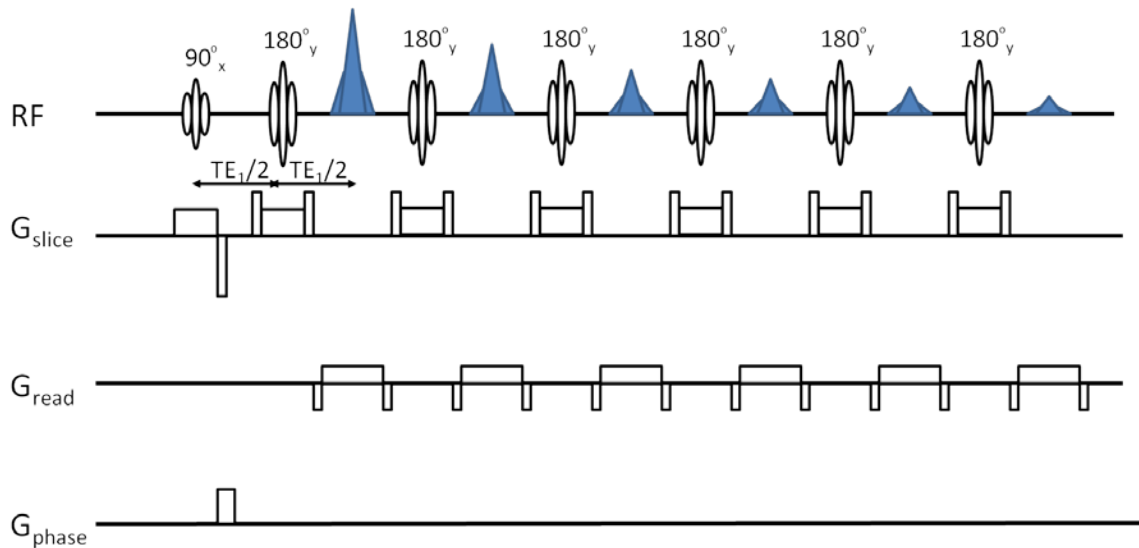


Figure 1: Carr-Purcell-Meiboom-Gill (CPMG) pulse sequence for measuring T_2 's of substances. A train of 180 pulses is applied to repetitively refocus the signal and reduce diffusion effects due to inherent magnetic field inhomogeneities.

A few years after Hahn's seminal paper, H.Y. Carr and E.M. Purcell modified the Hahn spin echo method to reduce phase accumulation from diffusional random walk by repetitive refocusing of spin trajectories using a train of 180 pulses (Carr and Purcell, 1954). Later, Saul Meiboom and David Gill (Meiboom and Gill, 1958) adapted the technique to increase its stability in the presence field inhomogeneities and imperfect 180 RF pulses. Since then, the Carr-Purcell-Meiboom-Gill (CPMG) sequence has been employed extensively to measure T_2 relaxation times in a variety of biological samples

(Vasilescu et al., 1978). With the development of techniques for spatial encoding, this unique soft tissue contrast proved invaluable to clinical imaging and established MRI as a pivotal diagnostic imaging modality.

1.5 Spatial encoding in MRI

In 1973, Paul Lauterbur proposed a revolutionary technique to encode spatial information in the NMR signal using superimposed linear magnetic field gradients to modify the resonant frequency of spins in a spatially dependent manner (Lauterbur, 1973). Signals from different spatial locations can be easily resolved using a Fourier frequency decomposition of the FID. In general, image acquisition in MRI is achieved with the use of magnetic field gradients to sample the Fourier-spatial frequency domain (k-space) components (Ljunggren, 1983, Twieg, 1983) of that object:

$$\mathbf{k}(t) = \frac{\gamma}{2\pi} \int_0^t \mathbf{G}(\tau) d\tau \quad (1.16)$$

For example, in echo planar imaging the entire k-space of a 2D imaging slice is covered in a rectilinear fashion within a single FID readout (Mansfield, 1977). This highly efficient gradient encoding scheme was originally proposed by Sir Peter Mansfield who, along with Lauterbur was awarded the 2003 Noble Prize in Physiology and Medicine for their developments of clinical MRI.

In today's state-of-the-art MR scanners spatial encoding is achieved using independent circuit coils generating magnetic field gradients along all three spatial

dimensions with amplitudes as large as $80mT/m$ and slew rates of $200T/m/s$. Recent advances in parallel imaging (Sodickson and Manning, 1997, Pruessmann et al., 1999) leverage additional encoding capabilities from spatially varying sensitivity profiles of multiple coils within phased arrays (Roemer et al., 1990), while innovative custom designed sampling strategies cover k-space more efficiently, significantly increasing imaging throughput and/or reducing distortions (Ahn et al., 1986, Frahm et al., 1986, Song et al., 1994) for a variety of different applications.

Today MRI plays a unique role in diagnostics, pre-surgical planning and treatment monitoring. Within seconds, high resolution images can be acquired non-invasively. The low radio-frequency MR signal can be detected even from structures deep within the body (e.g. white matter in the brain) with excellent signal-to-noise (SNR) and contrast-to-noise (CNR) ratio. Additionally, MR pulse sequences can be made sensitive to a variety of contrast mechanisms that reflect diverse cellular properties (magnetic relaxation, proton density, magnetic susceptibility, metabolite concentration, macromolecular concentration etc.) and biophysical processes (blood flow, diffusion, perfusion, changes in oxygenation, protein hydration, molecular exchange, etc). Over the last two decades these quantitative structural and functional measurements have changed our understanding of the physiology and pathology of the human body.

1.6 The NMR diffusion experiment

Diffusion weighted contrast quantitatively characterizes the incoherent scattering of self-diffusing water molecules interacting with the stationary tissue micro-anatomy.

Mathematically, it can be understood as a loss of coherence due to diffusing spins accumulating random phase $\Delta\phi$ in the presence of a magnetic field gradient $\mathbf{G}(\tau)$:

$$\Delta\phi = \gamma \int_0^t \mathbf{G}(\tau) \cdot \mathbf{r}(\tau) d\tau \quad (1.17)$$

For a sufficiently large number of spins undergoing Brownian motion $\mathbf{r}(\tau)$, the probability distribution of phase shifts becomes Gaussian $p(\Delta\phi)$ with mean 0 and variance $\langle\Delta\phi^2\rangle$ and results in a magnitude decay of the complex ensemble averaged transverse magnetization which can be related to the diffusion coefficient D (Equation 1.18). For example, in the presence of a constant gradient of magnitude \mathbf{G} a spin echo experiment with duration t results in a magnitude attenuation factor of:

$$\langle e^{-i\Delta\phi} \rangle = \int_{-\infty}^{\infty} e^{-i\Delta\phi} \frac{1}{\sqrt{2\pi\langle\Delta\phi^2\rangle}} e^{-\frac{\Delta\phi^2}{2\langle\Delta\phi^2\rangle}} d\Delta\phi = e^{-\frac{\gamma^2 G^2 t^3 D}{3}} = e^{-bD} \quad (1.18)$$

where we have introduced the parameter b (called b-value) which determines the effective diffusion sensitization based on the duration and magnitude of the magnetic field gradient.

To understand NMR diffusion effects in general, Henry C. Torrey extended the Bloch equation by adding a diffusion term (Torrey, 1956).

$$\frac{d\mathbf{M}(\mathbf{r}, t)}{dt} = \gamma \mathbf{M}(\mathbf{r}, t) \times \mathbf{B}(\mathbf{r}, t) - \frac{M_x \hat{\mathbf{x}} + M_y \hat{\mathbf{y}}}{T_2} - \frac{M_z \hat{\mathbf{z}} - M_0}{T_1} + \nabla \cdot (D \nabla \mathbf{M}) \quad (1.19)$$

In general, the Bloch-Torrey equation can be solved (Haacke, 1999) for any time-dependent gradient satisfying $\int_0^{TE} \mathbf{G}(t)dt = 0$ (condition required for echo formation at time TE) and results in a signal magnitude S attenuation factor of e^{-Db} , where:

$$S = M_0 \left(1 - e^{-\frac{TR}{T_1}} \right) e^{-\frac{TE}{T_2}} e^{-Db} \quad (1.20)$$

$$b = \gamma^2 \int_0^t \left(\int_0^\tau \mathbf{G}(\tau')d\tau' \right)^T \cdot \left(\int_0^\tau \mathbf{G}(\tau')d\tau' \right) d\tau \quad (1.21)$$

and D is the diffusion coefficient.

The theory and methodology for quantitatively measuring diffusion coefficients with NMR was pioneered in 1965 by Edward O. Stejskal and John E. Tanner (Fig. 2) who proposed the use of externally applied time-dependent magnetic field gradients to improve the diffusion encoding capabilities in spin echo experiments (Stejskal and Tanner, 1965). In the case of pulsed gradients spin echo (PGSE) experiment the b-value is given by:

$$b = \gamma^2 G^2 \delta^2 \left(\Delta - \frac{\delta}{3} \right) \quad (1.22)$$

where δ is the duration of the diffusion encoding gradient pulses of magnitude G and Δ is the separation between them (Fig. 2).

Today, routine clinical spin echo DWI scans use b-values between 600 – 1500s/mm². The maximum diffusion sensitization (b-value) is generally limited by the amplitude and duration of the diffusion encoding magnetic field gradient pulses. The

amplitude of the gradients G is restricted by hardware capabilities, such as gradient heating or duty cycle, and patient safety hazards such as peripheral nerve stimulation (Cohen et al., 1990) while the maximum duration of the applied gradients δ is generally limited by the signal amplitude exponentially decaying with time constant T_2 during transverse duration TE . It is therefore not possible to achieve large diffusion sensitization with short echo times. For many advanced diffusion models however, large b -values are desirable as they allow a more comprehensive characterization of the displacement probability distribution of water molecules in complex tissue micro-geometry revealing signs of restricted or hindered diffusion (Cohen and Assaf, 2002). Large b -values required for these measurements are generally achieved using a stimulated echo mechanism.

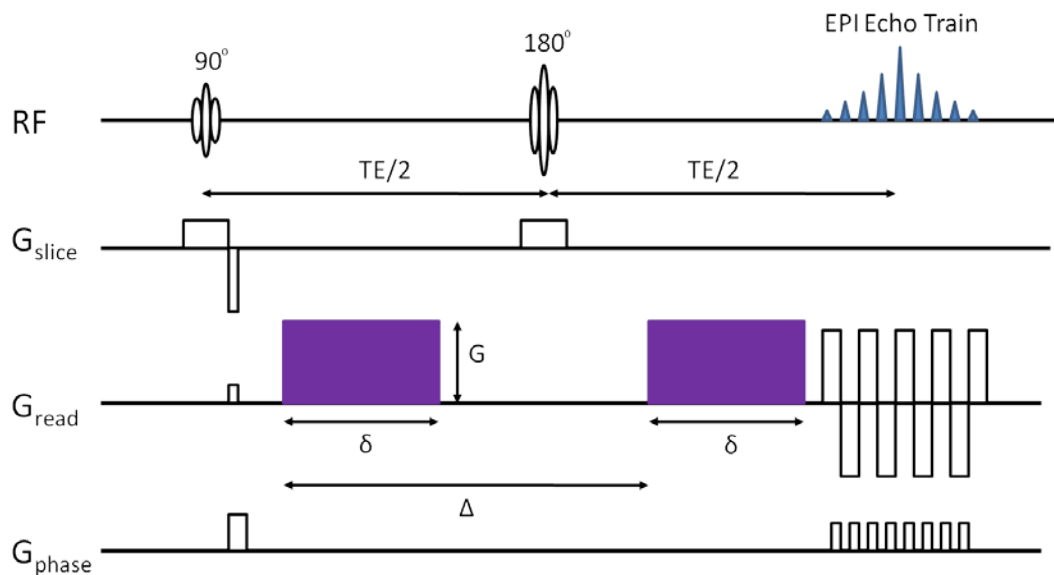


Figure 2: Pulse sequence diagram showing a Stejskal-Tanner diffusion weighted pulse gradient spin echo (PGSE) pulse sequence with echo-planar imaging EPI readout, which uses two identical gradient

pulses on either side of a refocusing pulse. The diffusion sensitization (Equation 1.22) is a function of the duration δ and amplitude G of the gradient pulses, as well as their separation Δ .

A stimulated echo can be formed by replacing the refocusing effect of the 180° degree RF pulse with two 90° pulses separated by an arbitrary distance TM (Fig 3). At $TE/2$ after excitation a 90° degree pulse aligns the transverse magnetization along the longitudinal plane. During the longitudinal (mixing) period TM , the accumulated phase is stored and the signal magnitude decays with the T_1 relaxation time constant. The last 90° degree pulse re-aligns the magnetization in the transverse plane and refocuses the signal to form a stimulated echo after another $TE/2$ time interval (Frahm et al., 1985). The signal amplitude of the stimulated echo forming at $TM+TE$ after excitation is half of that measured using a spin echo with the same TE . Nevertheless, phase memory across the large separation between periods of transverse evolution (TM intervals) recommends this sequence for large b -value diffusion applications (Merboldt et al., 1985). In a pulsed gradient stimulated echo (PGSTE) diffusion preparation, gradients with significantly shorter duration δ can be used at full-amplitude G with much larger separation Δ resulting in significantly shorter echo times and/or larger b -values (Fig 3).

anisotropy is inferred from the water self-diffusivity rank-2 tensor estimated from images acquired with diffusion sensitizing gradients oriented along at least 6 non-collinear orientations (Basser and Pierpaoli, 1998).

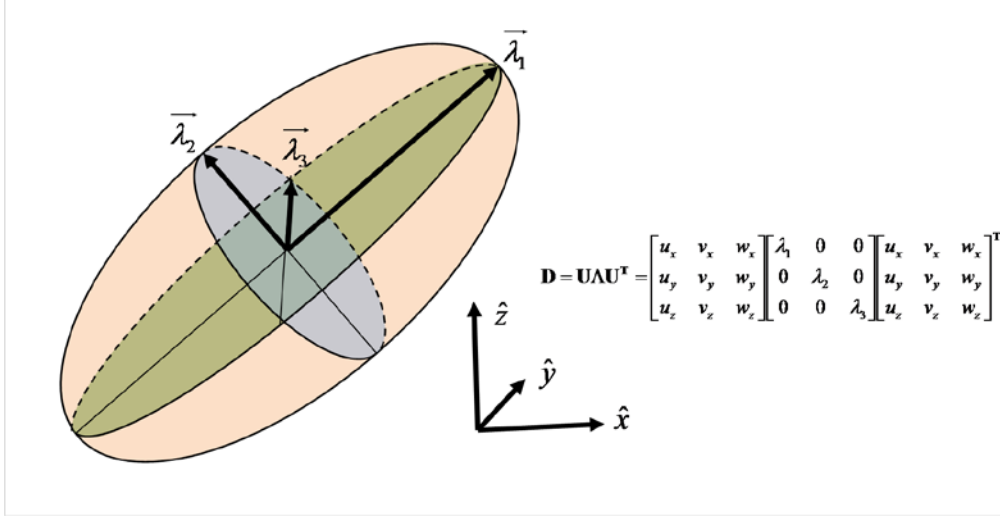


Figure 4: Eigenvalue decomposition of diffusion tensor. For every voxel, the diffusion tensor can be decomposed along three orthotropic axes related to the underlying tissue orientation.

In general, for a Stejskal-Tanner PGSE diffusion encoding scheme with diffusion gradient pulses of amplitude G and duration δ applied along \mathbf{g}_i separated by Δ , measured transverse DW signal is:

$$S_i = S_0 e^{-\mathbf{b}:\mathbf{D}} = M_0 \left(1 - e^{-\frac{TR}{T_1}} \right) e^{-\frac{TE}{T_2}} e^{-\mathbf{b}:\mathbf{D}} \quad (1.23)$$

where S_0 is the baseline transverse magnetization acquired without diffusion encoding.

The signal attenuation can be written:

$$\mathbf{b}:\mathbf{D} = -\ln\left(\frac{S_i}{S_0}\right) = \gamma^2 G^2 \delta^2 \left(\Delta - \frac{\delta}{3} \right) \mathbf{g}_i^T \mathbf{D} \mathbf{g}_i \quad (1.24)$$

Two key properties of the diffusion tensor (diagonal symmetry and positive-definitiveness) are revealed by extending the Einstein diffusion equation (Equation 1.1) to a second-order tensor

$$\mathbf{D} = \begin{pmatrix} D_{xx} & D_{xy} & D_{xz} \\ D_{yx} & D_{yy} & D_{yz} \\ D_{zx} & D_{zy} & D_{zz} \end{pmatrix} = \frac{1}{2\tau} \langle \Delta \mathbf{r}^T \Delta \mathbf{r} \rangle = \frac{1}{2\tau} \begin{pmatrix} \langle \Delta x^2 \rangle & \langle \Delta x \Delta y \rangle & \langle \Delta x \Delta z \rangle \\ \langle \Delta y \Delta x \rangle & \langle \Delta y^2 \rangle & \langle \Delta y \Delta z \rangle \\ \langle \Delta z \Delta x \rangle & \langle \Delta z \Delta y \rangle & \langle \Delta z^2 \rangle \end{pmatrix} \quad (1.25)$$

where $\Delta \mathbf{r} = \mathbf{r} - \mathbf{r}_0$ is the displacement (row) vector of as a function of diffusion time and τ . The diffusion tensor is symmetric $D_{ij} = D_{ji}$ and has assumes an eigenvalue decomposition along three orthotropic axes with positive diffusivities along these axes (Fig. 4). To estimate the 6 independent components of the diffusion tensor we can acquire several images with different diffusion weighting orientation \mathbf{g}_i with $i = \overline{1, N}$ and reformulate Equation 1.24 as a linear system with:

$$\begin{aligned} \mathbf{S} &= \left[-\ln\left(\frac{S_1}{S_0}\right) \quad -\ln\left(\frac{S_2}{S_0}\right) \quad \dots \quad -\ln\left(\frac{S_N}{S_0}\right) \right]^T \\ \mathbf{x} &= [D_{xx} \quad D_{xy} \quad D_{xz} \quad D_{yy} \quad D_{yz} \quad D_{zz}]^T \\ \mathbf{B} &= \gamma^2 G^2 \delta^2 \left(\Delta - \frac{\delta}{3} \right) \begin{bmatrix} g_{1,x}g_{1,x} & g_{1,x}g_{1,y} & \dots & g_{1,z}g_{1,z} \\ g_{2,x}g_{2,x} & g_{2,x}g_{2,y} & \dots & g_{2,z}g_{2,z} \\ \dots & \dots & \dots & \dots \\ g_{N,x}g_{N,x} & g_{N,x}g_{N,y} & \dots & g_{N,z}g_{N,z} \end{bmatrix} \\ \mathbf{S} = \mathbf{B}\mathbf{x} &\rightarrow \mathbf{x} = (\mathbf{B}^H \mathbf{B})^{-1} \mathbf{B}^H \mathbf{S} \end{aligned} \quad (1.26)$$

The underlying tissue anisotropy can be visualized with ellipsoid representations of the computed diffusion tensors (Fig. 4) and quantitatively characterized with scalar invariants such as eigenvalues (which represent the diffusivities along the orthotropic axes of the tissue orientation) or anisotropy measures such as fractional anisotropy (FA),

relative anisotropy (RA) or volume ratio (VR). The most common measure is fractional anisotropy which can be defined with respect to the three eigenvalues $\lambda_1, \lambda_2, \lambda_3$:

$$FA = \sqrt{\frac{1}{2} \sqrt{\frac{(\lambda_1 - \lambda_2)^2 + (\lambda_2 - \lambda_3)^2 + (\lambda_3 - \lambda_1)^2}{\lambda_1^2 + \lambda_2^2 + \lambda_3^2}}} \quad (1.27)$$

In white matter for example the orientation of the ellipsoids follows the direction of the white matter fiber bundles composed of tightly packed, highly ordered arrangements of axons (several μm in diameter) that enable electrical communication between isolated brain regions. Because of the cylindrical symmetry of axons the local diffusion tensor usually estimates one major axis (eigenvector) of diffusion parallel to the axon orientation (axial diffusivity $\lambda_{||}$) and two minor axes orthogonal to the primary eigenvector (whose average represents the radial diffusivity λ_{\perp}). Both axial and radial diffusivities can be used to characterize changes in white matter integrity. The most common measure of anisotropy however, is fractional anisotropy (FA) which quantifies the normalized variance of the three eigenvalues of the DTI tensor. With recent developments in gradient hardware, researchers have designed faster and more efficient imaging schemes and developed advanced diffusion models capable to separate multiple fibers within a voxel (Frank, 2002), infer restriction/hindrance parameters (Assaf and Basser, 2005), or characterizing deviations from pure Gaussian diffusion (Liu et al., 2010).

Over the past decade, DTI has proven instrumental not only for connectivity mapping and fiber tracking (Mori and Zhang, 2006) in healthy brains, but also for revealing changes in white matter anisotropy that may correlate with healthy brain development (Moseley, 2002) and neurological disorders (Assaf and Pasternak, 2008). However, the complexity of brain structure within a typical MRI voxel makes it difficult to dissociate the tissue origins of the measured anisotropy. The tensor characterization is a composite result of proton pools in different tissue and cell structures (e.g. membranes, microtubules, neurofilaments, myelin sheaths, axonal water, and vasculature) with diverse diffusion properties. As a result, in many neurological and neuropsychiatric disorders with white matter pathology, changes in anisotropy often cannot be specifically correlated with changes in the underlying neuronal-specific structures (Beaulieu, 2002).

1.7.1 The emergence of DTI for studying white matter changes

Since DTI measures both the directionality and the rate of displacement of water molecules across tissue components (Basser et al., 1994a, Basser and Jones, 2002), it can identify transformations (e.g. during brain development, in white matter brain diseases, etc.) in the white matter microanatomy that may not be detectable as a volumetric/scalar change. In recent years, researchers have been actively applying DTI to investigate white matter microstructure changes during normal brain development or in disease. The DTI findings complement those of the conventional contrasts (e.g. T₁-weighted, T₂-weighted

etc.) and consistently indicate that white matter anisotropy (measured using fractional anisotropy) may be correlated to neuronal functions. However, the lack of tissue specificity in DTI significantly limits the diagnostic value of these correlations which cannot provide direct links to specific neuronal origins.

Although still at a preliminary stage, the potential clinical utility of DTI is being explored in a number of neuro-developmental conditions, including congenital brain malformations, metabolic disorders, and common neuro-developmental disorders. The unique contrast in DTI may lead to future clinical applications in diagnosis and disease monitoring, including responses to therapeutic interventions (Mukherjee and McKinstry, 2006).

One of the most exciting applications of DTI may be the possibility of investigating white matter maturation in pediatric brains, especially during the first two years which constitute the most dynamic phase of post-natal brain development. During this period, the brain reaches 80-90% of its adult volume (Pfefferbaum et al., 1994), the overall pattern of adult myelination is nearly completed (Nelson and Collins, 2008) and there is a robust elaboration of new synapses (Huttenlocher and Dabholkar, 1997). Concurrently an equally rapid development of a wide range of cognitive, social, and language abilities occurs (Kagan and Herschkowitz, 2005). It has been proposed that myelination occurs in concert with the maturation of central nervous system (CNS) functions. Both processes evolve in documented similar patterns of maturation starting

with the primary functions (e.g. visual, sensory, motor, etc.) and concluding with the complex integrative functions in the frontal brain regions (Yankelov and Lecours, 1967, Nelson and Collins, 2008).

Although there is some question as to how diffusion properties in white matter behave across the life span (Salat et al., 2005), the literature is remarkably consistent in affirming an increase in anisotropy and decrease in overall diffusion with age during childhood and adolescence (Sakuma et al., 1991, Nomura et al., 1994, Huppi et al., 1998, Pfefferbaum et al., 2000, Mukherjee et al., 2001, Abe et al., 2002, Engelbrecht et al., 2002, Mukherjee et al., 2002, Schmithorst et al., 2002, Counsell et al., 2003). This development is likely the result of both ongoing myelination and axonal pruning - changes which increase the efficiency of neuronal communication and provide a substrate for healthy cognitive and behavioral development (Suzuki et al., 2003).

Based on the empirical associations between the diffusion anisotropy and white matter development, DTI may offer a unique noninvasive approach to characterize WM development during the first few years of life. In particular, robust developmental effects are observable in fractional anisotropy (FA) values from premature infants through early childhood that are thought to reflect coherence and organization (i.e., myelination and axonal membranes) of white matter (Beaulieu, 2002). While these reliable age-related changes in FA support the potential utility of DTI for the investigation of the structural changes during brain development, and for studying

brain diseases of white matter origin in children (Glenn et al., 2003, Peng et al., 2004), the current methodology does not yet allow specific and separate assessment of myelin from axons.

In addition to the relationship between white matter anisotropy and development, researchers have also found a strong correlation between white matter anisotropy and cognitive performance, both in children and in adults. Specifically, the development of particular cognitive functions (e.g. working memory capacity or reading ability) is positively correlated with increased fractional anisotropy in restricted regions of the brain (e.g. left frontal lobe, or temporal lobe respectively). However, despite numerous reports corroborating these results, the changes in anisotropy have yet to be conclusively related to a specific origin. In other words, it is still unclear whether the underlying mechanism for the observed anisotropy decrease is a loss of myelin or a decrease of axonal density, or coherence. Thus, in order to better understand the causality between connectivity changes and cognitive functions during brain development, it is crucial to develop a more specific DTI acquisition method that can better differentiate causes of diffusional change.

1.7.2 Advanced DTI methods

Recently, several diffusion imaging strategies have been proposed that could allow better inference on tissue specificity and voxel composition (Tuch et al., 2005, Wedeen et al., 2008), for example, by resolving crossing fibers.

To illustrate, the recent development of advanced diffusion weighted imaging methods such as high angular resolution diffusion imaging (HARDI) (Frank, 2001), diffusion spectrum imaging (DSI) (Wedeen et al., 2005), generalized diffusion tensors (GDTI) (Ozarslan and Mareci, 2003, Liu et al., 2004a) or Q-ball imaging (Tuch, 2004) which acquire images with a large number of diffusion orientations and diffusion weighting factors, can provide a better characterization of the displacement probability distribution function (Callaghan, 1991, Callaghan et al., 1991). Such large b-value measurements can be further used with multi-tensor models for resolving crossing fibers, or models of restricted and hindered diffusion (Assaf and Basser, 2005, Assaf et al., 2008) to explain non-Gaussian diffusion effects in vivo. While these methods might potentially yield more sensitive biomarkers for neurodegenerative white matter diseases, they provide only an indirect measure of tissue specificity, have limited sensitivity and require long scan times.

Alternatively, the voxel composition can be further characterized by increasing the resolution of the DTI scan (Liu et al., 2004b). Even though high resolution DTI techniques significantly improve full-brain structural connectivity studies by resolving smaller fibers at the gray/white matter interface, they come at a clinically prohibitive cost in signal-to-noise ratio (SNR) efficiency and provide limited additional insight into the glial (myelin) or axonal origin of white matter pathologies compared to conventional DTI scans.

1.7.3 Limitations of DTI and the need for increased tissue specificity

Acknowledging the current lack of tissue or neuronal (tissue/cellular) specificity in DTI assessment of brain development and cognitive functions, researchers have implemented various techniques aimed at addressing the existing shortcomings. For example, the current implementation of DTI often suffers from fluid and flow contaminations from CSF and vasculature due to significant partial volume effect at relatively low spatial resolution, especially in the ventral brain regions, within the periventricular space or close to the cortical surface. Early methods for removing the confound have relied on an inversion recovery technique (Bhagat and Beaulieu, 2004, Ma et al., 2004) which could result in a large reduction in signal-to-noise ratio and temporal resolution. As such, improved methodology that mitigates these weaknesses will be necessary, which are discussed in our research plan.

Certainly, removing confounding signal alone does not guarantee tissue or neuronal specificity. Indeed, given the multiple contributing signal sources within the white matter, innovative ways of selecting specific proton pools will be required. A recent attempt to achieve tissue specificity was through the use of diffusion tensor spectroscopy (Basser et al., 1994b, Ellegood et al., 2006, Upadhyay et al., 2007). It was shown that it is possible to estimate the diffusion anisotropy of N-acetyl aspartate (NAA), a neuronal specific metabolite that exists only in the intracellular space and is an index for neuronal viability. While this technique clearly offers specificity to intracellular

proton pools, it is limited by the nature of spectroscopic acquisition – in that only limited spatial coverage can be achieved within each acquisition and the SNR is poor due to the low concentration of NAA.

The effort to achieve tissue specificity in DTI is still ongoing - it is hoped that a sensitive yet specific technique can be developed to allow researchers to have more exclusive assessment on a particular tissue or water pool of interest (e.g. myelin water).

Chapter 2: Importance of Imaging Myelin Microstructure and Strategies for Myelin Specific DTI

This chapter considers the possibility of integrating DTI with MR techniques for myelin contrast imaging in order to achieve sensitization to myelin microanatomy. First, myelin morphology and physiology are briefly presented followed by a discussion of myelin microstructural changes associated with white matter pathologies and healthy brain maturation. Finally we review different strategies for myelin contrast MR imaging and highlight the need and feasibility of constructing a diffusion tensor capable to detect changes in myelin microstructure.

2.1 The role of myelin in neuronal signaling

The human nervous system constantly monitors, integrates and coordinates information about the external and internal environments. Sensory information is gathered through specialized receptors and transmitted via the peripheral nervous system to the brain (Gall and Spurzheim, 1810). The human brain is organized according to highly energy efficient, space-saving scaling rules (Herculano-Houzel, 2009) into a complex modular architecture (Broca, 1861) that supports optimal communication between 100 billion neuronal cells (neurons) through specialized mechanisms of point-to-point chemical signaling (synapses) and long-range electrical signaling (myelinated axons). Apart from neurons, the human brain contains an equal or greater number of glial cells - such as astrocytes or oligodendrocytes - (Azevedo et al., 2009) which provide

metabolic support, form myelin, maintain homeostasis, and participate in signaling and brain development (Allen and Barres, 2009). Morphologically, the human brain can be analyzed in two regions with separate microstructural features and underlying signaling mechanisms: gray matter containing randomly oriented neuronal cell bodies and dendrites, and white matter comprising highly ordered geometrical arrangements of parallel cylindrical myelinated axons.

Gray matter (GM) contains the convoluted surface of the brain where billions of neurons interact electrochemically through modulatory signals (e.g. excitatory, inhibitory etc.) via ~1 quadrillion synapses (Murre and Sturdy, 1995). These numerous connections between neurons result in adaptive intricate neural circuits capable to carry out complicated functions (McCulloch and Pitts, 1990, Dayan and Abbott, 2005) that form our perception of the world, structure our memories, and determine our behavior.

Meanwhile, white matter (WM) represents the anatomical infrastructure mediating communication between segregated brain regions through electrical impulse propagation with a speed of up to 80 m/s (Kandel et al., 2000). Human white matter contains parallel arrangements of tracts, organized in fascicles comprising tightly packed bundles of cylindrical nerve fibers. A single nerve fiber consists of an axon (a protoplasmic protrusion of the neuron) and the medullar myelin sheaths (formed by the oligodendrocyte cellular membrane).

The axon in human white matter has a cylindrical shape with an average radius of $1 - 1.5\mu m$ and several feet in length. It contains a variety of organelles with diverse microstructures: mitochondria, smooth endoplasmatic reticulum, synaptic vesicles and a densely packed cytoskeleton. The highly ordered cytoskeleton includes parallel arrangements of microtubules ($\sim 25nm$ in diameter) and microfilaments ($\sim 4nm$ in diameter) serving as scaffold for trafficking macromolecules (Kandel et al., 2000) and neurofilaments ($\sim 10nm$ diameter) providing structural support for the axon.

2.1.1 Myelin microstructure

Myelin is formed as a specialized extension of the oligodendrocyte proteo-lipid bi-layer plasma membrane (Virchow, 1854) which repeatedly envelops a particular stretch of the axon $\sim 0.2 - 1mm$ long (Fig. 5). Its function is to metabolically support and electrically insulate the axon facilitating a more energy efficient, space-saving and rapid conduction of the action potential. The structure and function of myelin is supported by its chemical composition.

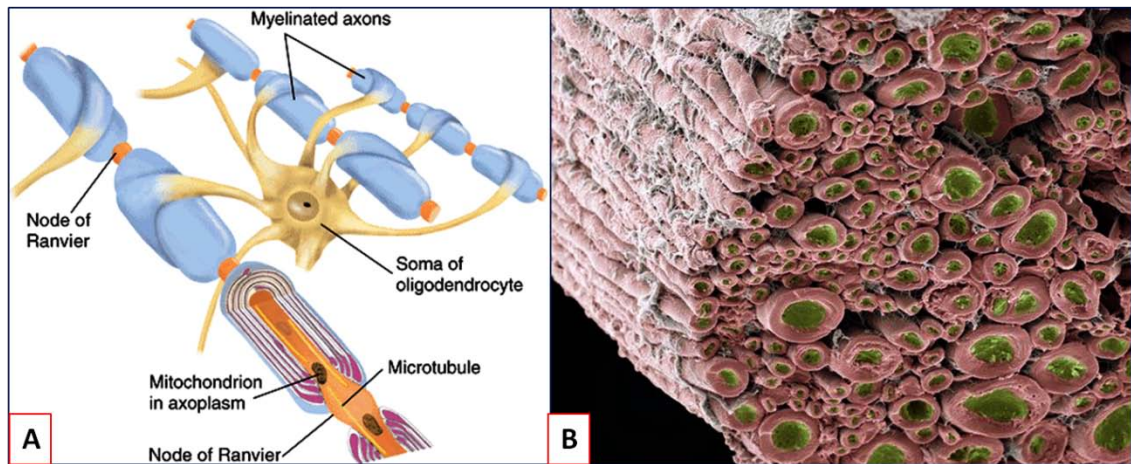


Figure 5: Microanatomy of white matter. A. Myelin is formed as an extension of the oligodendrocyte bi-lipid plasma membrane membrane tightly wrapping around the axons (credit Steven Gschmeissner / Science Photo Lab). **B.** The complex white matter microstructure makes it difficult to disentangle diffusional changes of myelin (pink) or axonal (yellow) origins using conventional diffusion tensor techniques.

Myelin accounts for approximately 40 – 50% of the central nervous system (CNS) white matter; interestingly, it contains only ~40% water by weight, while its dry mass is composed of abundant macromolecules such as proteins (15 – 30%) and lipids (70 – 85%) (Baumann and Pham-Dinh, 2001). Chemical studies indicate that the most abundant myelin proteins are the myelin basic protein (MBP) ~30%, proteo-lipid protein (PLP) ~50%, 2'3'-Cyclic nucleotide 3'-phosphohydrolase (CNP) ~4%, myelin associated glycoprotein (MAG) ~1% and myelin oligodendrocyte glycoprotein (MOG) < 1%. Lipids commonly found in myelin are cholesterol (extracellular), phospholipids (intracellular) and glycolipids (extracellular) in molar ratios of 4: 3: 2 (Morell and Quarles, 1999). This abundance of macromolecules and lipids, relative to other white matter components, gives rise to unique magnetic interactions that can be exploited as

sensitive selection criteria for myelin water (water trapped between the myelin layers) in MRI (e.g. short T_2 , magnetization transfer, magnetic susceptibility contrast). The electrostatic interactions between these lipids and macromolecules give rise to the compact multi-lamellar micro-architecture spiraling around the circumference of the axon.

Electron microscopy studies of myelin ultra-structure reveal a periodic arrangement (periodicity of $\sim 12nm$) of dense intra- and extracellular compartments alternating between the lipid membrane layers (Hildebrand et al., 1993) (Fig. 6). The thickness of the intracellular (high electron density) layer is modulated by the non-covalent forces between MBP and the membrane phospholipids on the opposite side (Min et al., 2009). Meanwhile, the extracellular (lower electron density) layer contains PLP and other proteins that coordinate the adherence of opposing extracellular faces (Klugmann et al., 1997). These proteo-lipid interactions determine the membrane packing within the $\sim 0.7\mu m$ thick myelin sheath and play a critical role in maintaining the microstructural integrity of myelin and implicitly its electrophysiological function.

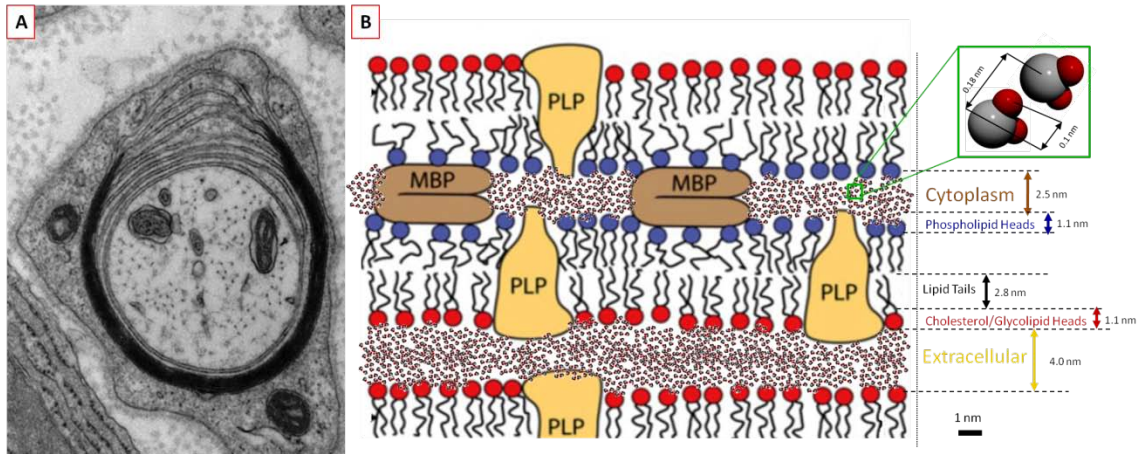


Figure 6: A. Electron microscopy image of myelin microstructural changes adapted from (Novak et al., 2011). B. The spacing between adjacent layers of myelin is determined by the electrostatic interaction between myelin proteins and lipids adapted from (Min et al., 2009). Conventional myelin contrast MR imaging can investigate changes in myelin content, but are not sensitive to the gradual loosening of myelin layers (A) associated with early stages of demyelination pathologies.

2.1.2 The function of myelin in nerve electrophysiology

The importance of myelin in nerve conduction can be understood by comparing the unmyelinated giant squid axon (diameter $\approx 500 \mu m$) to the myelinated frog sciatic nerve (diameter $\approx 12 \mu m$). While both support conduction velocities of up to $25 m/s$, the former requires 5000 times more energy and occupies 1500 times more space. This enormous functional advantage is derived from the multi-lamellar myelin micro-geometry which generates a significant increase in the effective resistance and decrease in the effective capacitance across the polarized axonal membrane. Consequently, the propagation of electric impulses along the myelinated axon occurs in a saltatory fashion with the axonal membrane depolarizing only at discrete locations, called nodes of Ranvier (Ranvier, 1878), where Na^+ ion channels aggregate (Ritchie and Rogart, 1977). Theoretical models for action potential propagation along the axon (Hodgkin and

Huxley, 1952, Frankenhaeuser and Huxley, 1964) demonstrate the strong relation between myelin microstructure and its electrophysiological function.

Optimal propagation of the action potential requires fine-tuning of myelin microstructural parameters, depending on the axonal radius. Experiments and simulations indicate that parameters such as the interlamellar period (Min et al., 2009) the thickness of the myelin layer (Hildebrand and Hahn, 1978) or the inter-nodal distance (Friede, 1986), determine electrical properties of myelin sheath (Frankenhaeuser and Huxley, 1964, Min et al., 2009) and control the speed, reliability and energetic cost of the action potential propagation.

2.2 Changes in myelin microstructure during neurological disorders of white matter origin and normal brain development

The speed, energy efficiency and reliability of neural transmission plays an important role in neuronal communication and therefore cognitive performance. It is now generally understood that myelin insulation around the axons greatly improves the neuronal conductivity. Abnormal myelin can result from damaged myelin sheath (demyelination) in white matter lesions (e.g. multiple sclerosis, Alzheimer's disease) or from defective myelin formation (dysmyelination - e.g. schizophrenia) (Filley, 2001). Demyelination pathologies are usually accompanied by the disruption and unraveling of myelin sheath segments resulting in large amounts of myelin debris, followed by macrophage response with varying timelines (Vargas and Barres, 2007). In the case of

dysmyelination, the myelin sheaths can become structurally loose forming irregular (bulging) wrappings. Generally changes in myelin microstructure corrupt nerve function and lead to diverse symptoms ranging from tremors, seizures, impaired sensation, movement, cognitive functions and potentially dementia. While animal studies have investigated myelin changes in various mouse models of neurological disorders (Nave, 1994), translating their findings to human populations is not straightforward. The specific physiopathological mechanisms and clinical evolution of neurological brain disorder remain unclear (Barkovich, 2000, Laule et al., 2007).

Correct formation of multi-lamellar myelin microstructure is essential in the electrophysiology of nerve fibers and plays an important role in healthy brain development. Structural maturation of individual brain regions and their connecting pathways during the first decade of life, is required for the successful development of key brain functions (e.g. sensorimotor, cognitive, etc.). This maturation eventually provides a smooth flow of neural impulses throughout the brain, which allows for information to be effectively integrated across many spatially segregated brain regions involved in these functions. Axons of the major pathways in the human brain, such as those connecting the frontal lobe (responsible for higher cognitive functions) to the other brain regions, the corpus callosum (which connects the two halves of the brain) or the corticospinal tract (which connects the brain to the spinal cord and the rest of the body), continue to develop throughout childhood. Postmortem studies suggest that the

myelination process in these major fiber tracts undergo continuous growth in the first decade of brain development. However, the scarcity of human brain specimens for postmortem analysis has made it difficult to draw definite conclusions about the timetable of myelination during childhood and adolescence.

Because of the critical importance of the myelin sheath in improving the conductivity axons, myelination is a major aspect of the machinery of neural circuits and cognitive functions. Generally, abnormal myelin formation is a hallmark of neurodegenerative pathologies which can significantly reduce the quality of life for many patients. The economic, social and medical cost of neurological disorders of white matter origin justifies the development of advanced neuroimaging methods for assessing myelin morphological changes during brain disorders and healthy brain development.

2.3 Myelin Imaging

Because of its importance in the investigation of brain development and neuropsychiatric disorders of white matter origin, myelin imaging has attracted increasing attention in the neuroimaging research community.

In white matter samples, the microstructure of myelin can be directly imaged using various modalities. For example neutron or x-ray diffraction (Padrón et al., 1979) and electron microscopy methods can resolve the ultrafine layered myelin microstructure with *nm* resolution (e.g. lamellar periodicity) while confocal microscopy

(Reynolds et al., 1994), near-infrared imaging, fluorescence microscopy (Wang et al., 2010), Raman Spectroscopy (Pezolet and Georgescauld, 1985) or Coherent Anti-Stokes Raman Scattering (CARS) (Wang et al., 2005) can be sensitive to myelin content and/or structural features such as sheath thickness or internode distance. Despite the high spatial resolution of optical methods, most of these techniques are highly invasive and have limited spatial coverage, rendering them unsuitable for monitoring healthy development, disease progression (e.g. in diffuse demyelination diseases) or treatment response. The characterization of white matter changes in longitudinal clinical studies requires non-invasive high-throughput whole-brain imaging strategies.

While common imaging modalities such as computed tomography or sonography show little myelin contrast (Brant-Zawadzki and Enzmann, 1981), techniques using molecular tracers in positron emission tomography (Frey et al., 1981, Stankoff et al., 2006, Wu et al., 2010), or contrast agents in MRI (Wessig et al., 2007, Frullano et al., 2011) have limited sensitivity and potential risk of toxicity. Magnetic resonance techniques using endogenous contrast agents such as macromolecules (Waldman et al., 2003), phospholipids (Kilby et al., 1991), or metabolite concentrations (Helms, 2001) have limited accuracy due to spectral overlap, and are limited to a qualitative assessment of myelin content.

2.3.1 Strategies for Myelin Contrast Imaging in MRI

Due to its superior sensitivity and excellent soft tissue contrast, ^1H proton MRI of bulk tissue water remains the preferred method for clinical diagnosis and assessment of demyelination diseases (e.g. multiple sclerosis). Changes in myelination during early development can be observed with conventional T1W and T2W images (Miller et al., 2003), while clinical studies often use high resolution T2W images for delineating white matter lesions in multiple sclerosis. Nevertheless, the clinical and pathological specificity of these techniques is limited as contrast changes in T_1 and T_2 weighted images cannot be consistently correlated with underlying changes in myelin (Laule et al., 2007).

To increase the myelin specificity of the MR signal researchers have attempted to isolate the myelin associated water signal based on the T_1 or T_2 spectra of white matter. From multiple images acquired with different echo times during a multi-TE experiment (MacKay et al., 1994) a multi-exponential decomposition of the MR signal consistently reveals multiple water peaks in the T_2 spectrum of white matter, during both in vitro (Swift and Fritz, 1969, Vasilescu et al., 1978) and in vivo (Gersonde et al., 1984, MacKay et al., 1994) experiments. Specifically, the short- T_2 peak ($\sim 30\text{ms}$) is associated with water inside the packed myelin wrappings and is believed to be the result of lengthening of the correlation time of molecular tumbling of myelin associated water confined inside the compact micro-geometry and magnetically interacting with abundant macromolecules. Meanwhile, the longer T_2 peaks are associated with axonal /

extracellular water ($\sim 100ms$) and CSF contamination ($\sim 2s$). The myelin water fraction (MWF) is generally defined as the fraction of signal corresponding to T_2 components between 10 – 50ms normalized to the signal of the entire T_2 spectrum and can be measured quantitatively with the use of an external water standard (Whittall et al., 1997b). In major white matter fiber bundles MWF represents between 15-20% of the total tissue water content. The spatial correspondence between myelin and the short- T_2 water peak has been quantitatively established with histology in a demyelination study (Laule et al., 2006). Moreover, in a nerve injury model, the size of the short- T_2 component was found to correlate with quantitative histological measures of myelin, regardless of the integrity of the myelin microstructure (Webb et al., 2003), suggesting that the short- T_2 peak is sensitive to the content of myelin, regardless of myelin microstructural organization. While the multi-TE technique could potentially provide quantitative myelin imaging with adequate sensitivity for clinical use, its implementation as a high throughput clinical sequence is currently hindered by several technical challenges such as unwanted off-resonance saturation (magnetization transfer) effects in 2D multislice CPMG imaging (Poon and Henkelman, 1992), slow but not negligible exchange of water across different T_2 peaks in the white matter spectrum (Stanisz et al., 1999) and patient safety considerations limiting power deposition (from a train of 180 degree pulses during a CPMG sequence).

An alternative method for selecting myelin water can be proposed with a multi-exponential decomposition of the white matter T_1 (Does et al., 1998, Travis and Does, 2005), using a dual inversion recovery (Villringer et al.) preparation to select the short T_1 ($\sim 820ms$) myelin component. Even though this technique is believed to offer adequate specificity to myelin water ($\cong 90\%$) (Travis and Does, 2005), the long preparation period ($\cong 2.5s$) leads to prohibitively long scan durations for full-brain clinical scans, limiting its application mostly to animal studies (Does et al., 1998, Travis and Does, 2005).

A fast and convenient method to sensitize the MR signal to myelin water can be achieved using a magnetization transfer preparation (Wolff and Balaban, 1989), which takes advantages of the disparate widths of overlapping 1H spectra of free water (width $\cong 1ppm$) and semisolid (associated with macromolecules) proton pools (width $\cong 500ppm$). In short, magnetization transfer preparation uses a broadband off-resonance ($5ppm$) RF pulse to selectively excite and saturate bound hydrogen protons in non-aqueous molecules (e.g. lipids) including macromolecules (hereafter referred to as macromolecules for simplicity) (Henkelman et al., 2001). Following chemical and dipolar exchange of magnetization (Eng et al., 1991) between bound protons (in macromolecules) and neighboring free protons (in free water) the available longitudinal magnetization of free water is reduced and the available water signal is decreased (Henkelman et al., 1993). The magnetization transfer ratio (MTR) can be computed as the ratio of the signal acquired with and without MT preparation and generally reflects both

the concentration of macromolecules and their kinetics of hydration. Since compact myelin tissue contains the majority of macromolecules in large myelinated fiber tracts within human white matter (Baumann and Pham-Dinh, 2001), MT preparation pulses have been successfully used to generate images reflecting myelin content (Pike, 1997, Filippi and Grossman, 2002). Nevertheless, while MT preparation may provides an effective and efficient solution to achieve myelin water weighting, it does not offer exclusive myelin contrast; rather, it has been consistently found that MT contrast in demyelination diseases could be modulated by secondary, epipathophysiological effects, such as inflammation (Brochet and Dousset, 1999), edema or the presence of macrophages (Blezer et al., 2007) obscuring changes of myelin origin.

2.4 Need and feasibility of myelin specific DTI in developmental and translational neuroimaging

While there is a significant increase in DTI applications in clinical neuroimaging research, and techniques to improve the neuronal specificity, none to date have a specific focus on developing a DTI acquisition technique to investigate the microstructural changes in myelin. Given its importance of improving our understanding of white matter maturation, the possibility of acquiring myelin-specific DTI images will have an immediate impact in developmental brain sciences, both in healthy and diseased patients.

Because the maturation of brain white matter (WM) is largely dependent on myelination and is critical for the development of the central nervous system, there is already an extensive body of research work in the past two decades on imaging myelin content as reviewed in the previous section.

However, an understanding of myelin content alone is often not sufficient to understand the maturation process of myelin and brain white matter, as it is often the microstructural changes, in addition to the chemical composition/content, that provide important insight in the functions. For example, as discussed earlier, it is the tightly organized multi-layer myelin sheath structure, in addition to the mere presence of myelin, that improves the insulation of axons for increased conductivity. Further, many white matter disorders are believed to be originating from the microstructural changes (e. g. multiple sclerosis), followed by the eventual content losses (van der Knaap and Valk, 1995). For example, at an early stage of white matter disease onset (e.g. multiple sclerosis), it is very common that the content of a tissue may remain similar and thus MRI negative, however, its microstructure may be damaged as the myelin sheath gradually loses integrity. The ability to construct a diffusion tensor that is myelin specific can have an immediate impact on our better understanding the microstructural myelin changes during healthy brain development and better differentiating its pathological state.

Among the existing MR techniques for myelin water imaging, multi-TE technique is a common and reliable solution to allow multi-exponential fit and subsequent extraction of the myelin water signal, which has short T_2 values (< 50 ms) (MacKay et al., 1994, Whittall et al., 1997a). It needs, however, to be integrated with DTI to allow microstructural assessment of myelin. As it stands now, this technique is not clearly suitable to be incorporated within a DTI acquisition for a clinical examination, because of its long scan duration. Nevertheless, it can provide insight in designing myelin-specific DTI and could also serve as an anatomical standard for structural comparison. Alternatively, because of the large macromolecular concentration in myelin (lipid layers in myelin sheath), magnetization transfer (MT) contrast is often employed to image myelin content (Grossman, 1999, Stanisz et al., 1999, Horsfield, 2005, Laule et al., 2007, Schmierer et al., 2007). Because the MT pulse is inserted before the spin excitation and hence does not affect the acquisition scheme, it can be integrated within a standard DTI pulse sequence and potentially allow myelin specificity.

2.5 Significance of myelin specific DTI in neurological disorders of white matter origin and normal brain development

Given the overall importance of myelin in normal brain development and in many white matter disorders, it will be of great interest to characterize myelin microstructural changes noninvasively. The improved characterization of these changes will likely have a large impact on extending our understanding of pathological and

normal myelin maturation process, and apply this understanding to better differentiate myelin pathology at an early stage in pediatric brain disorders of white matter origins. Indeed, numerous reports have documented anomalous WM integrity in developmental delay. For example, children with attention deficit have lower FA values in the posterior corpus callosum and internal capsule (Nagy et al., 2004) and a variety of WM regions (Ashtari et al., 2005). Generalized developmental delay is associated with higher diffusion and lower anisotropy in the corpus callosum and subcortical WM (Filippi et al., 2003), whereas autism is associated with reduced anisotropy in cortical WM and the corpus callosum (Barnea-Goraly et al., 2004). Fragile X is associated with low anisotropy in only frontostriatal WM and parietal sensory tracts (Barnea-Goraly et al., 2003a), whereas children with velocardiofacial syndrome show reduced anisotropy in the parietal, frontal, and temporal lobes (Barnea-Goraly et al., 2003b).

An area of particular promise for clinical applications of myelin-specific DTI may be in autism spectrum disorders (ASD), which affect 1 out of every 150 children (Fombonne, 2003). There is now considerable evidence that the white matter volume in autism is enlarged (Davidovitch et al., 1996, Lainhart et al., 1997, Stevenson et al., 1997). Of great interest for understanding macroscopic brain development in autism is the recent potential to map changes in WM tracts in the developing brain (Herbert et al., 2004, Lee et al., 2007, Sundaram et al., 2008). Structural MRI studies of autism have focused on regions of interest that may not be as informative as connections between

brain systems. Although DTI has not yet been applied to the longitudinal study of brain development in normal and disease populations such as autism, it is clearly a “powerful method for studying the process of brain development, with both scientific and clinical applications” (Mukherjee et al., 2002). Further, the myelin-specific DTI may be of particular importance in studying brain development in autism where it has been suggested that the fundamental pathology is more widely based in the brain micro-circuitry development modulated by myelination, at the level of neuronal processes (Polleux and Lauder, 2004), and may be the result of ‘functional under-connectivity’ across large-scale cortical networks (Koshino et al., 2005, Just et al., 2007). It is thus of high importance to be able to investigate the respective time courses of myelin development in children with developmental disorders such as ASD.

Finally, it should be noted that the possibility of myelin microstructural imaging can also have wide applicability in white matter diseases in general. For example, it may be used for detection of early demyelination process in multiple sclerosis where myelin content and axonal integrity are still intact, but the myelin sheaths are losing integrity and diffusion anisotropy.

Chapter 3: Initial effort toward myelin specific DTI using Magnetization Transfer preparation and stimulated echo

In this chapter we describe our development, implementation and evaluation of a magnetization transfer MT prepared stimulated-echo diffusion tensor imaging (DTI) technique that can be made sensitive to the microanatomy of myelin tissue. We first discuss the use of stimulated-echo acquisition mode (STEAM) to preserve significant signal from the short T_2 component (myelin water), and magnetization transfer (MT) preparation to further achieve additional differentiating sensitization to this signal. Next we present the implementation of the MT prepared DTI-STE pulse sequence and the development of a robust methodology for deriving a myelin water weighted (MWW) diffusion tensor. Finally we interpret our preliminary results in healthy human controls (Avram et al., 2008, 2009, Avram et al., 2010c) and multiple sclerosis patient (Avram et al., 2010a) and discuss the limitations in terms of sensitivity and specificity of this method.

3.1 Reducing the echo time in DTI using stimulated echo

The clinical standard for diffusion tensor imaging protocols uses a single-shot twice-refocused spin echo (Reese et al., 2003b) EPI DTI pulse sequence, with parallel imaging (Pruessmann et al., 1999). This technique is a variation of the conventional spin echo diffusion sequence (Fig. 2) that refocuses the diffusion weighted signal twice to mitigate image distortions due to eddy currents generated by imperfect diffusion

encoding gradient pulses. While this method consistently provides great image within several minutes, the use of two 180 refocusing pulses requires echo times as long as 100ms, thereby greatly diminishing the signal from myelin water, which has short T_2 (~35ms).

In stimulated echo acquisition mode the separation between diffusion encoding gradient pulses can be increased thus accommodating the same diffusion sensitization within much shorter echo times (Merboldt et al., 1985). Figure 7 compares the minimum achievable echo time for the twice refocused spin echo (TRSE) and stimulated echo (STE) sequences with echo planar imaging EPI readout as a function of diffusion sensitization (b-value). The simulation uses gradient pulses with a maximum amplitude of 5G/cm and slew rate of 120 T/m/s, and a duration of $T_M=120$ ms for the mixing time of the stimulated echo. In practice, to minimize echo time and mitigate image distortions due to field inhomogeneities the readout duration of the single-shot EPI acquisition is reduced both by undersampling the k-space along the phase encoding direction (parallel imaging) and by leveraging k-space symmetries (partial Fourier acquisition). To reflect these standards, an echo delay of only 12 ms from the beginning of the readout was assumed. The significant echo time reduction of the stimulated echo diffusion encoding scheme can be appreciated for all b-values. For example, to accommodate a diffusion sensitization of 1000 a minimum echo time of 86ms is required for the twice refocused spin echo (TRSE) EPI while only 47ms with stimulated echo (STE) EPI (45% smaller).

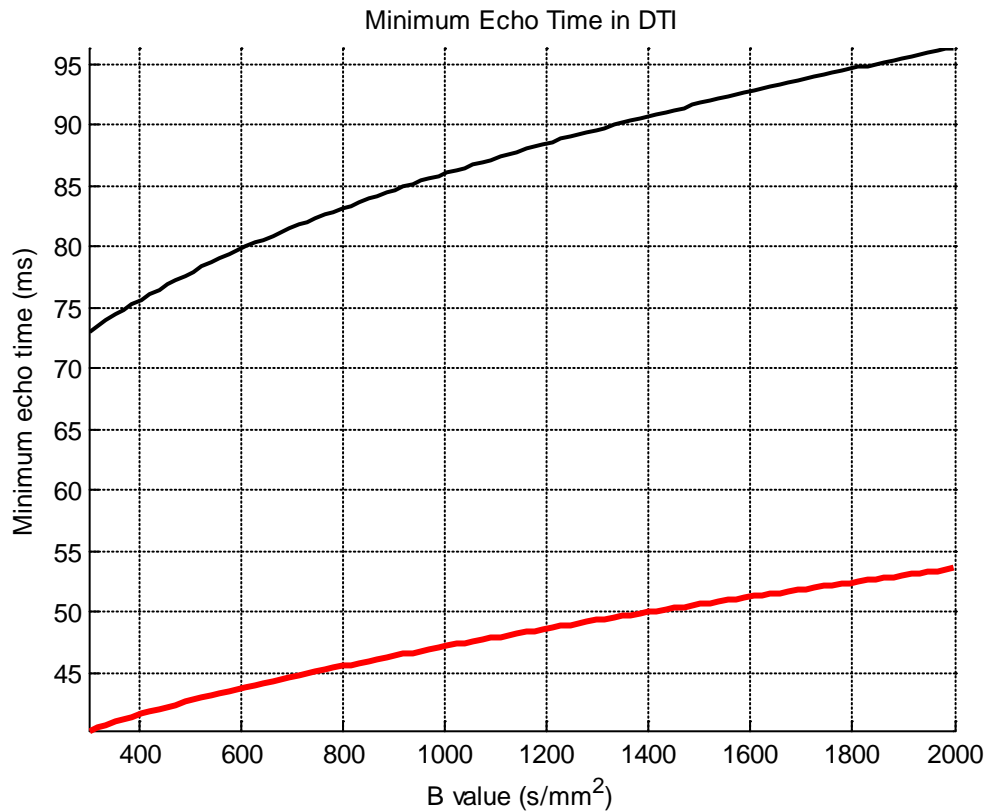


Figure 7: Comparison of minimum achievable echo time dependence on diffusion sensitization for clinical twice refocused spin echo (TRSE) EPI (black) and stimulated echo (STE) EPI (red) pulse sequences. A maximum gradient amplitude of 5 G/cm and slew rate of 120 T/m/s were used. For the stimulated echo the mixing period of TM was 120ms. For the EPI readout, a 12 ms delay from the beginning of the acquisition window was used.

Clearly, the short echo time (TE) enabled by the stimulated-echo acquisition preserves significantly more signal from myelin water. However, contributions from the longer T₂ components are still dominant. To achieve further differentiating sensitization to myelin water, it is necessary to integrate stimulated echo DTI with a separate MR method for achieving myelin contrast.

3.2 Sensitizing DTI to myelin water using magnetization transfer

As briefly discussed in the previous chapter, many techniques have been developed to achieve myelin-weighted contrast, such as multi-echo time (TE) imaging (MacKay et al., 1994), double inversion recovery (Travis and Does, 2005) or magnetization transfer (Wolff and Balaban, 1989). Among them, multi-TE imaging is used as a common and reliable technique for imaging myelin water quantitatively (MacKay et al., 1994). Specifically, a T_2 spectrum is derived from measurements at multiple TEs and the myelin water signal is modeled as the short T_2 component (<50 ms).. The limitations for multi-TE imaging, however, are the long scan time and the additional requirement to reach very short TEs, which currently is problematic with DTI. The DIR method is based on the short T_1 of myelin and requires a lengthy (e.g. 2 s) preparation pulse, making it impractical for a whole-brain clinical DTI scan (Travis and Does, 2005). The MT technique, which uses an off-resonance radiofrequency pulse to selectively excite and saturate bound hydrogen protons in non-aqueous molecules including macromolecules (hereafter referred to as macromolecules for simplicity), leads to reduced longitudinal magnetization of free water molecules after they exchange magnetization with the saturated protons. Since myelin tissue contains the majority of macromolecules in large fiber tracts within the white matter (Baumann and Pham-Dinh, 2001), MT preparation pulses have been successfully used to differentiate myelin water signal and generate images reflecting myelin content (Pike, 1997, Filippi and Grossman,

2002). While MT preparation may not generate exclusive myelin contrast, it does offer a reasonably effective and efficient solution to achieve sufficient myelin water weighting, making it a prospective candidate to be incorporated into DTI acquisition for the investigation of myelin microstructure.

Two recent studies have already demonstrated that MT preparation can be incorporated into diffusion weighted imaging to investigate the diffusion characteristics of water associated with macromolecules in vivo (Mulkern et al., 2005, Ronen et al., 2006). Mulkern et al. attempted to validate the tissue specificity of the bi-exponential diffusion model (fast and slow) using differential magnetization transfer effects in human subjects. The authors concluded that two components derived from a bi-exponential diffusion fit could not be interpreted as separate compartments associated with intra and extra-cellular water. In an animal study (anesthetized cat brain), Ronen et al. on the other hand, found that MT can change the volume fractions of the fast and slow diffusion components at longer irradiation times. However, most in vivo myelin images to date, including the two studies above, have been acquired with non-tensor based measurements. Therefore they are only sensitive to the content of myelin, and not to the microscopic organization of the myelin sheaths. As it is generally known, the demyelination process often begins with a gradual unwrapping of the myelin sheaths during inflammation or edema (Gareau et al., 2000, Laule et al., 2004) rather than a decay of the myelin content. As a result, the myelin maps acquired thus far can detect a

reduction in myelin content occurring at late stages of demyelination (Baumann and Pham-Dinh, 2001), but could fail to characterize early-state microstructural changes in myelin sheaths (Barkovich, 2000). Thus, means to detect myelin microstructural changes, which would reflect this early unwrapping process, will be potentially valuable for an early detection of white matter developmental disorders and will help deploy early interventions that have proven to be critical in treating white matter diseases.

To this end, we propose a new method that can lead to improved assessment of myelin microstructure. In particular, we describe our development and implementation of a myelin-weighted DTI pulse sequence that preserves sufficient myelin signal and allows the estimation of a myelin water weighted (MWW) diffusion tensor. Because of its short T_2 , myelin water signal decays rapidly and cannot be detected with traditional DTI techniques. As such, we specifically implemented a stimulated-echo DTI SENSE acquisition scheme (Rane et al., 2010) capable of much shorter echo times to preserve significant signals from the short T_2 proton pools. We further incorporated an MT preparation pulse which would provide differential sensitization to the myelin water. It is hoped that this new combined strategy can potentially be used to detect and quantify changes in anisotropy associated with the myelin microstructure, which would better our understanding of the white matter maturation process during human brain development in healthy populations, and improve the early diagnosis of demyelination process in white matter diseases.

3.3 Pulsed Magnetization Transfer for in vivo Myelin Water Weighting

The MT preparation in our experiment consisted of a spatially non-selective MT module (Fermi pulse, 2500 Hz offset, 1080 degrees flip angle), which was repeated every 300ms before each slice was acquired. The preparation scheme was consistent throughout our experiments including the DTI acquisitions.

Although MT preparation can allow significant weighting on myelin water signal, it does not achieve exclusive myelin contrast due to the presence of other macromolecules throughout brain tissue and the potential exchange mechanisms among various proton pools (Stanisz et al., 1999). To evaluate and quantify the effect of our MT preparation on achieving myelin water weighting, we first carried out experiments employing multi-TE acquisitions. Indeed, previous studies have shown that images at different TEs can be used to obtain an accurate estimate of the T_2 spectrum of water in different pools (MacKay et al., 1994). Specifically, it has been shown that there are three components indicative of the compartmentalization of proton pools in three different tissue environments. For white matter under physiological conditions, pools with short T_2 (<35ms) have been associated with myelin water, those with intermediate T_2 (35-120ms) have been associated with axonal and intra/extra cellular water, while those with long T_2 (>120ms) represent CSF. A detailed model of MT suppression of the short and intermediate/long T_2 components of bovine optic white matter was developed by Stanisz

et al. It was found that the efficiency of the MT transfer in bovine optic nerve specimen is in fact nine times larger in the short T_2 component than in the intermediate/long T_2 component associated with intra and extracellular axonal water (Stanisz et al., 1999).

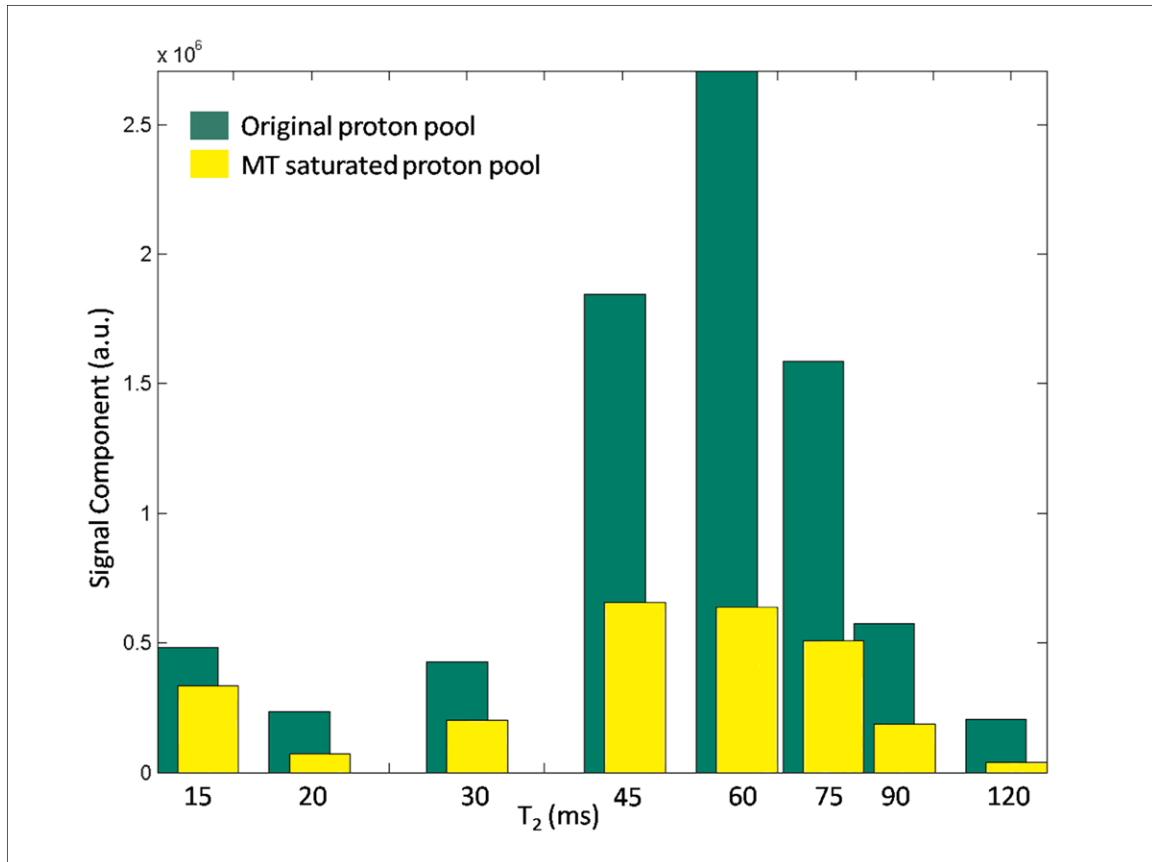


Figure 8: Pulse sequence schematics for the magnetization transfer prepared stimulated echo DTI. Spatially non-selective Fermi-shaped MT pulse is played out with a repetition time of 300ms in a multi-slice stimulated echo acquisition with diffusion weighting; TE/TM/TR = 34/135/4500 ms, 15 slices, $b = 600$ sec/mm². The colors correspond to the MT crushers (blue), diffusion encoding (red), slice selection (green) and readout (orange) gradients. A spatial-spectral pulse (not shown here) was used for excitation.

To validate the effectiveness of the MT preparation in selecting myelin water, we carried out control experiments to quantify its effect on the different white matter T_2 components. Specifically, two sets of multi-slice (64x64x33 matrix) single-shot spin-echo

measurements were performed at different TEs (TE/TR=18, 20, 22.5, 25, 27.5, 30, 32.5, 35, 37.5, 40, 45, 50, 55, 60, 65, 70, 75, 80, 90, 100, 110, 125, 150 and 200 ms/9.9s), one set with MT module turned on, and the other one off. Images were acquired separately for every TE to avoid echo train instabilities and diffusion effects that may arise from a CPMG sequence (Carr and Purcell, 1954, Meiboom and Gill, 1958). For every voxel in the major white matter fibers the measured T_2 decay curve obtained with MT preparation was subtracted from that obtained without MT to retrieve the signal due only to the saturated spins. The curves were fit using the non-negative least squares method in MATLAB 7.0 (The MathWorks, Inc., Natick, MA), to obtain the T_2 spectra of the original proton pool (MT off) and the MT saturated pool. The signal components at each T_2 bin were quantified to assess the effect of the MT pulse on the short and intermediate T_2 components (Fig. 8).

In vivo studies have reported that the application of the MT pulses can decrease the white matter signal on a proton density weighted image by approximately 25-35%. This finding was confirmed in our experiments as comparable signal suppression was found in main fiber tracts. It is however unlikely that this large change is exclusively specific to myelin water, as the amount of myelin water has been estimated by in-vivo measurements to be no more than 15% of the proton density signal in major fibers (Mackay et al., 1994). Saturation of axonal macromolecules and exchange between myelin and axonal water are possible explanations for the limited specificity of MT to

myelin water (Stanisz et al., 1999). Significant MT effect was observed in gray matter as well (15-20%). However, since this effect was mainly due to non-myelin specific macromolecules, we excluded these regions and focused our analyses on the major fiber tracts with a minimum MTR of 25%.

In order to quantitatively assess the specificity of the MT preparation to myelin water we derived and compared the white matter T2 spectrum of the total pool of protons with that of the saturated proton pool. The region of interest (Ducreux et al.) used for this analysis contained major fiber tracts with a high degree of myelination (i.e. genu and splenium of the corpus callosum, superior longitudinal fasciculus, and corticospinal tract) and no CSF contamination. For the multi-TE dataset measured without MT irradiation a non-negative least square fit was performed for every voxel (Vavasour et. al., 2000). The same fitting procedure was applied on the difference signal of the two multi-TE acquisitions. The histogram in Fig. 8 shows the T2 spectra within the selected major fiber tracts in a representative subject. The same tracts were used and illustrated in Figs. 10 and 11. As expected, a clear differential sensitivity was observed in the short T2 signal, resulting in significant myelin water weighting. The ratio of the short T2 peak (<35ms) to the intermediate T2 peak (>35ms) was 23% in the saturated pool, compared to 14% in the initial pool containing all the spins. These results are comparable with previous studies (Stanisz et al., 1999). Since the specificity in the saturated pool is significantly larger than that in the total proton pool, the tensor

estimation of the directional diffusion of the saturated pool should also be significantly weighted by myelin water contributions.

3.4 Magnetization Transfer prepared stimulated echo DTI pulse sequence

To preserve the short T_2 component (i.e. the myelin water signal), we developed a stimulated-echo (STE) DTI sequence with a single-shot EPI acquisition (Rane et al., 2010) and parallel imaging SENSE capabilities. The same MT preparation scheme described above was incorporated into the DTI sequence allowing for the saturation of myelin water spins (Fig. 9). A b-value of 600 s/mm^2 was achieved in our STE DTI sequence within a TE of 34 ms using SENSE acceleration (factor of 2) and partial Fourier acquisition (0.66 k-space coverage). A multi-slice acquisition scheme was used to allow increased MT effect as the result of repetitive spatially non-selective MT modules. Using a TR of 4.5s with 15 slices for the DTI scans the same 300ms pulse repetition period for the spatially non-selective MT module was maintained. Two scans were acquired - with and without MT preparation. In both scans, all other imaging parameters were identical (TE/TM/TR = 34ms/135ms/4500ms, 19 directions, b-value 600 s/mm^2 , matrix size 64×64 , 20cm field of view (FOV), 5mm slice thickness, 15 slices, 5 averages). In addition, proton density weighted images (TE/TR=18/9900ms) were acquired and the MTR maps were computed. Subsequently, MWW tensors were derived from both DTI and PD images. For comparison, clinical twice refocused spin echo (TRSE) DTI images with the same b-

value of 600 s/mm^2 (but with an intrinsically larger $\text{TE}=70\text{ms}$) were acquired. Finally, to observe the preferential effect of MT preparation on different T_2 species, we performed an additional control experiment. In the same session we acquired STE-DTI images at $\text{TE}=34\text{ms}$ ($\text{NEX}=2$) and $\text{TE}=80\text{ms}$ ($\text{NEX}=5$) with and without MT. Contrary to the short TE experiments, there was a very low signal difference between the MT and non-MT prepared acquisitions when long TE ($\text{TE} = 80\text{ms}$) was used. Consequently, the tensor fitting procedure for the MWW tensor at long echo time failed to yield positive definite diffusion tensors in the main fibers, implying that the MT preparation is preferentially sensitive to short T_2 proton pools in these regions.

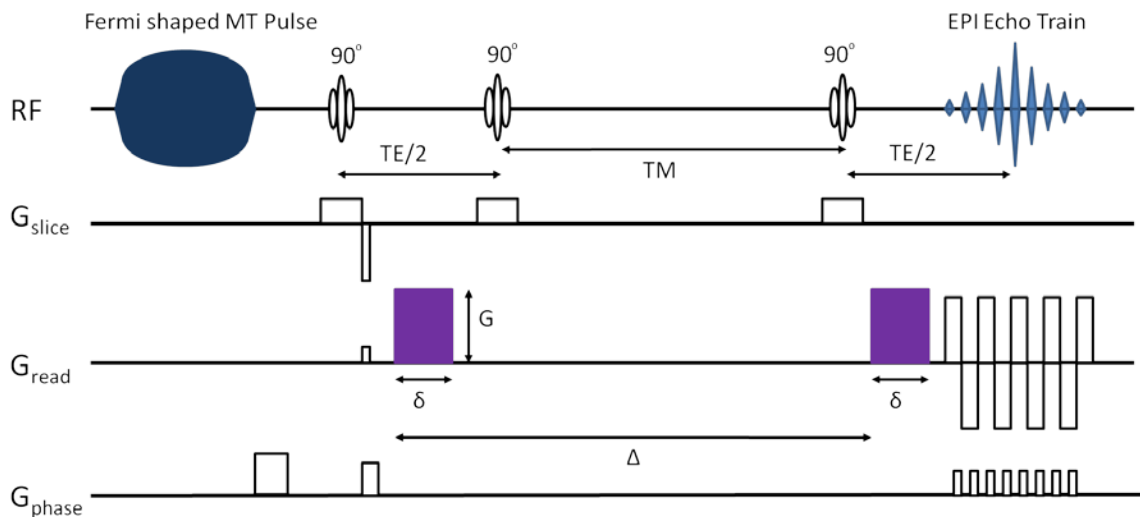


Figure 9: Pulse sequence schematics for the magnetization transfer prepared stimulated echo DTI. Spatially non-selective Fermi-shaped MT pulse is played out with a repetition time of 300ms in a multi-slice stimulated echo acquisition with diffusion weighting; $\text{TE}/\text{TM}/\text{TR} = 34/135/4500 \text{ ms}$, 15 slices, $b = 600 \text{ s/mm}^2$. The colors correspond to the MT crushers (blue), diffusion encoding (red), slice selection and readout (orange) gradients. A spatial-spectral pulse (not shown here) was used for excitation.

3.5 Processing strategy for robust Myelin Water Weighted (MWW) DTI

Because a simple image subtraction will not be sufficiently robust to model the diffusion tensor for the proton pools that are influenced by the MT preparation, especially under low SNR conditions, we developed a new processing strategy. For an experiment with sufficiently long TR, the diffusion weighted signal due to the MT saturated spins can be written as:

$$S_{i,\Delta MT} = S_i - S_{i,MT} = P e^{-\frac{TE}{T_2}} e^{-b_i D} - P_{MT} e^{-\frac{TE}{T_{2,MT}}} e^{-b_i D_{MT}} \quad (3.1)$$

where S_i is the measured DW signal along diffusion encoding direction i , P represents the proton density and the subscripts $_{MT}$ and $_{\Delta MT}$ respectively refer to the spins remaining after the application of MT and those that were saturated during off-resonance irradiation (i.e. which make up the myelin water weighting signal). The magnitude change due to the diffusion of the MT selected protons becomes:

$$e^{-b_i D_{\Delta MT}} = \frac{S_{i,\Delta MT}}{S_{0,\Delta MT}} = \frac{P e^{-\frac{TE}{T_2}} e^{-b_i D} - P_{MT} e^{-\frac{TE}{T_{2,MT}}} e^{-b_i D_{MT}}}{P e^{-\frac{TE}{T_2}} - P_{MT} e^{-\frac{TE}{T_{2,MT}}}} \quad (3.2)$$

In order to make the fitting procedure more robust in the presence of low SNR, we make the assumption that the application of MT does not significantly alter the average T_2 of white matter at 3T (i.e. $T_2 \approx T_{2,MT}$). This is reasonable since the amount of myelin water within even the most myelinated tracts is only 15% (MacKay et al., 1994), and moreover, the TE used in this experiment is short relative to either T_2 or $T_{2,MT}$. Thus, Equation 3.2 can be re-written as:

$$e^{-b_i D_{\Delta MT}} \approx \frac{P e^{-b_i D} - P_{MT} e^{-b_i D_{MT}}}{P - P_{MT}} = \frac{P \frac{S_i}{S_0} - P_{MT} \frac{S_{i,MT}}{S_{0,MT}}}{P - P_{MT}} \quad (3.3)$$

which can be reliably fitted with a tensor:

$$D_{\Delta MT} \approx (\mathbf{b}^T \mathbf{b})^{-1} \mathbf{b}^T \left[-\ln \left(\frac{P \frac{S_i}{S_0} - P_{MT} \frac{S_{i,MT}}{S_{0,MT}}}{P - P_{MT}} \right) \right] \quad (3.4)$$

This fitting procedure presents several advantages over other methods such as the two-compartment diffusion model with a bi-exponential decay (Mulkern et al., 2005, Ronen et al., 2006). Firstly, Gaussian probability distribution of phase shifts is not assumed for either of the two sets of diffusion measurements. It is only in the last step that a Gaussian tensor is fitted directly on the diffusion weighted signal derived for the population of interest. Therefore, the model is readily extensible with advanced DTI analysis methods such as higher order tensors (Liu et al., 2010) or crossing fibers. Secondly, compartmentalization of two pools is not necessary; the model remains valid even in the presence of exchange, which cannot be excluded for long diffusion time.

3.6 In vivo myelin water weighted (MWW) DTI has larger diffusion anisotropy compared to conventional DTI

Diffusion tensors were estimated for the two DTI measurements (with and without MT), as well as to the saturated spins using the model described in the methods section. The diffusion properties of these tensors were compared to those obtained with a clinical TRSE DTI sequence at the same b-value. All datasets used to derive diffusion

tensors had a minimum SNR of 23 which ensures consistency of the fractional anisotropy (FA) (Farrell et al., 2007). To guarantee sufficient SNR, the MWW diffusion tensor was estimated in major fiber tracts with at least 25% MTR.

At a first glance, the colored FA maps (Fig. 10) derived from TRSE DTI, STE DTI and MWW tensors appear quite similar in major fiber tracts (i.e. genu and splenium of the corpus callosum, superior longitudinal fasciculus). The main direction of diffusion is similar in all three tensors. This finding is consistent with the structural arrangement of myelin sheath wrapping around the axons, which renders water diffusion faster along the sheath and slower across, resulting in the same principal diffusion direction as that of the axons.

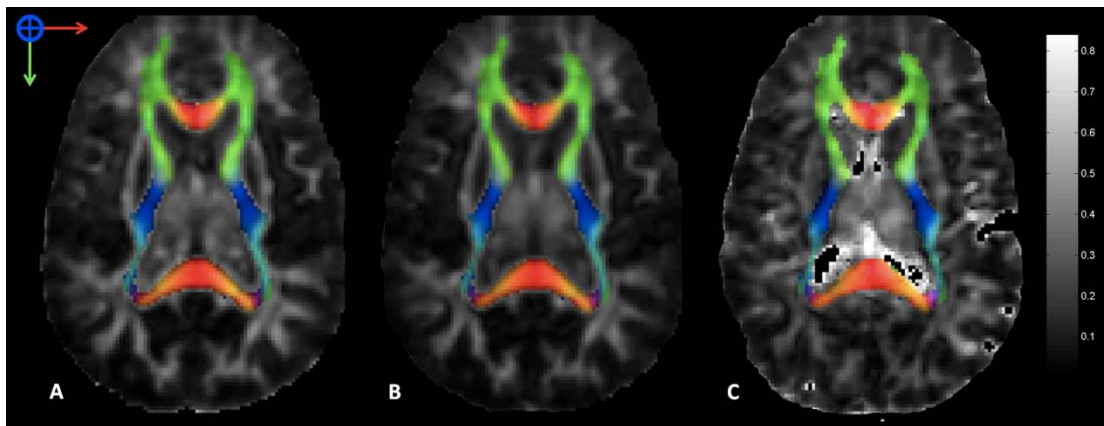


Figure 10: In white matter tracts, the main directions of diffusion are similar for the TRSE-DT (A), the STE-DT (B), and the Myelin Weighted Water tensor (C). Due to the very small MT effect in regions of the ventricles with large CSF partial volume, the MWW tensor was derived from very low signal levels and therefore the FA values for these regions exhibit large variations as shown.

Further analysis was conducted on the FA and diffusivity components within the same major fibers. As shown in Fig. 11 (A,B), the FA values for main fibers in the

stimulated echo DTI dataset were indeed very similar, as expected, to those obtained from the DSE DTI tensor. In contrast, the computed myelin water weighted (MWW) tensor showed an average increase of 5.2% in the FA of the MT saturated spins in white matter, suggesting that the diffusion of myelin water is more anisotropic than that in axonal water. The increase in FA was more pronounced in the genu and splenium of the corpus callosum where the myelinated fibers were more aligned (less divergent) within the voxel compared to other tracts in the slice Fig. 11 C.

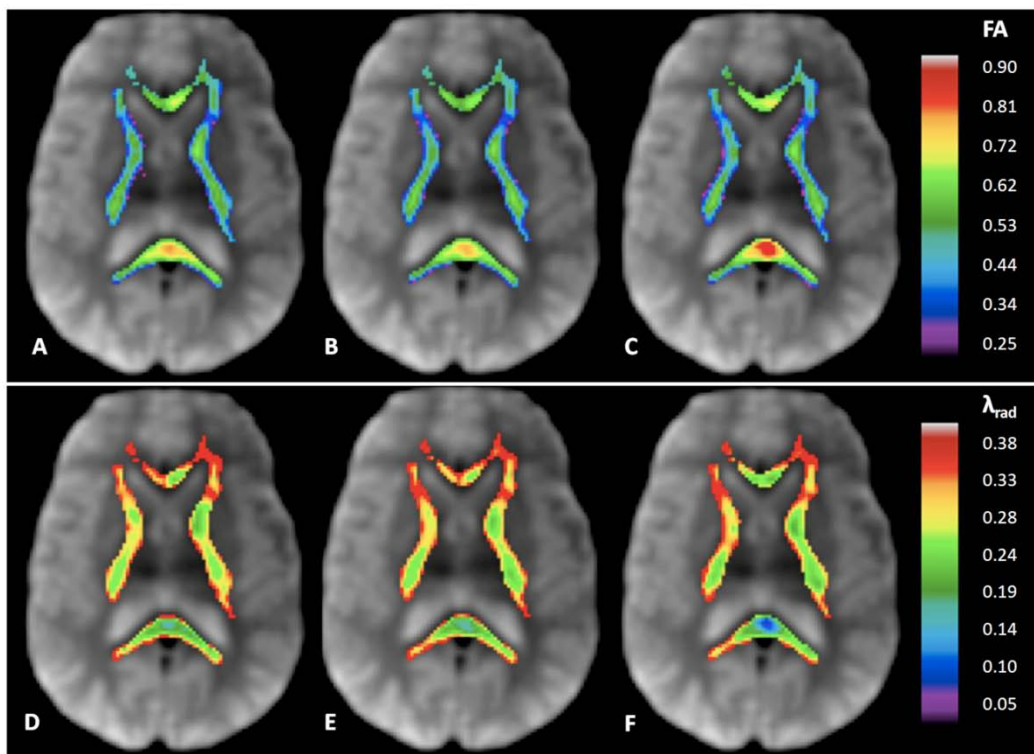


Figure 11: Fractional anisotropy and radial diffusivity ($\mu\text{m}^2/\text{ms}$) maps for white matter. Top row FAs, bottom row radial diffusivities (from left to right TRSE-DT, STE-DT, and MWW tensor respectively). MWW diffusion tensor shows larger FA, mainly due to a significantly smaller radial diffusivity.

To further investigate the cause of the observed change in FA, the diffusivities (axial, radial and mean) for the three tensors were compared. It was found that the

larger FA in the MWW tensor could be attributed mainly to a decrease in its radial diffusivity (~11.1% on average), suggesting that myelin water undergoes a more restricted Brownian motion trans-axially compared to axonal water (Fig. 11: D, E, F). No significant differences were observed in the axial diffusivities of the three tensors, while the mean diffusivity decreased slightly for the myelin water weighted tensor (5.78%), in accordance with the decrease of radial diffusivity. The results were similar across two repeated sessions (within each session four independent measurements were made); specifically there was a $6.6 \pm 2\%$ increase in FA and a $11.1 \pm 0.1\%$ decrease in radial diffusivity relative to the clinical DSE-DTI sequence. To further quantify the differences in FA and radial diffusivity, a path ROI was drawn along the splenium of the corpus callosum where the degree of myelination and MTR were the largest. Fig. 12 shows the FA and radial diffusivities as a function of distance along the path. At the center of the splenium, the anisotropy experiences a significant increase (max: 24.6%; mean 9.9%) for MWW tensor (red) when compared to those derived from the STE (green) or DSE (blue) DTI images. This is due to a significantly smaller radial diffusivity (max 49.5%; mean 20.5%) in the myelin water weighted tensor.

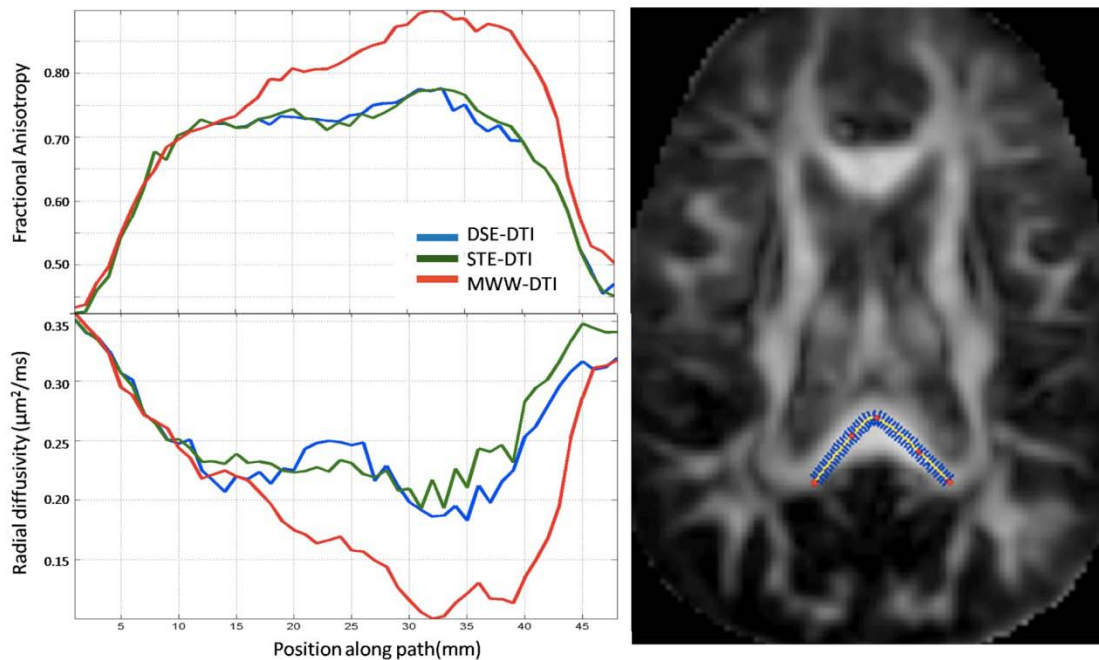


Figure 12: FA and Radial diffusivity along a path through the splenium of corpus callosum. Myelin water tensor (red) shows larger FA and smaller radial diffusivity than the either STE DTI tensor (green) or clinical DSE DTI tensor (blue)

Overall, the measured FA and diffusivity values are comparable with previous in vitro measurements of myelin water diffusion anisotropy conducted in non-human peripheral nerves (Stanisz and Henkelman, 1998, Peled et al., 1999, Andrews et al., 2006a). The initial measurement of short T₂ water diffusion properties (Stanisz and Henkelman, 1998) revealed little anisotropy in the short T₂ component and unexpectedly large apparent diffusion coefficient (ADC). Later, a detailed study by Peled et al found some restriction in the short T₂ signal and an intermediate component that was attributed, at least in part, to interstitial water as it exhibited little restriction and relatively large diffusivity (Peled et al., 1999). More recently, Andrews et al reported results similar to ours: a larger anisotropy in short T₂ component due mainly to a

reduced radial diffusivity. With a T_2 based selection method for myelin water the axial diffusivity measured in the short T_2 signal was only slightly smaller than that of the intermediate/long T_2 component (Andrews et al., 2006a). The large discrepancies between these different studies might be due to several factors such as nerve specimens, temperature control, preparation method, fitting procedure, myelin selection, data acquisition etc. Our current study differs from these in that it uses pulsed MT to image (not only measure) the diffusion anisotropy in the human central nervous system (CNS) in vivo. As a result, our MT preparation, diffusion encoding and acquisition efficiency (number of echoes) are limited by clinical safety considerations.

It is worth noting that, because myelin water and axonal water appear to have the same main directions of diffusion, there might be a particular demand for tissue specificity in DTI. Many tissue-specific proton pools (e.g. myelin water) that contribute to the measured anisotropy in white matter might have diffusion tensors oriented along the direction of the axon. Thus, characteristics of myelin water diffusion cannot be fully obtained even by using advanced methods specifically aimed at solving multiple tensors such as HARDI (Frank, 2001, Tuch et al., 2002). Instead, specific selection of myelin water protons is required.

The method presented above can be readily combined with other advanced DTI techniques to better characterize myelin microstructure. For example a longer experiment with more diffusion encoding directions (and/or b-values) can be used to

derive a higher order tensor for the myelin water (Liu et al., 2010). Even though the first order tensor derived in this manuscript has the same orientation as the regular DTI, metrics in higher order tensors could be even more sensitive to changes in myelin anisotropy during early pathology.

3.7 Myelin Water Weighted DTI can better differentiate between WM lesions in multiple sclerosis patient

A patient diagnosed with relapsing-remitting multiple sclerosis was scanned with the DTI sequence both with and without the MT preparation while all other scan parameters were kept constant: TE/TR=38/4500ms, 15 slices with 2x2x5 mm³ resolution, b=500 s/mm², 15 directions, 8 averages. The parameters of the off-resonance Fermi shaped MT pulse were: offset=2.5kHz, flip=1080 degrees. Spin echo based proton density images with the same MT preparation on and off were used to compute the MTR map (TE/TR=20/10000ms). The MTR map along with the DTI data sets was then used to retrieve the myelin water weighted (MWW) diffusion tensor of the spins that have exchanged magnetization during the off-resonance MT irradiation. In addition, diffusion tensors were fitted separately to the two stimulated echo DTI acquisitions (with and without MT). The SNR of the calculated myelin water tensor was MTR dependent and ranged between 40% and 60% of the SNR of a single stimulated echo DTI acquisition. Finally, for comparison, a standard clinical twice refocused spin echo (TRSE) single-shot EPI DTI measurement was performed with similar parameters as the

stimulated echo sequences: TE/TR=70/4500 ms, resolution 2x2x5 mm³, b=500 s/mm², 15 directions, one average.

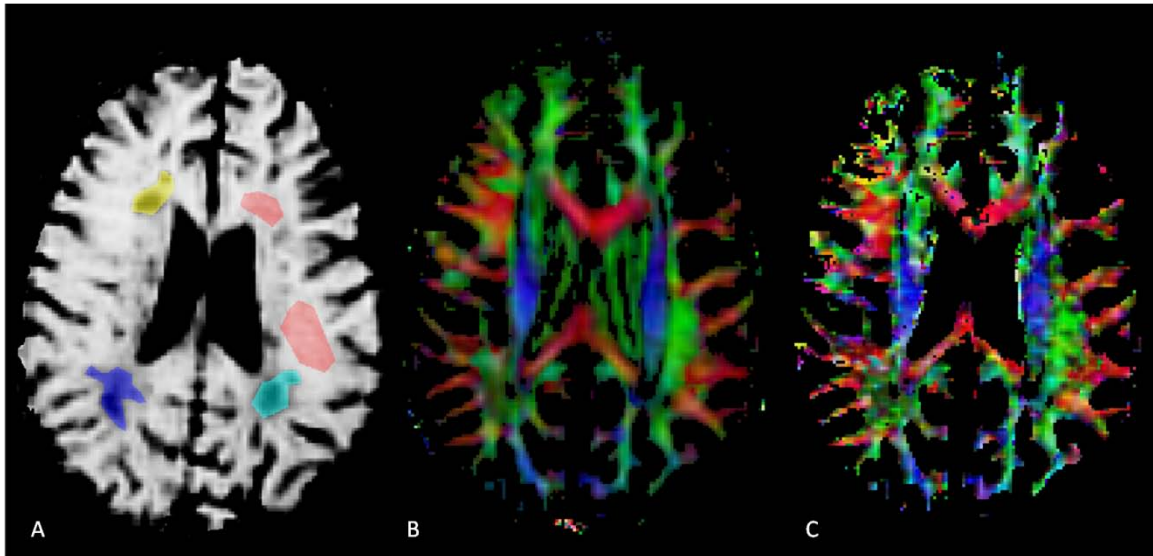


Figure 13: Myelin Water Weighted Diffusion Tensor Imaging in Multiple Sclerosis patient. Three lesions - left posterior (LP), right posterior (RP) and left anterior (LA) - shown in blue, cyan and yellow respectively, as well as normal appearing white matter (NAWM) in red were identified based on the T2W and MTR (A) maps. The colored FA maps for MWW-DTI (C) shows more heterogeneity across lesions, when compared to the colored FA of the conventional DTI (B), suggesting that the MWW-DT might provide a better characterization of WM lesions in multiple sclerosis (MS).

Four regions of interest ROIs were drawn on the T₂-weighted images: three in white matter lesions with different degrees of demyelination and one in normal appearing white matter (Fig 13: A). The mean FA values were computed in those regions for each of the four calculated tensors (clinical TRSE diffusion tensor, stimulated echo DTI with and without MT and myelin water weighted (MWW) diffusion tensor). As expected, in all four ROIs average FA values in the stimulated echo DTI acquisition were larger than those in the clinical DSE DTI measurement, suggesting that indeed a shorter TE provides increased contribution from myelin water. Furthermore, when MT was

turned on removing the contribution of most myelin water to the diffusion tensor, a decrease in the average FA was observed. Most importantly, the FA values in the estimated diffusion tensor due to the myelin water spins vary more significantly across lesions with different degrees of myelination (MTRs). Because the calculated myelin water anisotropy is more specific to the changes in myelin microstructure it could provide a more accurate differentiation of white matter lesions in early stages.

Table 1: Myelin water weighted diffusion tensor obtained using the magnetization transfer prepared stimulated echo DTI sequence can better differentiate between white matter lesions (LP - left posterior, RP - right posterior, LA - left anterior) in multiple sclerosis.

ROI	MTR(%)	FA				
			TRSE-DTI	STE-DTI	MT-STE-DTI	MWW-DTI
NAWM	30.6	0.47	0.51	0.49	0.56	
LA	26.1	0.28	0.26	0.25	0.40	
RP	23.9	0.22	0.25	0.24	0.29	
LP	23.4	0.22	0.25	0.23	0.32	

Our preliminary results, based on a new DTI pulse sequence with greatly shortened echo times, demonstrate that it is possible to preserve sufficient myelin signal. Moreover, the myelin water anisotropy shows a clear reduction in FA in the lesions as compared to the healthy white matter. There is also a better differentiation in FA values within the three lesions that can potentially be correlated to the disease progression. In comparison, the FA values in conventional DTI did not indicate any significant differentiation, most likely due to the lack of myelin signal.

3.8 Need for Improved Specificity and Increased Sensitivity

We have thus far described our effort and demonstrated effectiveness in achieving myelin water weighting within the realm of DTI. While its initial promise is clearly illustrated, there are remaining issues to be addressed before this new strategy can be widely applied in translational and clinical applications. Chief among these are concerns regarding the specificity and efficiency of the MT module, as well as the relatively low SNR of the MWW DTI images.

As shown in many previous studies, MT contrast reflects, in part, the amount of myelin especially in main fiber tracts of white matter, and can thus be used to characterize white matter pathologies (Pike, 1997, Filippi and Grossman, 2002). Although it is theoretically straightforward, the actual implementation to maximize myelin weighting using MT for clinical applications can be challenging. Most studies that rigorously quantify the myelin specificity of MT were performed with continuous wave (CW) irradiation on animal specimens. While CW irradiation maximizes the amount of saturation this method is not practical in living human subjects because of high Specific Absorption Rate (SAR). Instead, pulsed MT is often used. In this case, the magnetization transfer effects are driven to a steady state which is modulated by additional exchange processes between pools with different relaxation rates. Even though the transfer of magnetization in myelin water is nine times more efficient than in the intermediate T_2 compartment due to higher concentration of non-aqueous molecules

(Stanisz et al., 1999), exchange between myelin water and axonal water could limit the specificity of the MT effect to the short T_2 component. In addition, the effect of MT can also be modulated by the kinetics of hydration of macromolecules. For example, some studies suggest that the MTR can be influenced by epiphiopathological processes such as inflammation and edema (Gareau et al., 2000, Laule et al., 2004). Additional experiments by varying different MT parameters can be conducted to further investigate these potential mechanisms.

In our in vivo implementation, multi-slice acquisition was used in conjunction with a non-selective MT pulse for each slice packet allowing an inherent increase in MT effect from repetitive MT preparations. This in turn increases the potential exchange time among the various proton pools. While we are confident that, attributed to the inherent multi-layered myelin structure, the MT preparation still yields significant myelin water weighting as demonstrated in our results, further experiments can be conducted to achieve exclusive myelin water contrast. Exclusive myelin water diffusion measurements can be obtained at the cost of longer acquisition time. For example, the multiple echo time acquisition could be incorporated in a single DTI sequence, allowing the quantitative assessment of diffusion on the entire T_2 spectrum along each encoding direction. The drawback of such an acquisition scheme is that it would require even shorter echo times (below 20ms), thereby limiting the amount of diffusion weighting. Nevertheless, for many clinical applications, measuring a myelin water weighted tensor

is already useful in that it provides valuable information about the myelin microstructure that cannot be obtained otherwise.

In our results, it was found that voxels in major fiber tracts experience a large MT saturation effect up to 30%, resulting in sufficient average SNR to derive myelin water weighted diffusion tensor after averaging (SNR=23). In comparison, however, the STE-DTI tensor after the same 5 averages had an SNR of 132, while the SNR in the DSE-DTI tensor data was 71. Clearly, while the use of STE-DTI greatly shortens the TE for improved SNR, the incorporation of MT saturation to further differentiate myelin water signal is at the expense of sensitivity.

To make this sequence practical for clinical applications increased SNR would be needed. Specifically, using a spiral readout scheme would greatly shorten TEs. For a $b=600$ s/mm² a TE as short as 20ms can be obtained. This reduction in TE further contributes to preserve the myelin water signal. Another benefit of spiral acquisition is the ability to increase spatial resolution without the requirement for longer echo times. The larger imaging matrix may allow us to minimize partial volume effects and also improve specificity. Finally, further sensitization to myelin water can be achieved by reducing the TR, as myelin water is believed to have the shortest T₁ compared to all other T₁ components in human white matter at 3T (Travis and Does, 2005, Labadie et al., 2008).

Chapter 4: Technical development of short-TE Diffusion Tensor Imaging for clinical applications

While the preliminary results obtained with our newly developed magnetization transfer (MT) prepared stimulated echo (STE) DTI pulse sequence illustrate the feasibility of myelin specific DTI, our current method requires increased sensitivity and myelin water specificity before it can be applied widely in clinical applications. To this end, we describe in this chapter the implementation of a robust stimulated echo DTI sequence with segmented spiral-out readout trajectory for achieving minimal TE on clinical MRI scanners. To ensure high spatial accuracy throughout the DTI scan we further develop a methodology for inherently and dynamically correcting both motion induced phase errors and off-resonance effects due to magnetic field inhomogeneities (including eddy currents) in the reconstructed image. We outline our results obtained in healthy volunteers and discuss the potential of this sequence for investigating microstructural changes in myelin tissue.

4.1 Minimizing echo time using a spiral-out readout trajectory

We have seen in the previous chapter that compared to the standard twice refocused spin echo (TRSE) DTI the stimulated echo diffusion encoding scheme minimizes the duration of transverse relaxation significantly reducing the echo time and preserving more signal from myelin water. A further reduction of TE can be achieved by optimizing the readout trajectory.

The conventional echo planar imaging readout uses a Cartesian trajectory to sample the k-space in a rectilinear fashion. To prevent image artifacts due to phase discontinuities, the k-space is covered continuously along the phase encoding direction (e.g. from bottom to top). Consequently, the readout window begins before the center of k-space is covered (i.e. TE - the time of echo formation). In practice, this delay between the start of the readout window and the time of echo formation can be minimized by undersampling the k-space using parallel imaging and partial Fourier encoding. However, even if both strategies are employed simultaneously in a diffusion weighted acquisition with small matrix size, the echo delay cannot be reduced below 10ms without compromising on image quality. To effectively reduce the echo time a center-out k-space sampling strategy is required.

The most common and efficient solution for a center-out acquisition are spiral readout trajectories. Compared to Cartesian techniques (such as EPI), spiral trajectories are more attractive because the efficient use of sinusoidal readout gradients on two spatial dimensions inherently refocus motion- and flow- induced phase errors and generates a sampling pattern with increased encoding capabilities (e.g. randomness of k-space sampling).

Combining the spiral-out readout with a stimulated echo acquisition can drastically reduce the echo time in the DTI measurement. Figure 14 (A) compares the minimum achievable echo time for the twice-refocused spin echo EPI and the stimulated

echo spiral sequences as a function of diffusion sensitization (b-value). Diffusion encoding gradients with 5G/cm amplitude and 120 T/m slew rates were assumed. The simulation uses a very conservative value of 7ms pre-echo delay for the partial-Fourier EPI readout and a 120ms longitudinal period (mixing time) for the stimulated echo. It is evident that combining stimulated echo acquisition with spiral-out readout minimizes the echo time in DTI, enabling TEs as short as 20ms on commercial whole body clinical scanners.

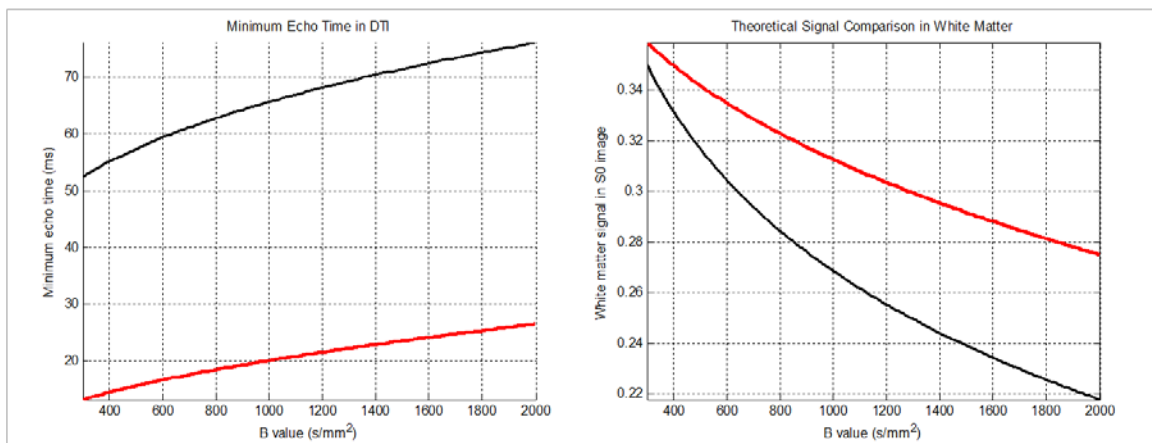


Figure 14: A. Minimum echo time achievable with twice refocused spin echo (TRSE) EPI DTI (black) and STEAM spiral DTI (red). B. Theoretical normalized white matter SNR comparison between the clinical TRSE EPI DTI and STEAM spiral DTI. For STEAM spiral DTI the duration of the longitudinal period was assumed to be 120 ms, while for TRSE EPI DTI a 14 ms echo delay from the end of diffusion encoding was used to accommodate for the partial Fourier acquisition. Standard gradient hardware parameters were assumed: maximum gradient strength= 50 mT/m, maximum slew rate= 200 T/m/s

The considerable shortening of echo time not only preserve more signal from the short T_2 myelin water but also increases the sensitivity of DTI to favorably offset the inherent 50% signal reduction of stimulated echo. For example, Figure 14 (B) shows the theoretical signal-to-noise-ratio in white matter tissue as a function of diffusion

sensitization evaluated using tissue relaxation times from literature (Stanisz et al., 2005) and the minimum achievable echo times for the TRSE EPI and stimulated echo spiral-out acquisitions previously calculated. Clearly, even for small b-values the reduction in echo time enabled by our sequence modifications provides better white matter sensitivity than the clinical standard.

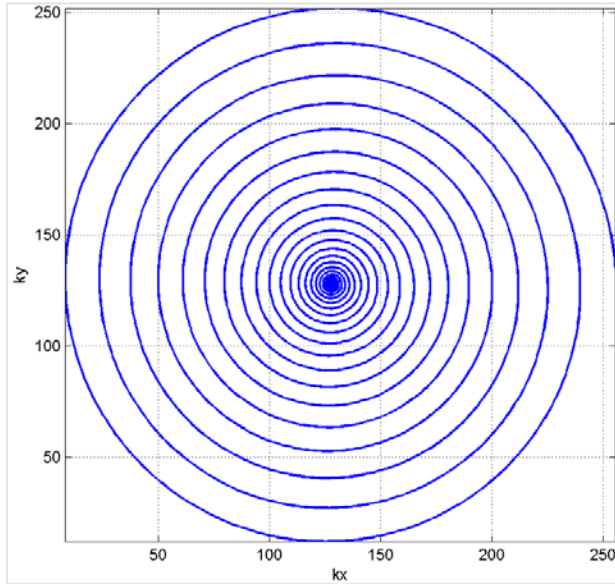
4.2 Inherent motion correction in high resolution DTI using self-navigated interleaved spiral (SNAILS) acquisition

The long readout duration required for single-shot acquisition in the conventionally DTI generally limits the imaging matrix (and hence in-plane spatial resolution) to moderate values (i.e. 128x128). To mitigate partial volume effects and better resolve crossing fibers in DTI it is often desired to use high spatial resolution. Most importantly however, intravoxel coherence of fiber orientations can significantly impact the measured average fractional anisotropy, especially for the myelin water weighted diffusion tensor which has small radial diffusivity. To achieve high resolution, the image must be acquired over multiple RF excitations (multi-shot) by segmenting the k-space coverage.

For in vivo diffusion imaging however, the large gradient amplitudes required for motion sensitization lead to random image phase errors in each excitation due to bulk motion. After reconstruction of individual image segments, these inconsistent motion induced phase errors destructively interfere resulting in signal loss image

artifacts. To correct for such errors it is necessary to acquire additional data in the form of a navigator, a low resolution phase image (sampling the center of k-space and its vicinity) from which motion can be estimated for each shot. There are several strategies for acquiring such navigators for EPI but many of them compromise on the available time for diffusion sensitization (and echo time), are not inherent, or have poor sensitivity..

Spiral imaging, on the other hand, provides great versatility in designing multi-shot acquisition strategies for diffusion imaging. In particular, it is possible to modify the segmented spiral trajectory to oversample the center of k-space thus acquiring an inherent navigator for each excitation. The oversampled k-space region can then be used to reconstruct a low resolution but full field-of-view (FOV) phase image from which motion induced phase errors can be estimated. Figure 15 shows the k-space trajectory for the variable density spiral analytically designed by Kim et al. (Kim et al., 2003) in which the parameter α conveniently controls the amount of oversampling. It has been previously demonstrated that this technique can be readily incorporated with spin echo DTI to generate high resolution images with excellent SNR and great spatial accuracy (Liu et al., 2004b).



$$k(\tau) = \lambda \tau^\alpha e^{j2\pi m \tau}$$

$$\tau(t) = \begin{cases} \left[\frac{s_m \gamma}{\lambda \omega^2} \left(\frac{\alpha}{2} + 2 \right) t \right]^{\frac{1}{\alpha+1}}, & 0 \leq t \leq \min(T_{s2a}, T_{es}) \\ \left[\frac{g_m \gamma}{\lambda \omega} (\alpha + 1) t \right]^{\frac{1}{\alpha+1}}, & T_{s2a} \leq t \leq T_{es} \end{cases}$$

Figure 15: Analytical design of a self-navigated spiral trajectory (Kim et al.). α is a parameter for controlling the change in density, n the number of turns, $\lambda = N/(2 \cdot FOV)$, s_m is the maximum slew rate, g_m the maximum gradient amplitude; T_{s2a} the transition time from slew rate limited to amplitude limited region, and T_{es} is the time to end of slew rate limited trajectory. The trajectory is rotated by an angle $\theta = 2\pi/N_L$ in order to acquire N_L interleaves.

While the self-navigated interleaved spirals DTI implementation (Liu et al., 2004b) provides inherent correction for shot-to-shot motion induced errors, the long readout duration of variable density spiral trajectories allows for phase accumulation due to off-resonance effects induced by field inhomogeneities. The reconstructed images can be severely degraded by artifacts of local blurring, stretching and compressing. To prevent these effects, the readout duration is generally reduced by increasing the number of interleaves (k-space segments). This strategy however, comes at the cost of significantly longer scan duration and can be impractical for clinical applications..

4.3 Magnetic field inhomogeneities and gradient eddy currents degrade DTI images

Diffusion tensor imaging (DTI) has the unique ability to non-invasively characterize the ordered microstructures of biological tissue such as white matter or myocardium (Basser et al., 1994a). The conventional DTI experiment requires the acquisition of one non-diffusion weighted baseline image and several images with diffusion-weighting gradients sensitized along at least 6 non-collinear orientations (Basser and Pierpaoli, 1998). These images are fit with a rank-2 tensor model and the underlying tissue microanatomy is assessed quantitatively with metrics such as fractional anisotropy (FA), mean diffusivity (MD), or principal diffusion direction. By assessing the main diffusion directions in the white matter, neural pathways across remote brain regions can be inferred to visualize and quantify the underlying structural connectivity (Mori et al., 1999, Hagmann et al., 2003). The tensor calculation is performed on a voxel-by-voxel basis and assumes images across all diffusion-weighting orientations are perfectly registered with minimal distortions.

However, many off-resonance effects - caused by tissue susceptibilities, gradient eddy currents, B_0 field variations, chemical shift, patient/physiological motion and/or hardware instabilities - can lead to imperfections in the desired k-space trajectories, thereby significantly degrading the reconstructed MR images. For DTI sequences specifically, the large-amplitude diffusion waveforms induce eddy currents in the gradient coils, which in turn generate diffusion-weighting direction dependent magnetic

field gradients during the readout window. As a result, each DW image is distorted differently depending on the orientation of the applied diffusion gradients. During advanced DTI scans which require long scan durations (Tuch et al., 2002, Liu et al., 2004b, Assaf and Basser, 2005, Wedeen et al., 2005, Avram et al., 2010c) the underlying magnetic field inhomogeneities might exhibit additional intra-scan variations due to patient motion (i.e. rotation of tissue susceptibilities with respect to the direction of the main field), physiological motion (i.e. breathing, pulsation of ventricles) or hardware instabilities. For spiral readout trajectories such spatially and temporally varying off-resonance effects lead to k-space trajectory imperfections which manifest as local image blurring, stretching and compressing. These distortions cause misalignments of DW images acquired with different diffusion orientations ultimately leading to erroneous tensor estimations and loss of spatial accuracy. In order to robustly estimate diffusion tensors on a voxel-by-voxel basis it is thus necessary to correct for off-resonance effects dynamically throughout the DTI scan.

A number of approaches have been proposed to address off-resonance distortions due to sequence-dependent eddy current (Haselgrove and Moore, 1996, Jezzard et al., 1998, Andersson et al., 2003, Bodammer et al., 2004, Shen et al., 2004) and sequence-independent susceptibility induced distortions in DTI. The sequence-dependent off-resonance effects due to eddy currents induced by the diffusion gradients can be partially mitigated using a twice refocused spin echo technique (Feinberg et al.,

1994, Reese et al., 2003a). However, this implementation generally restricts the maximally achievable b-value, requires longer echo time (thus leading to decreased SNR) and/or scan duration, and does not correct for off-resonance effects induced by other sources of magnetic field inhomogeneities such as tissue susceptibilities or B_0 field variations. An additional field-map based correction is commonly used to complement the distortion correction.

Most frequently, the field map can be estimated from a separate acquisition of two gradient echo images with different echo times. When this is done as a separate scan, the total scan duration is increased and the resultant field-map does not account for intra-scan variations of tissue susceptibility induced field inhomogeneities. To correct for such variations, a field map can be estimated dynamically using navigator data. While this method has been successfully implemented in functional MRI scans (e.g. using a spiral in trajectories), for spin echo DTI it is rather impractical, since the acquisition of an additional navigator would significantly reduce the available time for diffusion encoding.

A few studies propose a general approach to correct for both eddy current- or tissue susceptibility- induced off-resonance effects simultaneously, but require additional calibration scans (Chen et al., 2006, Truong et al., 2008) and/or scanner hardware (Barnett et al., 2009). A very common and successful method to dynamically mitigate the effects of field inhomogeneities due to various sources is to reduce the readout duration

by segmenting the acquisition, usually at the expense of increased scan time. However, for multi-shot diffusion imaging, it is generally necessary to acquire additional navigator data in order to correct for motion induced random phase variations in each shot (Miller and Pauly, 2003). This requirement further increases the duration of the readout and/or the overall scan duration.

We propose an integrated solution for dynamic and inherent off-resonance correction in DTI using a stimulated echo (STE) implementation with self-navigated interleaved spirals (SNAILS) readout. When compared to a clinical spin echo DTI sequence, the inherent half signal reduction associated with the stimulated echo pathway can be advantageously offset by a drastically shorter echo time (TE) for the same diffusion weighting. The spiral out readout further minimizes the achievable echo time providing excellent signal-to-noise ratio (SNR) especially for tissues with short T_2 relaxation times such as white matter, or myelin water. More importantly however, with the stimulated echo sequence it is possible to exploit additional spin echo coherence pathways and acquire a field map dynamically and inherently. In our implementation we preserve the spin echo signal formed by the first two 90° RF pulses and consecutively acquire two images with different echo times from which we can readily derive a field map. Because the diffusion weighted stimulated echo pathway is in the longitudinal plane during this period, it is not affected by our sequence modifications. The advantage of this approach is that all acquired field maps can be dynamic, inherent (created by the

same excitation pulse), high resolution and fully registered with the corresponding DWI image. Compared to the clinical TRSE EPI DTI sequence, even for small b-values, the current method has similar theoretical SNR in white matter, inherently corrects for distortions due to dynamic field inhomogeneities including eddy currents, and has the potential to image with large matrix size, large b-value, variable diffusion time and/or short TE. Compared to the current implementation of spin echo DTI with SNAILS acquisition, our new approach significantly reduces the total scan duration (by allowing longer readouts and thus fewer interleaves), achieves dynamic and inherent off-resonance correction, and a wider range of b-values, diffusion times, or echo times.

Taken together, our integrated techniques will be able to improve the spatial accuracy of DTI in an inherent and dynamic manner while achieving large b values and preserving a short TE. It is hoped that this new methodology will find increased utility in modern DTI applications where spatial accuracy and tissue specificity (e.g. myelin water with short T_2) are desired.

4.4 Integrated solution for short-TE DTI using Stimulated Echo SNAILS DTI with dynamic and inherent correction for motion and field inhomogeneities

A multi-slice STEAM DTI sequence with self-navigated interleaved spiral (SNAILS) readout was implemented on a 3T GE MR750 scanner (Fig. 16). Following a non-spatially selective fat suppression module, transverse magnetization is generated with a slice selective 90° sinc-shaped radio-frequency (RF) pulse. After diffusion

encoding, a second slice-selective 90° RF pulse is applied at $TE/2$ after excitation creating two coherence pathways: the main stimulated echo pathway used to acquire the desired diffusion weighted signal and a secondary, spin echo pathway, used for dynamic field map acquisition.

After the application of the second 90° pulse, the phase of the main diffusion-prepared stimulated echo pathway is stored in the longitudinal plane as M_z magnetization. The duration of this longitudinal period (T_M) in a STEAM experiment is generally limited only by the tissue T_1 relaxation rate and can therefore be relatively long ($T_M > 100\text{ms}$). To generate a stimulated echo the third slice-selective 90° pulse is played out at $TE/2+T_M$, followed by the corresponding balancing diffusion gradients and SNAILS center-out trajectory that minimizes the echo time. For each shot in the segmented DTI experiment, the variable density trajectory oversamples the center of k -space to acquire a low resolution, but full FOV image which serves as an inherent navigator to correct for motion induced random phase errors, as shown previously using spin echo (Miller and Pauly, 2003, Liu et al., 2004b). Using this acquisition scheme it is possible to acquire high resolution DTI images with excellent SNR (Liu et al., 2004b).

The signal amplitude of a stimulated echo is half of that measured using a spin echo with the same TE and b-value. However, because our STEAM spiral DTI implementation achieves considerably shorter TE for the same b-value, the signal amplitude of the measured stimulated echo can be comparable to that of the clinical

twice refocused spin echo sequence with partial Fourier EPI readout and parallel imaging, especially in tissues with short T_2 such as white matter (Fig. 14). In addition to the short TE the arbitrarily large b-value and diffusion time offers additional flexibility in designing advanced DTI experiments (Tuch et al., 2002, Liu et al., 2004b, Assaf and Basser, 2005, Wedeen et al., 2005, Avram et al., 2010c), while the segmented acquisition provides the possibility for high resolution imaging (Liu et al., 2004b, Holdsworth et al., 2008). Nonetheless, our technique still suffers from the common eddy current artifacts induced by large diffusion gradients preceding the spiral readout. To address this problem and other off-resonance effects, we propose to take advantage of a secondary spin echo coherence pathway to acquire additional images and generate magnetic field maps in an inherent manner.

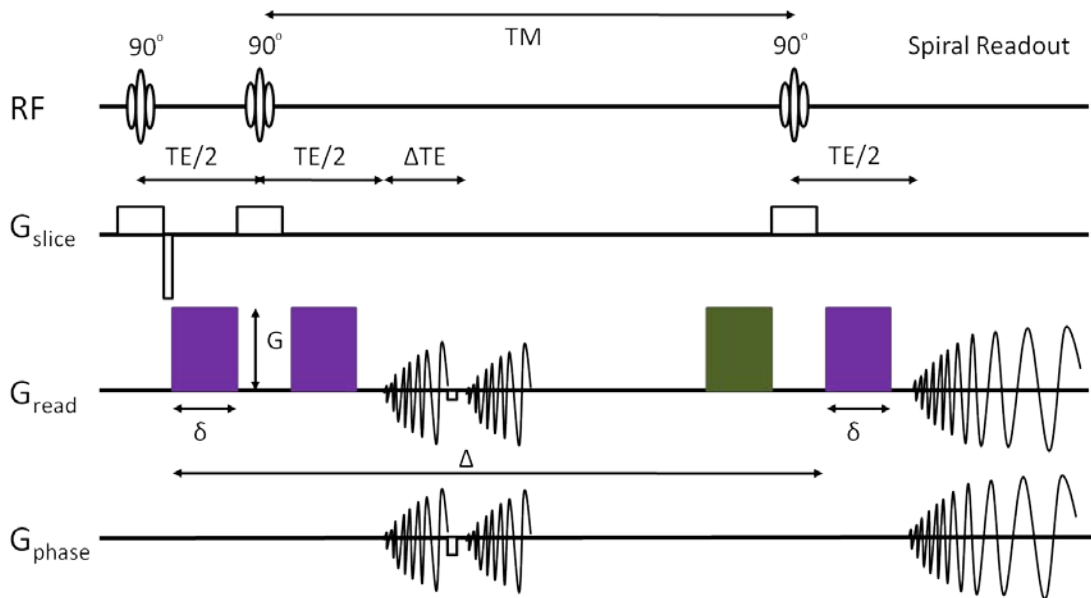


Figure 16: STEAM DTI pulse sequence with inherent and dynamic field-map acquisition. Non-spatially selective fat suppression module (blue) precedes slice excitation. Diffusion weighting gradients (purple)

cause identical eddy current during the SE and STE readouts. Crusher gradients (green) also act to replicate the same eddy current profile for both STE and SE readouts.

Specifically, the spin echo formed by the first two 90° RF pulses can be refocused with balancing diffusion gradients and acquired at a minimized echo time $TE_1=TE$ using a segmented readout with spiral-out trajectory. During this period (TM) the main stimulated echo pathway stored in the longitudinal plane remains unaffected by any gradient manipulations. The amplitude of the acquired spin echo signal is only 50% of the amplitude of a conventional spin echo (using a 180° refocusing pulse) with the same TE and b-value. However, because the diffusion pulse durations used in a stimulated echo experiment are generally short, the diffusion weighting on this spin echo pathway can be small (generally on the order of 50 s/mm^2) providing sufficient signal for the acquisition of a second, asymmetric spin echo at later time $TE_2= TE_1+\Delta TE$, (with ΔTE of phase evolution under the effect of field inhomogeneities) following a quick rephasing of the first readout trajectory. A dynamic field map can then be reliably calculated from the complex subtraction of these two phase images. Generally the minimum interval ΔTE provides the best SNR, but is restricted by the duration of the first readout and its rephasing gradient. In order to increase the robustness of the field map estimation, the ΔTE can be reduced using a segmented uniform density spiral trajectory to acquire the two echoes. Because the field map is computed using complex division (phase subtraction), random shot-to-shot phase variation due to motion during the interval TE will be inherently removed during the segmented acquisition of the two phase images.

Finally, to ensure that the eddy currents induced in the gradient coils preceding the spin echo and stimulated echo readouts are identical, the diffusion gradients need to be replicated (at the end of the TM interval) to the left of the last 90° RF pulse. These matching diffusion gradients conveniently serve an additional purpose as crusher gradients to remove any residual magnetization from undesired pathways.

Overall, preserving the spin echo pathway during the longitudinal period (TI) gives us the opportunity to acquire a high fidelity field map (inherent, good SNR, high spatial resolution, little distortions) dynamically without any penalty. This field map can then be used to inherently correct for off-resonance effects due to both eddy currents and intra-scan magnetic field inhomogeneities variations that change on a temporal scale larger than the image readout window.

4.5 Image reconstruction using simultaneous motion and off-resonance correction

The newly developed sequence was used to conduct DTI scans in healthy volunteers who provided informed written consent in compliance with the Institutional Review Board protocol at Duke University Medical Center. A set of DTI images were obtained with a matrix size of 192x192x5 over a 24x24 cm² FOV with 5 mm slice thickness, TE/TM/TR = 22/120/4000 ms, b-value of 1000 s/mm² and 15 diffusion directions. For each image, 10 k-space segments were acquired using a variable density spiral readout trajectory of 29 ms duration with inherent self-navigation capability. For

both spin echo acquisitions a segmented spiral was used to acquire images at $TE_1/TE_2=22/28\text{ms}$ (10 interleaves with 5 ms readout duration). The b value on the spin echo pathway was 55 s/mm^2 . Because the two spin echo images were acquired consecutively along the same coherence pathway, motion induced random phase terms in each shot are removed after complex subtraction of the phase images. The inherent field map was calculated robustly from the total phase accumulated during the ΔTE duration.

To correct the effects of k-space trajectory imperfections in the measured diffusion weighted images based on the corresponding field maps, both time and frequency domain off-resonance correction methods were implemented: simulated phase evolution rewinding (SPHERE) (Kadah and Hu, 1997), and direct conjugate phase reconstruction (Noll et al., 1992), respectively. For the SPHERE reconstruction, an initial image estimate was reconstructed from the raw data using phase correction to remove the shot-to-shot phase variation due to motion. A corrected raw dataset was then obtained after rewinding the phase of the measured data in individual $200\mu\text{s}$ time segments based on the acquired field map. The final images were obtained after gridding and Fourier Transformation of the corrected raw data for all k-space segments. For conjugate phase reconstruction (Liu et al., 2005a), each stimulated echo diffusion weighted image was reconstructed with phase correction following raw signal demodulation at different frequencies (increments of 5Hz) within the range of observed

field-map off-resonances (-50 to 50Hz). The series of reconstructed images was multiplied by a binary frequency mask prior to summation.

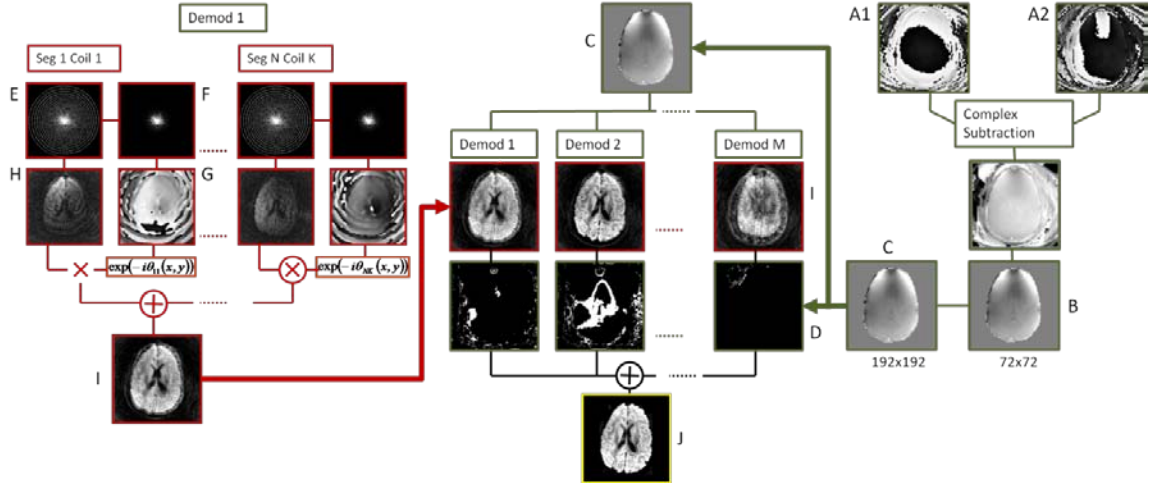


Figure 17: Simultaneous inherent motion and off-resonance correction image reconstruction pipeline. Phase images reconstructed from the symmetric (A1) and asymmetric spin echo (A2) acquisitions are subtracted to obtain a field map (B) which is interpolated (C) and segmented into different bins (D) corresponding to small frequency ranges (~3Hz). The individual readouts acquired on the stimulated echo diffusion weighted pathways are demodulated at each mean bin frequency and gridded on to a 2x oversampled Cartesian grid (E). The inherent oversampled navigator data (F) is used to reconstruct a low resolution full FOV image (G) which is removed from the corresponding interleaf (H) prior to summation. The motion corrected images reconstructed at each demodulation frequency (I) are multiplied by their corresponding frequency masks (D). Following summation across all frequency bins, the motion and off-resonance corrected image (J) is obtained.

The images obtained with our new sequence before and after correction were compared to those obtained with the clinical DSE EPI DTI sequence. To illustrate the effect of dynamic off-resonance correction diffusion tensors were fit to the data acquired with our new method before and after correction. Fractional anisotropy, axial and radial diffusivity and main diffusion orientation were quantitatively and qualitatively compared in white matter regions with highly varying degrees of field inhomogeneities.

4.6 Short-TE DTI with high spatial resolution and accuracy

In DTI the echo time is limited by the transverse duration of diffusion preparation which can be significantly shortened with stimulated echo, thus reducing the echo time and offsetting the inherent 50% signal deficit. The echo time can then be further reduced by using a spiral out readout trajectory. For a given b-value, the minimum echo time achieved with a STEAM spiral-out DTI sequence ($T_M=120\text{ms}$) is significantly shorter than that obtained with the clinical TRSE EPI DTI sequence with partial Fourier encoding (Stanisz et al., 2005) (and SENSE acceleration). Based on the T_1 and T_2 white matter relaxation parameters at 3T (Stanisz et al., 2005) the theoretical white matter SNR for the two sequences was compared as a function of b-value (Fig. 14: B): it is evident that even for modest b-values ($\sim 600\text{ s/mm}^2$) the stimulated echo diffusion weighted signal amplitude is comparable to that obtained with the clinical sequence.

The inherent field maps acquired dynamically for each diffusion direction (Fig 18: A-D) show clear distinctions depending on the orientation of the applied diffusion weighting gradients. A rough estimate of the eddy current maps for each diffusion weighting direction, including intra-scan variations of other sources of field inhomogeneities, can be obtained by subtracting the field map corresponding to the baseline image from those corresponding to the diffusion weighted images (Fig 18: E-H). This operation reveals the relative contribution of gradient eddy current induced off-resonance fields (local variations up to 40 Hz), but is not necessary for image correction.

Instead, it is more practical to use the field maps measured dynamically for each diffusion orientation, since they inherently include both gradient eddy current effects and intra-scan variations of magnetic field inhomogeneities.

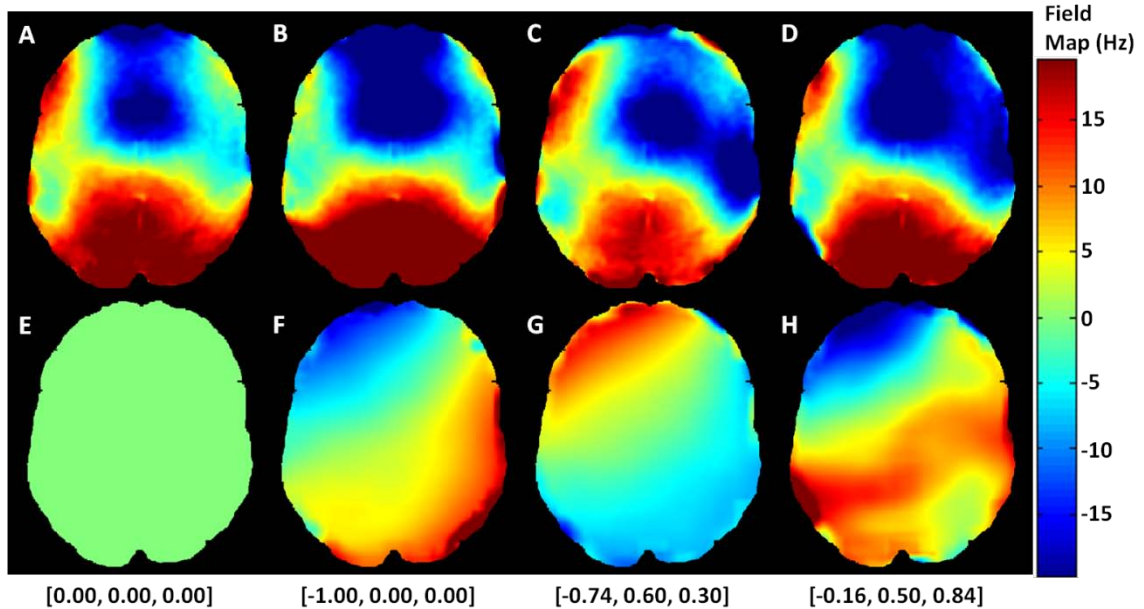


Figure 18: Top row: field maps acquired dynamically for the baseline image (A) and three diffusion weighted images (B-D) acquired with different orientations. Bottom row: Corresponding eddy current profile estimations (E-H) calculated by subtracting the field map (A) corresponding to the baseline image from corresponding to the diffusion weighted images (B-D).

The diffusion weighted images were first reconstructed by removing the motion induced phase errors in each interleave using the inherent navigator data (Fig. 19: A-C). As expected, even for long diffusion times, the random phase is successfully removed to yield high resolution diffusion weighted images with excellent signal intensity (no signal loss artifacts commonly associated with multi-shot diffusion imaging). However, a visual inspection in regions of large eddy current fields reveals significant blurring and stretching, depending on the orientation of the diffusion weighting gradients (Fig. 19:

arrows). In particular, grey matter signal from sulci and gyri is distributed to the neighboring voxels leading to erroneous measurements in adjacent white matter tracts. The full extent of these distortions can be appreciated by comparing the images before and after off-resonance correction with inherent field maps. As shown in Fig. 19 (D-F), both baseline and individual diffusion weighted images are inherently corrected, as compared to the uncorrected images (Fig. 19: D-F). Various local blurring artifacts (arrows) are specifically removed (arrows), leading to greatly improved spatial accuracy in each diffusion weighted image.

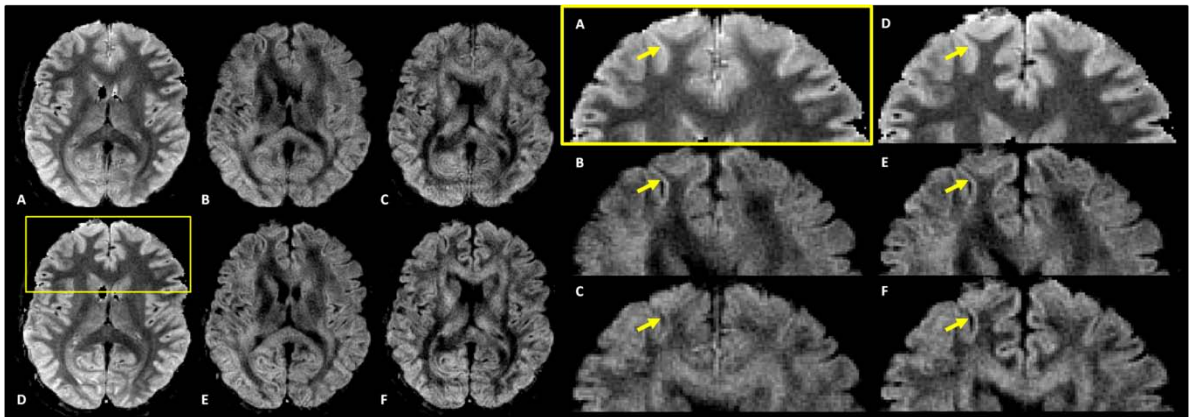


Figure 19: Top row: Baseline (A) and diffusion weighted images (B, C) acquired with STEAM SNAILS DTI and reconstructed with motion correction. Bottom row: The same images (D, E, and F respectively) after simultaneous motion and off-resonance correction with inherently acquired field maps. Local blurring artifacts (yellow arrows) are specifically corrected for each image individually to remove diffusion weighting direction dependent distortions caused by eddy currents.

Finally, rank-2 diffusion tensors were fit to the STEAM DTI dataset and the principal diffusion direction-colored FA maps were computed and compared before and after off-resonance correction (Fig. 20). As expected, due to direction dependent image blurring, the uncorrected images have vaguely delineated white matter features and

small FA values in the WM fibers affected by field inhomogeneities, especially eddy currents. After correction these images are greatly improved: the FA is restored, and small fibers in the posterior and anterior regions become considerably more discernible.

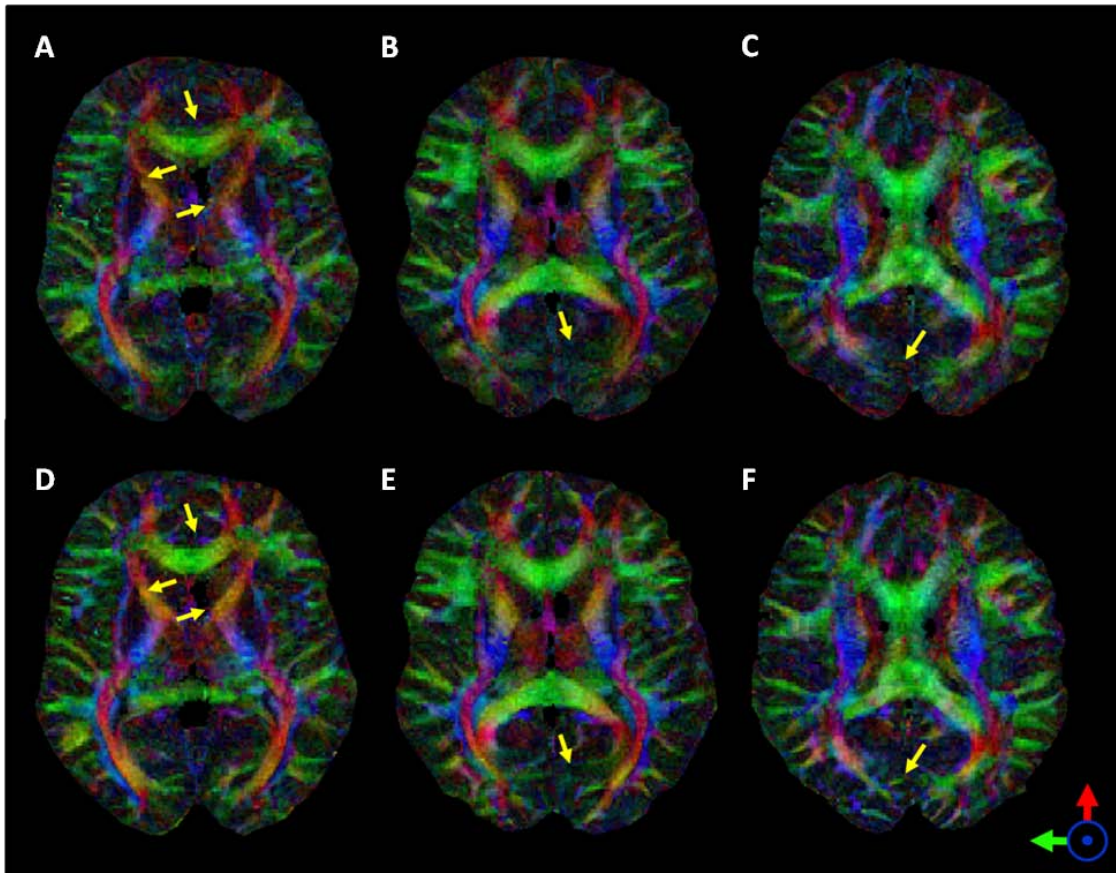


Figure 20: Fractional Anisotropy (FA) maps with principal diffusion orientation color-coding for three slices. Top row: images reconstructed with motion correction only (A, B, C). Bottom row: images reconstructed with simultaneous motion and off-resonance correction (D, E, F).

Many methods have been proposed to address image distortions due to eddy current- and tissue susceptibility -induced field inhomogeneities during a DTI scan. Most of these methods come at a cost of separate calibration scans or additional hardware, often require registration of separately acquired field-maps with the uncorrected images and significantly limit the range of feasible diffusion parameters

such as b-value, TE or diffusion time. Our newly developed methodology has demonstrated for the first time that it is possible, using a stimulated echo, to correct for off-resonance effects in DTI inherently and dynamically.

Compared to the twice refocused spin echo EPI DTI, for the same spatial coverage and b-value, our current method requires a slightly longer repetition time (TR) due to the increased diffusion time. Theoretically, the stimulated echo spiral DTI implementation results in a 20% longer slice acquisition duration when compared to the TRSE DTI with EPI readout. In practice however, the realistic increase in scan time is smaller, since the throughput of TRSE DTI is often limited by hardware considerations such as gradient duty cycle and heating, especially for long DTI scans (high res, or advanced). This throughput limitation in our technique can be addressed using a 3D multi-slab acquisition strategy (Frank et al., 2010) which could significantly reduce the TR without overdriving the gradient hardware system.

Despite the slight throughput disadvantage, our current implementation represents an integrated solution for high-resolution DTI with inherent motion and off-resonance correction capabilities and optimal flexibility for diffusion scan parameters.

It has been previously demonstrated that it is possible to acquire spin echo DTI images with high spatial resolution and excellent SNR, using SNAILS readout (Liu et al., 2004b). In this manuscript, we have extended this methodology to a stimulated echo to achieve significantly shorter echo times and have demonstrated that even in the

presence of longer diffusion times the inherent navigator data can be used to reliably remove motion induced phase errors in each shot (Fig. 19, top row). We then further adapted the STEAM SNAILS DTI implementation with a complementary methodology to address distortions introduced by off-resonance effects during the relatively long self-navigated spiral readout.

The dynamic acquisition of the inherent field map can be designed independently from that of the diffusion weighted images, using high spatial resolution or temporal resolutions. If single-shot readout trajectories are used for acquiring the two spin echo images, a low resolution field map can be estimated for every shot. The resulting correction (using time-domain based phase-rewinding methods) would account for eddy current transients and real-time intra-scan variations. For multi-shot field map acquisition, because of the short readout durations, it is possible to concatenate more than two acquisitions to better characterize the spatial and temporal of transient eddy currents. Finally, the use of parallel imaging offers additional flexibility in designing the field map acquisition and significantly reduces the overall scan time (Liu et al., 2005b).

4.7 Short-TE DTI as a new clinical tool for analyzing diffusion anisotropy of T_2 components of white matter

Compared to the clinical TRSE DTI with EPI readout, our current technique achieves significantly shorter echo times, large b-values, and improved SNR. Being able

to explore the outer reaches of both k-space and q-space without the use of custom insert gradient hardware (Feldman et al., 2011), it could provide new tissue specific information and promote the adoption of advanced DTI methods to everyday clinical practice (Tuch et al., 2002, Wedeen et al., 2005, Assaf et al., 2008, Liu et al., 2010). More importantly, the exclusive use of short echo times for in vivo DTI preserves signal from short T₂ myelin water, which could reveal unique information about myelin microstructural changes during early development or pathology.

In summary, compared to previous approaches, our integrated solution has the potential to obtain DTI images with the great spatial accuracy (distortion free) and high spatial resolution required for applications such as full brain DTI connectivity studies (Skudlarski et al., 2008). Moreover, it can achieve very large b-values which opens new avenues for the clinical implementation of advanced DTI methods (Tuch et al., 2002, Wedeen et al., 2005, Assaf et al., 2008, Liu et al., 2010) and is uniquely suited for myelin-specific DTI applications that require short echo time (Avram et al., 2010c).

Chapter 5: Characterizing the TE dependence of white matter diffusion anisotropy in vivo

Our newly developed integrated DTI technique can acquire artifact-free high-resolution images with TEs as short as 18ms and thus has the potential to characterize white matter diffusion anisotropy as a function of echo time (Avram et al., 2011b). A better understanding of this relationship will guide the design of an efficient and practical imaging protocol for achieving sufficient myelin sensitivity in DTI within scan durations suitable for clinical applications. To this purpose we modify the sequence to accommodate the acquisition of multiple echo times and conduct an unprecedented multi-TE experiment in vivo with a wide range of short TE's (Avram et al., 2011a). Moreover, with a sufficiently large number of TEs it is possible to conduct a multi-exponential T_2 /diffusion decay analysis on the multi-TE DTI dataset and quantify the diffusion anisotropy of individual T_2 components in human white matter: myelin water (short T_2 peak), axonal/intercellular water (intermediate T_2 peak) or cerebrospinal fluid (long T_2 peak). Unlike most advanced DTI methods that interrogate diffusional properties along numerous diffusion weighting directions or b-values, our study explores a new dimension (T_2 relaxation time) that is inherently more tissue specific. In particular, characterizing diffusional properties of short T_2 white matter components (myelin water) could have an immediate clinical impact on our understanding of myelin

microstructural changes during pathological evolution of neurological disorders of white matter origin or in healthy brain maturation.

5.1 Myelin water diffusion in animal specimen and the need for in vivo human WM studies

Over the last decade, DTI studies using myelin deficient mouse models have suggested accruing evidence that myelin changes might be related to observed changes in anisotropy metrics such as FA or radial diffusivity. Investigations using the Shiverer mouse model measured a smaller radial diffusivity, but similar axial diffusivity in the anesthetized myelin-deficient compared to control mice (Song et al., 2002, Song et al., 2003), while a comparable study using DTI measurements with large b-values estimated the displacement probability distributions in the two mice populations found that dysmyelination does not significantly impact diffusion anisotropy characteristics (Biton et al., 2006). While these studies concur that the myelin microstructure plays a critical role in determining the measured diffusional properties in white matter, the incongruities in their findings suggests that conventional DTI cannot consistently dissociate changes in myelin microstructure, but rather is reflects only secondary effects of dysmyelination. To achieve direct sensitization to myelin microstructure it is necessary to integrate DTI with a myelin water selection technique.

The dependence of diffusion anisotropy on the T_2 components of myelinated nerves has been previously investigated in a few diffusion spectroscopy studies (Basser

et al., 1994b) of excised animal specimen - bovine optic nerve (Stanisz and Henkelman, 1998) and frog sciatic nerve (Peled et al., 1999, Andrews et al., 2006b) - using a modified CPMG sequence with diffusion sensitization (van Dusschoten et al., 1996) to acquire the diffusion weighted signal at multiple echo times. The recent study by Andrews et al found strong evidence that compared to other white matter T_2 components myelin water has larger diffusion anisotropy mainly due to smaller radial diffusivity. While animal studies can provide good sensitivity (imaging is not required) and the possibility to follow-up with histological correlations, the results of such investigations might be influenced/corrupted by factors such as sample type (PNS vs CNS) (Trapp and Kidd, 2004), sample preparation and handling (diffusional and T_2 characteristics can be affected by tissue autolysis post mortem) (Hukkanen and Roytta, 1987), or scan parameters (long CPMG echo train length can lead to accumulation of MT effects). Even with in vivo conditions, anesthetized animal studies are highly impractical because of their low sensitivity (high resolution needed to resolve white matter structure) as well as motion induced imaging artifacts that lead to signal instabilities during the multi-echo DTI acquisitions. Most importantly however, animal and human white matter have slightly dissimilar neuroanatomical microstructure (e.g. axon diameters, axonal density, sheath thickness, interlamellar distance, internode separation) that follow distinct pathological and developmental timelines (Yankelov and Lecours, 1967, Hamano et al., 1998).

Instead, characterizing the diffusion anisotropy of myelin water directly in human subjects will have an immediate clinical impact by enabling longitudinal studies of myelin microanatomical changes during white matter maturation, demyelination and myelin repair. The scarcity of human specimen and the lack of clinical tools for non-invasively investigating myelin structural changes call for the construction of a myelin specific diffusion tensor. Because the long echo times of conventional DTI implementations preserve little signal from myelin water, even advanced diffusion models that sample white matter with large b-values and numerous diffusion weighting orientations have limited tissue specificity, usually inferred indirectly. Moreover, since the diffusion tensor of MW has the same principal diffusion directions as that of other proton pools in white matter (e.g. axonal water), quantitative assessment of a myelin specific diffusion tensor requires a new dimension of analysis that can specifically select short T₂ white matter components. To better understand the diffusion anisotropy of short T₂ components we can use our technique developed in the previous chapter to analyze DTI changes in the short TE regime that is not achievable with conventional DTI.

5.2 Cardiac Gated multi-TE DTI pulse sequence with a wide range of short TEs

At the end, we adapted the short-TE DTI methodology developed in the previous chapter to acquire images at multiple echo times within a single DTI scan.

Using the stimulated echo mechanism with a spiral-out readout trajectory the echo time is significantly minimized compared to conventional DTI methods. With these modifications it is possible to achieve echo times as short as 18 ms for a $b=600 \text{ s/mm}^2$. To avoid signal instabilities in a CPMG echo train associated with repetitive refocusing of a motion sensitized diffusion weighted coherence pathway, we acquired each echo separately. Moreover, we used a single-shot uniform density spiral readout trajectory in order to accommodate the maximum number of echo times within a reasonable scan duration and mitigate potential registration errors between images due to intra-scan patient motion. For every diffusion encoding direction, images at different echo times were acquired sequentially using the same diffusion encoding scheme (same diffusion parameters) and identical duration of longitudinal relaxation (Fig. 21). Finally, to preclude signal variations due to inconsistencies between excitation and refocusing slice profiles, the sequence was triggered using cardiac gating.

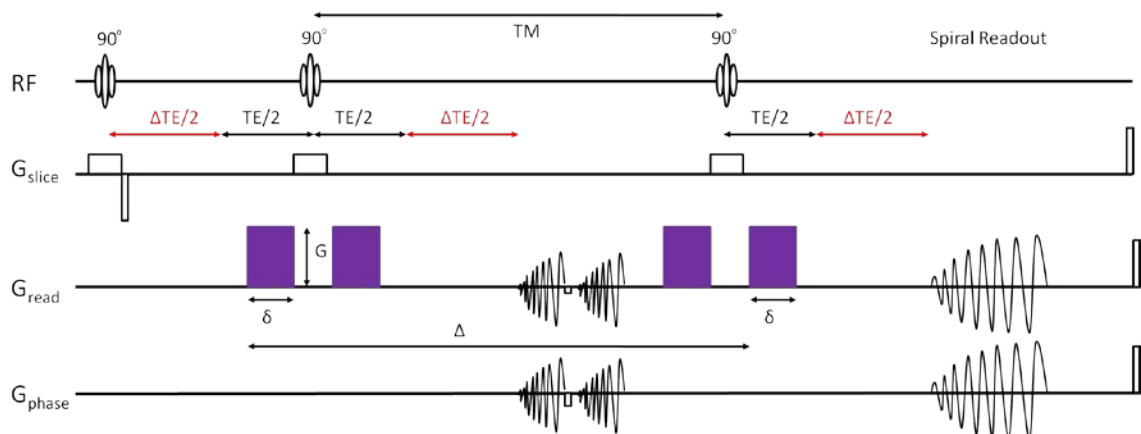


Figure 21: Schematic representing the pulse sequence diagram for the cardiac gated multi-TE sequence, using a uniform density spiral readout trajectory to acquire images in a single shot. For every TR, by increasing the intervals $\Delta TE/2$ (marked red) the effective echo time is incremented without changing the

diffusion sensitization (same diffusion encoding parameters Δ , δ , and G) or the duration of longitudinal relaxation (TM interval). To ensure consistent voxel composition, looping over echo times was nested inside the loop across different diffusion encoding directions.

The newly developed cardiac-gated multi-TE DTI pulse sequence was used to scan a healthy human volunteer who provided informed written consent in compliance with the Institutional Review Board protocol at Duke University Medical Center. Single-shot diffusion weighted images were acquired with a 22x22 cm² field of view (FOV) on a 96x96 image matrix (39ms readout duration) over 6 slices with a slice thickness of 5mm. Along the secondary spin echo pathway, two consecutive echoes were acquired for field map estimation (with a 46x46 matrix) using single-shot uniform density spiral-out readout trajectories of 14ms duration. The echo time was varied from TE=22ms to 92ms in 10ms increments. The diffusion weighting factor was 800 s/mm² along 15 non-collinear diffusion orientations. To allow full signal recovery in our multi-slice acquisition, the repetition time of the sequence was set to 7 times the R-to-R peak interval of the cardiac cycle. Throughout the entire scan duration (~25 minutes), no arrhythmia was observed; the heart rate of the subject was consistent and did not exceed 65 beats-per-minute.

5.3 In vivo multi-TE DTI reveals changes in anisotropy at short echo times

Artifact free images with excellent spatial accuracy and great SNR were reconstructed using the dynamic and inherent field-map based off-resonance correction

method described in the previous chapter. Periventricular white matter regions exhibited little signal variation suggesting that physiological motion (i.e. pulsation in the ventricles) was successfully mitigated using cardiac gating. The conspicuous contrast variation and large dynamic range across echo times suggests that the images acquired with short echo times might contain information that is not available with conventional DTI methods using echo times of 70-100ms.

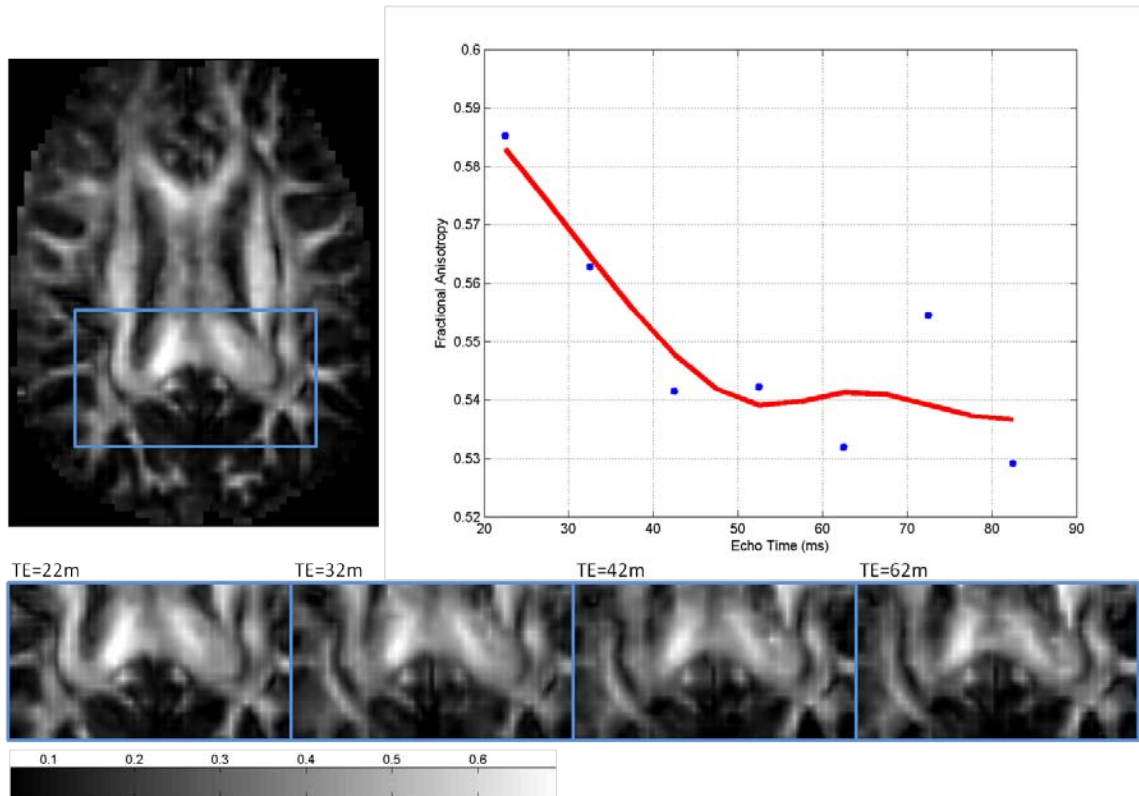


Figure 22: FA dependence on echo time. The abrupt decrease of FA in the short TE range from 22ms to 52ms, can be attributed to the diminishing contribution from short T_2 component. Assuming T_2 water components have the same preferred diffusion direction, the FA decreases in the short TE range implies that myelin water has larger anisotropy compared to other white matter T_2 components. At larger echo times, the FA appears to plateau and the measurements become more noisy due to decreasing SNR.

Each DTI dataset was then fitted with a rank-2 diffusion tensor model and the fractional anisotropy and diffusivities were quantitatively compared as a function of

echo time using an region-of-interest ROI based analysis. No significant difference was observed between the main diffusion orientation with echo time, suggesting that all T₂ water components (myelin water and axonal/intercellular water) diffuse preferably along the direction of the nerve fiber. The ROI analysis was focused mainly in the splenium of the corpus callosum and major white matter tracts to minimize partial volume effects with CSF within the 2.3x2.3x5 mm³ voxels. In Figure 22 the average fractional anisotropy across the ROI is plotted as a function of echo time. The initial decrease in FA (7.7%) as the TE varies from 22 to 52ms is followed by a plateau region (TE>=62ms) suggesting the that water with short T₂ (i.e. myelin water) contributes more to the anisotropy observed at short echo times than water with intermediate and long T₂ components. This initial decrease in anisotropy is unlikely caused by contributions from long or intermediate T₂ water (such as CSF or axonal/intercellular water respectively) which have similar signal contribution in images acquired with echo times of 22ms and 32ms, for example. For TEs above 60ms the FA reaches a plateau and the variability of our measurement increases, most likely due to decreased signal to noise ratio in the DTI images acquired at longer echo times.

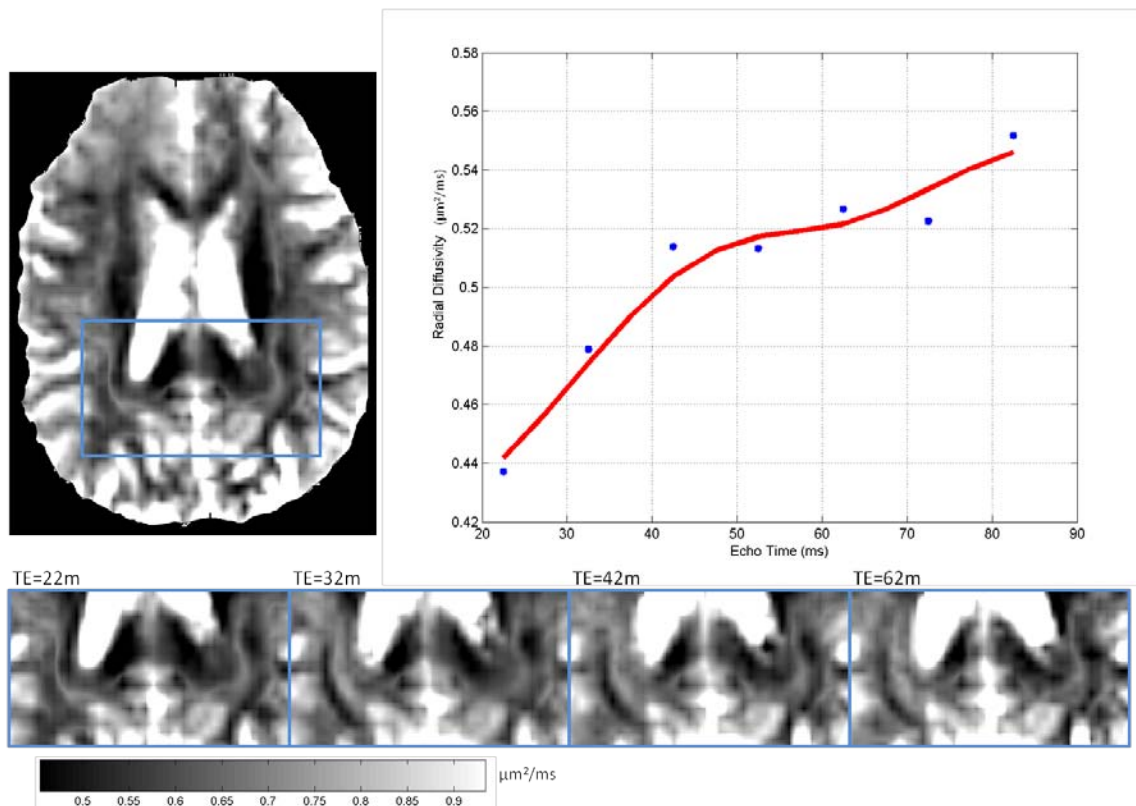


Figure 23: Dependence of radial diffusivity on echo time. The increase of radial diffusivity in the short TE range from 22ms to 52ms follows closely the decrease of FA observed in Fig. 22. For larger echo times the radial diffusivity increases slightly, probably due to decreasing SNR.

Comparing the echo time dependence of radial diffusivity, averaged over the same white matter ROI, we observe an initial increase of 18% (Fig. 23) that matches the decrease in FA (Fig. 22) in the short TE range from 22-52ms. At the longer echo times (62-82ms) the radial diffusivity increases slightly (6.5%), most probably due to reduced SNR. No significant change in the axial diffusivity was observed for echo times in the range 22-52ms. At longer echo times (>62ms) however, the axial diffusivity showed an increase, slightly less prominent than that of the radial diffusivity, which can also be attributed to low SNR.

5.4 Partial volume effects and the need for T_2 spectrum analysis

The methodology developed in the previous chapter allows us, for the first time, to probe white matter diffusion anisotropy in vivo in the regime of echo times between 22 and 52ms, where short T_2 myelin water signal contribution is considerable (Avram et al., 2011b). Our preliminary results obtained with a cardiac-gated multi-TE DTI sequence reveal a significant decrease in FA (7.7%) explained by an increase in radial diffusivity (18%) over this range of short echo times (22-52ms) which is consistent with the diminishing contribution of the short T_2 myelin water pool believed to have larger anisotropy due to smaller radial diffusivity (Avram et al., 2010b). For echo times greater than 62ms both radial and axial diffusivities were found to increase slightly resulting in a stabilization of the FA. At long echo times, however, measurements are less reliable and should be interpreted in the context of possibly insufficient SNR.

Another potential cause of variation in our observed echo time dependence is CSF contamination in periventricular white matter. Given the large voxel size $2.3 \times 2.3 \times 5 \text{mm}^3$ used in our experiment, partial volume effects cannot be entirely excluded. Nevertheless, due to its long T_2 relaxation time ($\sim 2 \text{sec}$), the signal contribution of CSF does not change considerably in the range of short TEs and consequently is unlikely a determinant factor of the observed changes in anisotropy. The same argument can be invoked to invalidate the contribution of axonal/extracellular water (with intermediate T_2) as the dominant source of observed anisotropy dependence. While the

current methodology does not represent a complete solution for characterizing myelin water anisotropy, understanding the echo time dependence of diffusion anisotropy can help us design practical solutions for achieving myelin water weighting in clinical applications.

A natural way to address partial volume effects is to increase the spatial resolution of the imaging protocol (Liu et al., 2004b). In our initial experiment in-plane voxel dimensions were large to allow for efficient single slice image acquisition while the slice thickness of 5mm was chosen to ensure sufficient SNR. The volume of data in a high-resolution in vivo multi-TE DTI experiment necessitate excessively long scan durations leading to discomfort to human volunteers and inevitable image mis-registration due to subject motion. Moreover, even a high resolution DTI study would not be able to efficiently separate tissue components based on their T_2 characteristics. Instead, a more reasonable solution to address partial volume effects is to conduct a T_2 spectrum decomposition and isolate the signal in individual water peaks.

A joint multi-exponential diffusion/relaxation decay analysis of white matter signal, however requires the acquisition of measurements at a larger number of echo times. Moreover, because both diffusion and T_2 relaxation result in exponential signal decreases these measurements lead to a badly conditioned and highly non-linear system of equations.

$$S_{i,j} = \sum_{k=1}^{\xi} \rho_k e^{-\frac{TE_j}{T_{2,k}}} e^{-\mathbf{b}:\mathbf{D}_k} \quad (5.1)$$

In the following section we will describe our development of a methodology to address the technical difficulties of multi-TE DTI analysis and robustly estimate the diffusion anisotropy of different T_2 components.

5.5 Robust T_2 spectrum analysis of diffusion tensor images

The diffusion coefficient in the Einstein equation (Equation 1.1) can be extended to a diffusion tensor. For a sufficiently large number of proton spins undergoing random walk, the ensemble average diffusion tensor can be written as:

$$\mathbf{D} = \frac{1}{2\tau} \langle \Delta \mathbf{r}^T \Delta \mathbf{r} \rangle = \frac{1}{2\tau} \frac{1}{N} \left(\sum_{j=1}^N \Delta \mathbf{r}_j^T \Delta \mathbf{r}_j \right) \quad (5.2)$$

where $\Delta \mathbf{r}_j$ is the (row) vector displacement of individual spins and τ is the diffusion time. If the entire ensemble of N protons consists of ξ subpopulations (pools) of sizes N_1, N_2, \dots, N_ξ with average diffusion properties $\mathbf{D}_1, \mathbf{D}_2, \dots, \mathbf{D}_K$ (e.g. myelin water, axonal water, CSF, etc.) we can re-write Equation 5.2 as a summation over individual subpopulations of spins:

$$\mathbf{D} = \frac{1}{2\tau} \frac{1}{N} \sum_{k=1}^{\xi} \left(\sum_{j=1}^{N_k} \Delta \mathbf{r}_j^T \Delta \mathbf{r}_j \right) = \frac{1}{2\tau} \frac{1}{N} \sum_{k=1}^{\xi} N_k \langle \Delta \mathbf{r}^T \Delta \mathbf{r} \rangle_k = \sum_{k=1}^{\xi} f_k \mathbf{D}_k \quad (5.3)$$

Where $f_k = N_k/N$ represents the population fractions of spins in each proton pool. Thus, the statistical nature of diffusion allows us to decompose the diffusion tensor

into a weighted summation of separate tensors corresponding to diffusion of different proton pools within the spin ensemble. This model assumes that within each population, transverse relaxation $T_{2,k}$ and diffusion \mathbf{D}_k characteristics are consistent, a condition justified by the validity of the central limit theorem given the large number of spins within a typical MRI voxel. Unlike other popular diffusion models (e.g. bi-exponential model) (Niendorf et al., 1996) our approach does not require compartmentalization and allows for free exchange between individual spin populations.

For a multi-TE DTI dataset acquired using η diffusion orientations at ζ echo times, individual diffusion weighted images $S_{i,j}$ (with $i = \overline{1,\eta}$ and $j = \overline{1,\zeta}$) can be related to the diffusion tensors of individual subpopulations $k = \overline{1,\xi}$ as follows:

$$-\ln\left(\frac{S_{i,j}}{S_{0,j}}\right) = b\mathbf{g}_i^T\left(\sum_{k=1}^{\xi}\frac{\rho_k e^{-\frac{TE_j}{T_{2,k}}}}{S_{0,j}}\mathbf{D}_k\right)\mathbf{g}_i = b\mathbf{g}_i^T\left(\sum_{k=1}^{\xi}f_k^j\mathbf{D}_k\right)\mathbf{g}_i \quad (5.4)$$

where, b is the diffusion sensitization factor, \mathbf{g}_i is a column vector denoting the orientation of the applied diffusion gradients $S_{0,j}$ are the baseline images acquired with echo time TE_j , while ρ_k and $T_{2,k}$ are the proton density and T_2 relaxation time constant of the k -th subpopulation. In the above expression we have introduced the notation f_k^j for the signal fraction of the component k measured at echo time $T_{2,k}$. In doing so, we have made the assumption that loss of coherence due to magnetic transverse relaxation and diffusion occur through independent physical mechanisms, and hence the signal fraction of each proton pool at a given echo time can be treated as an "apparent"

population fraction. This assumption is supported both by experimental results validating that local mobility (molecular tumbling causing T_2 decay) and spatial mobility (translation molecular motion causing diffusion decay) of water molecules occur through independent mechanisms (Knauss et al., 1996).

Our preliminary analysis of echo time dependence in DTI strongly suggests that diffusion anisotropy differs significantly across white matter T_2 spectrum, specifically short T_2 myelin water (<50ms) has larger anisotropy compared to intermediate T_2 (~80ms) axonal water or long T_2 CSF. More generally, we can use Equation 5.4 to characterize diffusion within ξ different T_2 components using rank-2 diffusion tensors. The multi-TE DTI experiment then can be understood as a collection of $(\eta + 1)\zeta$ measurements ($\eta\zeta$ diffusion weighted and ζ baseline images) with 7ξ unknowns (ξ proton density ρ_k images and 6ξ diffusion components, assuming diagonal symmetry of the diffusion tensors). While this system is highly non-linear, it can be solved as two separate linear problems.

First, proton densities (population fractions) of each spin pool can be calculated with an inversion of a linear system, noting that:

$$S_{0,j} = \sum_{k=1}^{\xi} \rho_k e^{-\frac{TE_j}{T_{2,k}}} \rightarrow \mathbf{S}_0 = \mathbf{E}\boldsymbol{\rho} \quad (5.5)$$

where \mathbf{S}_0 and $\boldsymbol{\rho}$ are $\zeta \times 1$ and $\xi \times 1$ column vectors with elements $S_{0,j}$ and ρ_k respectively, while \mathbf{E} is a $\zeta \times \xi$ matrix with elements $e^{\frac{TE_j}{T_{2,k}}}$. We can solve for $\boldsymbol{\rho}$ using non-negative least square estimation (Whittall and MacKay, 1989).

The second problem, that of finding the 6ξ unique elements of tensors \mathbf{D}_k could also be expressed as a system of independent equations, knowing the proton densities previously determined. However, because the unknown tensor components can assume both positive and negative values the straightforward inversion of this system can lead to solutions for population diffusion tensors \mathbf{D}_k that do not necessarily satisfy the positive definitiveness condition.

The key to formulating a robust fitting procedure is the assumption that the diffusion tensors of different white matter T₂ white matter components share the same eigenvector basis set, characterized the underlying fiber orientation. This argument is theoretically justified by the cylindrical symmetry of axonal and myelin geometries and is empirically supported by our recent findings (Avram et al., 2010c). Assuming that all proton pools have an identical basis set of eigen-directions (given by the rows of the 3x3 matrix $\mathbf{U} = [\mathbf{v}_1 \quad \mathbf{v}_2 \quad \mathbf{v}_3]^T$) but different eigenvalues (given by ξ diagonal matrices $\mathbf{\Lambda}_k$). The eigenvector decomposition of the diffusion tensors in Equation 5.4 becomes:

$$-\ln\left(\frac{S_{i,j}}{S_{0,j}}\right) = b\mathbf{g}_i^T \mathbf{U}^T \left(\sum_{k=1}^{\xi} f_k^j \mathbf{\Lambda}_k \right) \mathbf{U} \mathbf{g}_i = b\mathbf{g}_i^T \mathbf{U}^T \left[\sum_{k=1}^{\xi} f_k^j \begin{pmatrix} \lambda_1^k & 0 & 0 \\ 0 & \lambda_2^k & 0 \\ 0 & 0 & \lambda_3^k \end{pmatrix} \right] \mathbf{U} \mathbf{g}_i \quad (5.6)$$

The eigenvector matrix \mathbf{U} can be determined, for example, by conventional diffusion tensor fitting of a DTI dataset acquired with the shortest echo time. Once the eigenvectors are determined the number of unknowns is reduced to 3ξ thereby better conditioning the system of equations. More importantly however, all unknowns are positive and the non-negative least square solution will guarantee positive definite diffusion tensors for each T_2 component. Using consistent notation, we can define a $3\xi \times 1$ column vector of unknowns $\mathbf{\Lambda}$, the $\eta\zeta \times 1$ column vector of observations \mathbf{S} , and the $\eta\zeta \times 3\xi$ encoding matrix $\mathbf{\Sigma}$.

$$\mathbf{S} = S_{i+j(i-1)} = -\ln\left(\frac{S_{i,j}}{S_{0,j}}\right)$$

$$\mathbf{\Lambda} = \Lambda_{m+3k} = \lambda_m^k$$

$$\mathbf{\Sigma} = \Sigma_{m+3k, i+j(i-1)} = f_k^j (\mathbf{g}_i^T \mathbf{v}_m)^2$$

The system can be solved again with non-negativity constraints:

$$\mathbf{S} = \mathbf{\Sigma}\mathbf{\Lambda} \tag{5.7}$$

The proposed methodology has several advantages compared to alternative models of diffusion. First, it does not make any a priori assumptions about compartmentalization or exchange between pools. Second just like in the case of conventional DTI, because the system is formulated in terms of $\ln(S_i/S_0)$, the solution is robust to low signal to noise ratio in the original images. Finally, by assuming that all population diffusion tensors share the same eigenvectors, our model removes any dependence on fiber orientation allowing the robust estimation of positive definite

tensors for each T_2 component and the reliable quantization of average tensor metrics (diffusivities and FA) in white matter ROIs to characterize in vivo myelin water diffusion anisotropy with much improved statistical power.

5.5 White matter T_2 spectrum analysis confirms larger diffusion anisotropy of myelin water

Using our newly developed cardiac-gated multi-TE DTI pulse sequence (Avram et al., 2011a) we acquired on a healthy human volunteer an extensive DTI dataset with 18 echo times logarithmically spaced from 18ms to 120ms, and 10 non-collinear diffusion encoding directions with $b=600$ s/mm². To reduce the scan duration and minimize potential mis-registration due to subject motion, all 6 slices were obtained with a 88x88 matrix size on a 22x22cm² FOV using a single-shot uniform density spiral readouts of 36ms duration. Concurrently, low resolution spin echo images (46x46 matrix) were acquired for dynamic and inherent field map estimation (Avram et al., 2011b) during the $T_M=120$ ms stimulated echo mixing time. To increase the accuracy in estimating water fractions within the T_2 white matter spectrum (i.e. proton densities), diffusion was turned off and the same sequence (i.e. all other scan parameters kept constant) was used to acquire additional baseline images with 26 even shorter echo times, logarithmically spaced from 8ms to 20ms. As in the previous experiment, all readouts were reconstructed using field-map based off-resonance correction and distortion free images with excellent SNR were obtained.

Diffusion anisotropy was analyzed using the aforementioned methodology, for three T_2 white matter components, corresponding to the expected myelin water peak ($T_2=35\text{ms}$) axonal/extracellular water peak ($T_2=80\text{ms}$) and CSF ($T_2=2000\text{ms}$). First, accurate water fractions (proton densities) of each tissue component were estimated using baseline measurements acquired with 44 different echo times. Subsequently, the eigen-directions were calculated for each voxel by conducting a conventional diffusion tensor fit on the DTI dataset acquired with the shortest echo time ($TE=18\text{ms}$). For comparison, the DTI datasets acquired at all other echo times were also fitted with diffusion tensors in a conventional manner, and, as expected, identical eigenvectors were obtained throughout the entire white matter. Finally, using the estimated proton densities and eigen-orientations, the diffusivities were calculated for each tissue component and analyzed across the major white matter fibers including the genu and splenium of the corpus callosum, superior longitudinal fasciculus and the cortico-spinal tract.

The results of our T_2 spectrum analysis of human white matter diffusion anisotropy confirm our previous findings (Table 2). Diffusion anisotropy was found to be largest in the short T_2 water pool. Specifically, the fractional anisotropy of myelin water is 15% larger than that of axonal/extracellular water, and can be explained mainly through a 22% smaller radial diffusivity. Interestingly, the average myelin water tensor was also found to have a 11% smaller axial diffusivity compared to that of the

axonal/extracellular water tensor. The reduced axial diffusivity can be attributed in part to the organization of myelin sheaths in individual segments separated by nodes of Ranvier, approximately 0.2-1mm apart. Given the relatively long diffusion time ~150ms of the experiment restriction of axial mobility could become a significant factor even at moderate b-values. In our previous attempts to image myelin water, the slightly smaller axial diffusivity was likely obscured by overwhelming contribution from longer T₂ components due to insufficient myelin water specificity.

Table 2: Average diffusion characteristics calculated over a region of 1,452cm³ of white matter containing the major fibers

White matter Component	Myelin Water (35ms)	Axonal/Extracellular Water (80ms)	Cerebrospinal Fluid (2000 ms)
Fractional Anisotropy	0.425	0.37	<0.30
Radial Diffusivity	0.59	0.76	>1.00
Axial Diffusivity	1.20	1.35	>1.00

To ensure good conditioning of the two linear systems in eq. and eq. our current analysis minimizes the number of unknowns by approximating the white matter T₂ spectrum with three discrete components corresponding to the main observed water peaks. Provided that a sufficient large multi-TE DTI dataset is acquired, the diffusion characterization of T₂ water components can be improved using regularization methods to extend the assessment to a continuous smooth T₂ spectrum.

Finally, it is worth noting that, given the probable divergence of myelinated nerve fiber orientations within the large voxel size in our experiment, the results could

be underestimating FA and overestimating radial diffusivity in the myelin water compartment. Indeed, within non-parallel arrangements of nerve fibers, axial diffusion of myelin water within individual sheaths can increase the measured voxel-averaged radial diffusivity. To address this limitation, the experiment could be repeated with higher spatial resolution and/or more measurements at different diffusion orientations or b-values.

In conclusion, we have conducted an unprecedented experiment to better characterize diffusion anisotropy of white matter by exploring a new dimension with great potential for tissue specificity. DTI images acquired at multiple echo times were decomposed using a multi-exponential decay analysis to resolve tensors for individual T_2 tissue components. Overall, our results corroborate the findings from previous studies using MT-preparation to achieve MWW-DTI and provide convergent evidence that diffusion anisotropy of myelin water is determined mostly by the small radial diffusivity. While the multi-TE DTI experiment is not practical for clinical examinations due to its long scan duration, it can nevertheless guide the design of a clinical solution to achieve sufficient myelin water weighted DTI solution for a wide range of applications.

5.6 Need and feasibility of myelin water sensitization for clinical DTI applications

Our initial attempt to achieve myelin water weighted DTI using a magnetization transfer preparation pulse (Avram et al., 2010c) successfully detected diffusional

characteristics of myelin water but left several issues to be addressed before it could be used widely in translational and clinical applications. With a better understanding of diffusion anisotropy in different white matter T_2 components, we can now revisit these concerns and propose a strategy for efficient sensitization of myelin water in DTI.

The low sensitivity of the MT-DTI technique in Chapter 3 required multiple averages and imaging with low spatial resolution. The echo time reduction achieved with our short-TE spiral-out DTI technique can preserve more signal from myelin water thereby increasing the sensitivity of MWW DTI. Nevertheless, the MT prepared multi-TE experiment revealed that pulsed MT preparation has limited myelin water specificity even at short echo times (Fig. 8). Magnetization transfer contrast is modulated not only by the concentration of macromolecules, but also by their hydration kinetics resulting in contaminating contribution from water in extracellular and axonal compartments. Moreover, MT preparation requires large flip angles that can generate considerable RF power deposition, leading to subject discomfort and safety hazard for certain clinical populations (e.g. children).

A much more effective and efficient myelin water selection can be achieved from the acquisition of multiple images at different echo times. Myelin water imaging based on multi-exponential T_2 decay analysis is widely considered a very robust standard. While exclusive myelin water contrast requires the acquisition of very large datasets with low spatial resolution which is clinically impractical, DTI images acquired with

only a few different echo times could be used to derive sufficient myelin water sensitization for numerous clinical applications (Jones et al., 2004, Vidarsson et al., 2005). In the next chapter we develop an efficient myelin water weighted DTI technique for clinical examinations based on the simultaneous acquisition of two DTI datasets with different echo times (Avram et al., 2011a). It is hoped that MWW diffusion tensor metrics could be used as superior biomarkers to detect myelin microstructural changes during early brain development and neurological disorders of white matter origin.

Chapter 6: Integrated and efficient myelin water weighted (MWW) DTI using a two-TE acquisition

In this chapter we build on our understanding of diffusion properties of white matter T_2 components to propose an efficient alternative for achieving sufficient myelin water weighting in DTI by simultaneously acquiring images at two different echo times within a clinically acceptable scan duration. We demonstrate this new technique in healthy human volunteers, and discuss its potential for clinical applications.

6.1 Myelin water weighted DTI using two images with different echo times

Contributions from the short T_2 water components lead to an abrupt decrease of white matter diffusion anisotropy in the range of short echo times from 22ms to 52ms which are generally not achievable with conventional DTI. At short TE, both myelin water and water with longer T_2 (such as axonal or extracellular compartments) contribute significantly to the white matter MR signal, while at longer echo times the latter preponderate. If two measurements are acquired, with short TE and with long (clinical) TE, it is possible to isolate a signal component that is predominantly weighted toward myelin water.

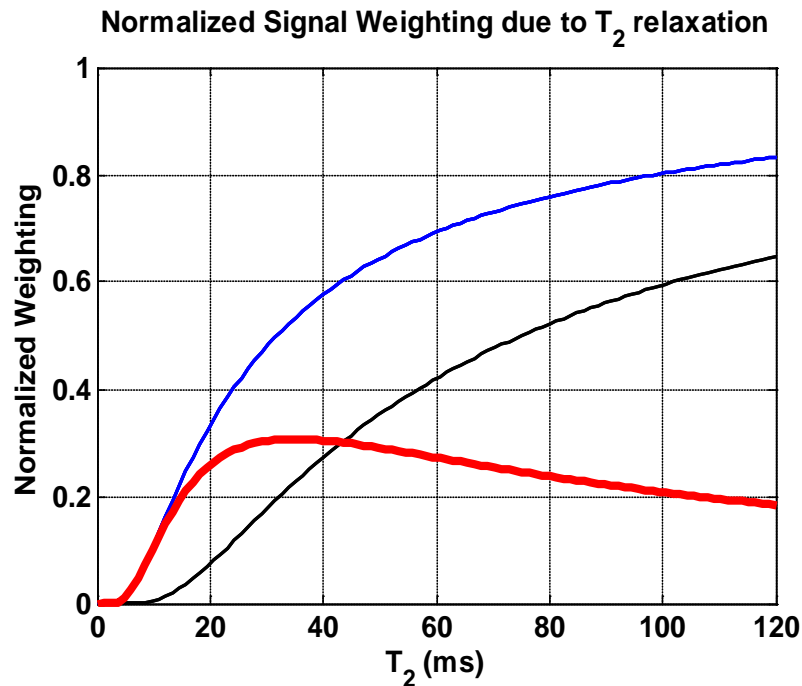


Figure 24: Normalized signal weighting due to transverse relaxation across the T_2 spectrum for images acquired with $TE_1=22\text{ms}$ (blue), $TE_2=72\text{ms}$ (black) and the difference signal of these two acquisitions (red) showing increased myelin water ($T_2 < 50\text{ms}$) weighting.

Figure 24 shows the normalized signal weighting due to the transverse relaxation of different T_2 components for measurements with $TE_1=22\text{ms}$ (blue) and $TE_2=72\text{ms}$ (red). The first measurement preserves significant contribution from short T_2 components while the second measurement contains mainly signal from long T_2 ($>50\text{ms}$) components such as axonal water or CSF. If we subtract the two datasets, we can efficiently remove contribution from the longer T_2 components and obtain a difference signal that is preferentially weighted towards myelin water. The myelin water specificity of this selection technique increases if the difference between TE_1 and TE_2 is small. However, reducing the difference between the two echo times also reduced sensitivity. To achieve sufficient myelin water specificity, we must choose two echo times at the

beginning and end of the short TE regime over which the multi-TE DTI experiment revealed most change (Avram et al., 2011a). In our experiments we chose TE1 the minimum TE (=22ms) for a given b-value (800 s/mm²). The second echo time TE2 (72ms) is chosen such that it results in a measurement with white matter SNR matched to that of the difference signal, allowing for direct comparison.

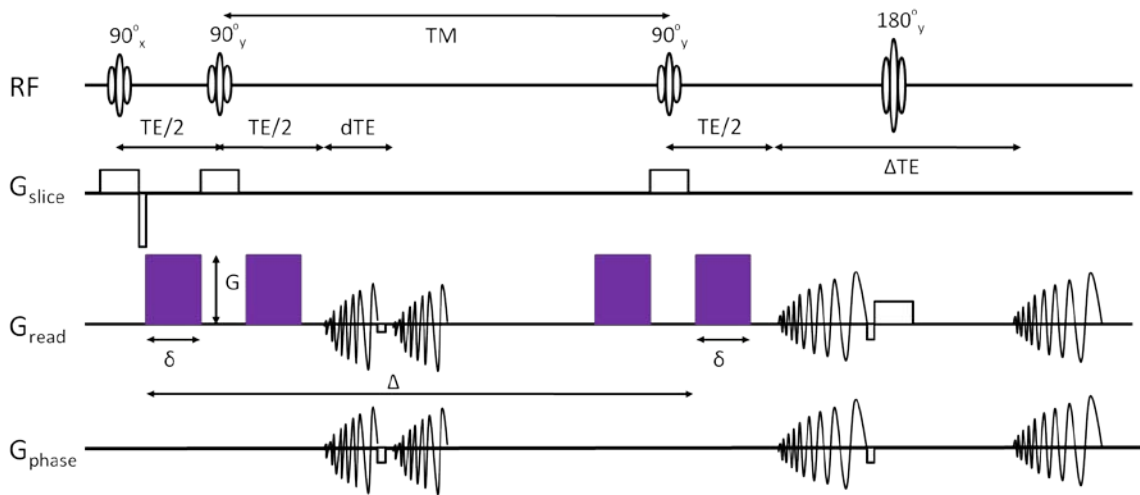


Figure 25: Pulse sequence diagram for rapid myelin water weighting DTI. Two diffusion weighted images with different TEs are acquired simultaneously (TE1=TE, TE2=TE+ΔTE). The difference between them can be used to calculate a short T₂ weighted diffusion tensor. Simultaneously, an inherent field map is acquired dynamically from two acquisitions along a secondary coherence pathway with dTE duration of phase accumulation.

We modified our short-TE DTI sequence with inherent and dynamic field-map correction developed in Chapter 4 to acquire two images concurrently (Fig. 25).

Specifically we used a 180° RF pulse to refocus the diffusion weighted stimulated echo signal and acquire it at a later echo time using the same segmented variable density spiral-out readout trajectory. Since the DW signal pathway is refocused only once it does not generate secondary coherence pathways that, due to motion-induced phase errors,

might lead to signal instabilities in the second acquisition (Norris et al., 1992, Schick, 1997). Nor does the refocusing pulse induce any significant magnetization transfer effects commonly observed in multi-TE multi-slice pulse sequences (Poon and Henkelman, 1992). Finally, the simultaneous acquisition of both echoes ensures that both images are inherently registered and any partial volume effects from long T_2 components (e.g. CSF) are inherently removed by subtraction.

6.2 Efficient acquisition of myelin water weighted DTI for clinical applications

Over multiple sessions, the newly developed short-TE SNAILS DTI pulse sequence was used to scan several healthy volunteers who provided informed written consent in compliance with the Institutional Review Board protocol at Duke University Medical Center. Ten slices were acquired with a 192x192 imaging matrix over a FOV of 22x22cm² with 5mm slice thickness. A diffusion sensitization of $b=800$ s/mm² was applied on 15 different orientations. The longitudinal period for the stimulated echo pathway ($T_M=120$ ms) accommodated two additional readouts used for inherent and dynamic field map (including eddy currents) correction as discussed in Chapter 4. Diffusion weighted images were acquired at two different echo times ($TE_1=22$ ms and $TE_2=72$ ms) with a sequence repetition time of $TR=3000$ s. For both echoes the same variable density spiral out trajectory with inherent self-navigation properties was used to acquire each image in 10 shots. All images were reconstructed with simultaneous

motion and field-map based off-resonance correction using the previously discussed pipeline (Fig. 17). The total scan time for this sequence was 8:30 min.

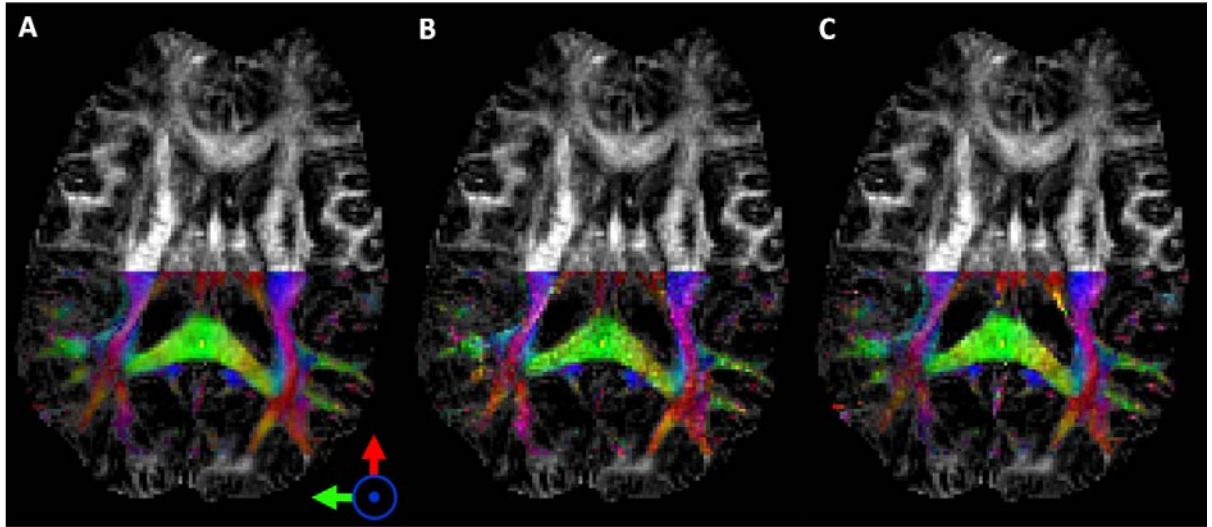


Figure 26: Fractional anisotropy maps with principal diffusion orientation color-coding overlay for the DTI images acquired with short TE1=22ms, (A) and with clinical TE2=72ms (B) and the Myelin water weighted (MWW) diffusion tensor (C) computed based on the two DTI acquisitions with different echo times. As expected, all tensors show identical preferred direction of diffusion.

The DTI datasets acquired with short and long TE's were fitted separately with a rank-2 tensor. An additional dataset was created by subtracting the two acquisitions to obtain images with significant myelin water weighting (MWW). Shown in Figure 26 are the corresponding FA images color-coded based on the principal direction of diffusion, obtained from the three DTI datasets (short TE, long TE and MWW). As expected, all three tensors exhibit identical principal diffusion directions along the orientations of major white matter tracts, suggesting that both short and long T₂ components (i.e. myelin and axonal/extracellular water respectively) have similar directionality of diffusion. The cylindrical symmetry in both axonal and myelin microstructures offer

theoretical support for this observation, while our results from Chapter 3 provide strong empirical for this argument (Avram et al., 2010b).

A quantitative comparison of fractional anisotropies (Fig. 27: top row) reveals that, as expected from our multi-TE experiment, the FA in the corpus callosum increases significantly by reducing the echo time from the clinical TE=72ms to TE=22ms. When measurements at both echo times are used to preferentially increase the contribution of the short T₂ components in the MWW tensor, the FA increases further. The differences observed in radial diffusivities are also consistent with our previous findings (Fig 27: bottom row). Specifically, radial diffusivity decreases with echo time as more signal from short T₂ components is preserved. The myelin water weighted DTI has the highest sensitization to myelin and therefore the smallest radial diffusivity. It can be observed that in periventricular white matter CSF contamination due to partial volume effects is unavoidable. Despite the high in-plane resolution, voxels at the interface between white matter and CSF exhibit a smaller FA at large echo times due to CSF contribution to radial diffusivity tensor components. In the MWW images, these effects however, are mitigated by the subtraction of perfectly registered images with different echo times; long T₂ (~2000s) water in CSF for example will experiences similar transverse relaxation signal decay at TE=22ms and TE=72ms.

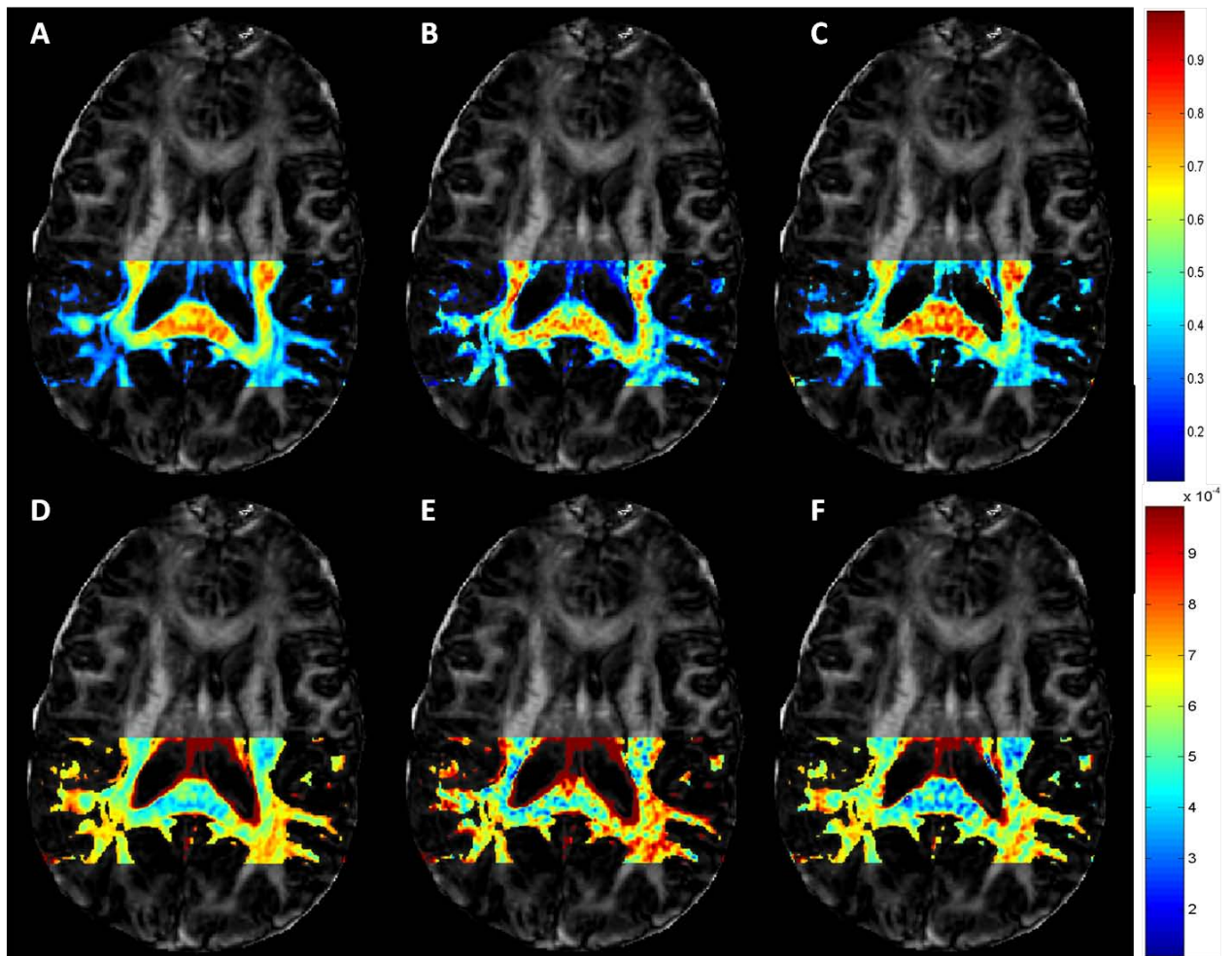


Figure 27: Fractional anisotropy (top row) and radial diffusivity (bottom row) comparison between DTI acquired with short TE1=22ms (A,D), DTI acquired with clinical TE2=72ms (B,E) and Myelin water weighted (MWW) DTI (C,F) computed based on the two acquisitions with different echo times. The MWW diffusion tensor has significantly large FA due to a smaller radial diffusivity, suggesting that the diffusion of water between the myelin sheaths is more anisotropic compared to that of axonal/intercellular water.

While the simultaneous acquisition of both echoes ensures perfect registration between DTI datasets allowing effective suppression of long and intermediate T_2 components, the accuracy of our quantitative comparison might be limited by two other factors. First, the signal-to-noise-ratio (SNR) is intrinsically smaller for images acquired at longer echo times (Farrell et al., 2007) possibly leading to shorter fractional anisotropy

values. However, our choice of the two echo times was such that, given the average white matter $T_2=69\text{ms}$ at 3T (Stanisz et al., 2005), the long TE and MWW datasets have roughly matched theoretical white matter SNR values. Secondly, as discussed in our previous myelin specific DTI experiments, intravoxel coherence of white matter fiber orientations might lead to underestimated fractional anisotropy and overestimated radial diffusivity values for myelin water. In voxels containing even slightly divergent fibers, the averaged myelin water rank-2 diffusion tensor anisotropy could be significantly reduced due to axial diffusion along the fibers contributing to the measured average radial diffusivity.

The tissue specificity of our newly developed MWW DTI technique can be increased by acquiring additional measurements at multiple echo times and designing efficient filters for myelin water. Non-diffusion weighted myelin water images have already been reliably estimated from linear combinations of images acquired with as few as 3 different echo times (Jones et al., 2004, Vidarsson et al., 2005). Nevertheless, using only two TEs, our elegant solution ensures perfect registration between all DTI images and, within a clinical time frame, provides sufficient myelin sensitization to investigate diffusion anisotropy effects due to short T_2 myelin water. These effects are generally detectable only in the short TE range (Fig 21-22) (Avram et al., 2011a), and hence cannot be characterized with traditional clinical DTI techniques.

It is hoped that our MWW-DTI method can find wide clinical applications to investigate the origins of many myelin-related white matter pathologies in pediatric brain disorders, or to allow early detection in myelin microstructural changes in demyelination diseases in adults.

Chapter 7: Conclusions and Future Work

In the final chapter we point out several conclusive remarks regarding the applicability of our newly developed short-TE DTI methodology. We discuss its potential integration with advanced DTI models and qualify the limitations of myelin water DTI in general. Finally, we outline the design of a study for validating the clinical utility of our technique by imaging healthy white matter maturation in a pediatric population.

7.1 Short-TE DTI for investigating diffusion anisotropy of myelin water

Traditional DTI techniques cannot successfully dissociate changes of individual signal components (axon, myelin, CSF, vasculature) and are therefore limited to a qualitative assessment of microstructural changes during neurological disorders of white matter origin. To address this limitation, we have developed an integrated clinical DTI methodology capable to investigate changes in myelin microstructure.

The combined strategy of using both stimulated echo diffusion preparation and spiral out readout trajectory minimizes echo time and optimizes sensitivity to myelin water. Our novel short-TE DTI methodology can thus achieve echo times as short as 18ms without the need for expensive custom designed insert gradient coils (Feldman et al., 2011). The echo time reduction preserves considerable signal from myelin water

allowing for the first time the possibility of characterizing myelin microstructure directly with DTI.

To isolate the tissue specific information gathered within the short TE-DTI measurement, myelin water selection techniques must be incorporated. While magnetization transfer can be naturally integrated with DTI to achieve myelin water weighting, its limited specificity, low sensitivity and large RF power deposition diminish its prospect for clinical use. Provided that sufficiently short echo times can be achieved, a direct and efficient approach is to estimate a MWW tensor from two measurements with different echo times. In our final implementation, both echoes are acquired simultaneously within ten minutes to produce high resolution MWW-DTI images which can be analyzed alongside DTI images acquired with conventional echo times in studies investigating myelin microstructural changes during early brain maturation or neurological disorders of white matter origin. The newly developed methodology has the potential to open new avenues in modern neuroimaging by enabling a new dimensionality to the DTI measurement.

7.3 Integrating short-TE DTI with advanced diffusion models

Over the last decade, researchers have developed advanced DTI models to better characterize the intravoxel tissue microstructure by quantifying deviations from Gaussianity in the diffusion displacement probability distributions (Tuch et al., 2003, Jensen et al., 2005, Liu et al., 2010). Generally these techniques require the acquisition of

DW images with large b-values and numerous diffusion orientations. The technical challenges of implementing large b-value acquisitions on clinical human scanners often represent an obstacle towards the clinical validation and adoption of these techniques.

The short-TE DTI pulse sequence developed in Chapter 4 is an ideal solution for large b-value DTI as it provides optimal white matter sensitivity and inherently corrects for most common sources of image artifacts (motion, eddy currents) to generate high resolution images with excellent spatial accuracy. In our final MWW-DTI implementation (Chapter 6) the concurrent acquisition of an additional, fully registered DTI dataset can be used to further increase sensitivity. More importantly however, by analyzing anisotropy along a new dimension (of T2 transverse relaxation rates) our new methodology provides complementary, tissue specific information to the aforementioned techniques. For example, higher order tensor metrics (e.g. kurtosis tensor) of myelin water diffusion could potentially provide sensitive biomarkers for detecting myelin microstructural changes during axonal ensheathment, demyelination or myelin repair. The analysis advanced MWW-DTI datasets could result in the development of novel diffusion models characterizing the highly ordered, packed myelin microarchitecture.

7.2 Limitations of myelin water weighted DTI

In Chapter 5 the cardiac gated multi-TE DTI study estimated for the first time the myelin water diffusion tensor in human white matter, and confirmed that diffusion of

myelin water is highly anisotropic. Nevertheless, our results are likely underestimating the true anisotropy of myelin water diffusion.

Variation in the orientation distribution of myelinated fibers within a typical white matter MR voxel can significantly affect the observed anisotropy. The macroscopic anisotropy measured as an average of a collection of highly prolate intravoxel (myelin water) diffusion tensors of individual fibers decreases with increasing fiber divergence. Axial diffusivity of non-parallel fibers can significantly contribute toward the radial diffusivity of the averaged tensor. In the extreme case of crossing fibers the diffusion tensors become oblong, potentially more isotropic leading to error in the tensor calculation (Mori and van Zijl, 2002). These concerns can be addressed by increasing spatial resolution (e.g. with a 3D acquisition) or incorporating advanced multi-tensor diffusion models.

Another source of error in our measurement of the in vivo myelin water diffusion tensor is the potential exchange between different T_2 water pools. Studies using neutron-scattering to measure the deuterium-hydrogen exchange in excised rabbit sciatic nerve report a time constant of 12 minutes (Kirschner et al., 1975, Peled, 2000). On the other hand, model-based analyses of multi-exponential T_2 decay in white matter seems to suggest that the exchange time constant for short T_2 myelin water is on the order of 400ms in excised bovine optic nerve (Stanisz et al., 1999) and 700ms in human white matter (Labadie et al., 2008). These investigations suggest that the exchange

dynamics of myelin water are slow, but not negligible. Further studies are necessary to assess the effect of this exchange on the observed myelin water anisotropy.

Both intravoxel fiber coherence and myelin water exchange contribute to underestimating the diffusion anisotropy in myelin tissue. While further experiments can be carried out to characterize these effects, for clinical use it might not be necessary (or practical) to measure absolute myelin water diffusion anisotropy. Rather, the amount of MWW sensitization achieved with our MWW-DTI methodology might prove sufficient for detecting clinically relevant myelin microstructural changes.

7.4 Monitoring myelination during healthy brain development

It is known that the human brain is not fully developed at birth. Indeed, various white matter regions will mature in myelination at different time courses. For example, the primary functional systems such as motor, sensory, and visual areas will have full myelination within the first year, while the regions involved in higher cognitive functions (e.g. frontal lobe) do not fully develop until after the first decade. Shown in Fig. 28 are examples of myelination time courses in different brain regions.

This region-dependent myelin and white matter maturation time course provides an ideal testbed for our myelin specific DTI, as the primary functional regions (e.g. occipital lobe) can serve as internal controls, along with the less mature frontal lobe, to validate the clinical utility of our myelin specific DTI. We are currently carrying out a preliminary clinical study applying MWW-DTI to image myelin microstructural changes

in developing brains where different regions have distinctly different maturation time courses, providing internal control within the same brain to validate the clinical value of our new technique.

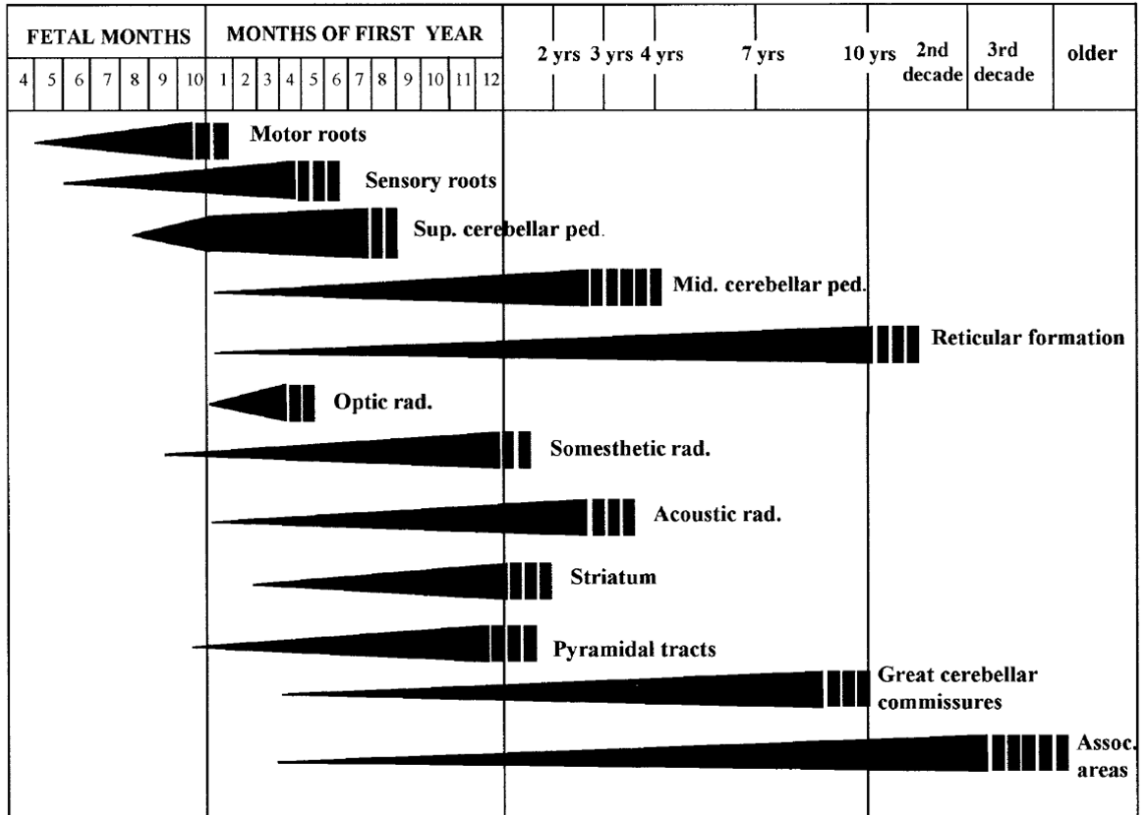


Figure 28: Timeline of myelination in healthy human brain adapted from (Baumann and Pham-Dinh, 2001). Maturation of cognitive abilities occurs in synchrony with myelination of corresponding white matter pathways.

Upon clinical validation, the newly developed myelin specific DTI methodology can be widely applied in even younger children to investigate the origins of many myelin and white matter pathologies in pediatric brain disorders, or to allow early detection in myelin microstructural changes in demyelination diseases in adults (e.g. multiple sclerosis).

Appendix A: Glossary of Terms

ADC	Apparent diffusion coefficient [mm^2/s]
ASD	autism spectrum disorders
<i>b</i>	Diffusion sensitization [s/mm^2]
<i>b</i>	Diffusion sensitization tensor matrix [s/mm^2]
BPP	Bloembergen-Purcell-Pound (model for molecular basis of magnetic relaxation)
<i>c</i>	Concentration [mol/m^3]
CARS	Coherent Anti-Stokes Raman Scattering
CNP	2'3'-Cyclic nucleotide 3'-phosphohydrolase
CNS	Central nervous system
CPMG	Carr-Purcell-Meiboom-Gill (pulse sequence)
CSF	Cerebrospinal fluid
CW	Continuous wave
<i>D</i>	diffusion constant [mm^2/s]
<i>D</i>	diffusion tensor [mm^2/s]
DIR	Double inversion recovery
DSI	Diffusion spectrum imaging
DTI	Diffusion tensor imaging
DTS	Diffusion tensor spectroscopy

DW	Diffusion weighted
D_{ij}	Components of the diffusion tensor
δ	Duration of diffusion encoding gradient pulse [ms]
Δ	Separation between diffusion encoding gradient pulses [ms]
EPI	Echo planar imaging
η	Viscosity [cp]
F	Average driving force
FA	Fractional anisotropy
FID	Free induction decay
FLAIR	Fluid attenuated inversion recovery
FOV	Field of view
$\Delta\phi$	Phase accumulation [rad]
$\langle\Delta\phi^2\rangle$	Mean square phase accumulation [rad ²]
G	Gibbs free energy [J] or gradient strength [mT/m]
GDTI	Generalized diffusion tensor imaging
GM	Gray matter
\mathbf{g}_i	Diffusion gradient orientation unit vector
HARDI	High angular resolution diffusion imaging
\hbar	Reduced Planck constant $1.054 \times 10^{-34} \text{ J} \cdot \text{s}/\text{rad}$
h	Planck constant $6.626 \times 10^{-34} \text{ J} \cdot \text{s}$

J	Flux [$1/m^3/s$] or angular momentum [$N \cdot m \cdot s$]
$J(\omega)$	Spectral density of microscopic local magnetic field variations [T/Hz]
k	k-space vector [$1/m$]
k_B	Boltzmann's constant $1.380 \times 10^{-23} J/K$
$\lambda_1, \lambda_2, \lambda_3$	Principal diffusivities [mm^2/s]
$\lambda_{ }$	Axial diffusivity [mm^2/s]
λ_{\perp}	Radial diffusivity [mm^2/s]
M	Macroscopic magnetization vector [A/m]
MAG	myelin associated glycoprotein
MBP	myelin basic protein
MD	Mean diffusivity
MR	Magnetic resonance
MRI	Magnetic resonance imaging
MT	Magnetization transfer
MTR	Magnetization transfer ratio
MOG	myelin oligodendrocyte glycoprotein
MW	Myelin water
MWW	Myelin water weighting
MWF	Myelin water fraction

μ	Chemical potential [$J/moles$] or magnetic dipole moment [$A \cdot m^2$]
NAA	N-acetyl aspartate
NAWM	Normal appearing white matter
NEX	Number of excitations
NMR	Nuclear magnetic resonance
n	number of moles
N_A	Avogadro's number $6.022 \times 10^{23} \text{ 1/mol}$
P	pressure [atm]
P_0	Standard pressure [atm]
PD	Proton density
PGSE	Pulsed gradient spin echo
PGSTE	Pulsed gradient stimulated echo
PLP	proteo-lipid protein
PNS	Peripheral nervous system
ppm	Parts per million
QSI	q-space diffusion imaging
r	Intermolecular distance [m]
r	Spin displacement [m]
Δr	Microscopic displacement of Brownian particle [m]
R	Gas constant 8.3145 J/K/mol

RF	Radio frequency
ROI	Region of interest
S	entropy [J] or MR signal
SAR	Specific absorption ratio
SE	Spin echo
SENSE	Sensitivity encoding
SNAILS	Self-navigated interleaved spirals
SNR	Signal to noise ratio
SPHERE	simulated phase evolution rewinding
STEAM	Stimulated echo acquisition mode
STE	Stimulated echo
T	temperature [K]
TE	Echo time
TM	Mixing (longitudinal) period of stimulated echo
TR	Repetition time
TRSE	Twice refocused spin echo
τ	time duration of diffusion [s]
τ_c	Molecular tumbling correlation time [s]
V	volume [m^3]
v	Molecular velocity [m/s]

WM	White matter
ω_0	Resonance Larmor frequency [<i>rad</i>]
$\Delta x, \Delta y, \Delta z$	one dimensional displacements of Brownian particle [<i>mm</i>]
$\langle \Delta x^2 \rangle$	One dimensional mean squared displacement [<i>mm</i> ²]
∇^2	Laplacian operator

References

1. Abe O, Aoki S, Hayashi N, Yamada H, Kunimatsu A, Mori H, Yoshikawa T, Okubo T, Ohtomo K (2002) Normal aging in the central nervous system: quantitative MR diffusion-tensor analysis. *Neurobiol Aging* 23:433-441.
2. Ahn CB, Kim JH, Cho ZH (1986) High-speed spiral-scan echo planar NMR imaging-I. *IEEE Trans Med Imaging* 5:2-7.
3. Allen NJ, Barres BA (2009) NEUROSCIENCE Glia - more than just brain glue. *Nature* 457:675-677.
4. Andersson JL, Skare S, Ashburner J (2003) How to correct susceptibility distortions in spin-echo echo-planar images: application to diffusion tensor imaging. *Neuroimage* 20:870-888.
5. Andrews TJ, Osborne MT, Does MD (2006a) Diffusion of myelin water. *Magn Reson Med* 56:381-385.
6. Andrews TJ, Osborne MT, Does MD (2006b) Diffusion of myelin water. *Magnet Reson Med* 56:381-385.
7. Ashtari M, Kumra S, Bhaskar SL, Clarke T, Thaden E, Cervellione KL, Rhinewine J, Kane JM, Adesman A, Milanaik R, Maytal J, Diamond A, Szeszko P, Ardekani BA (2005) Attention-deficit/hyperactivity disorder: a preliminary diffusion tensor imaging study. *Biol Psychiatry* 57:448-455.
8. Assaf Y, Basser PJ (2005) Composite hindered and restricted model of diffusion (CHARMED) MR imaging of the human brain. *Neuroimage* 27:48-58.
9. Assaf Y, Blumenfeld-Katzir T, Yovel Y, Basser PJ (2008) AxCaliber: a method for measuring axon diameter distribution from diffusion MRI. *Magn Reson Med* 59:1347-1354.

10. Assaf Y, Pasternak O (2008) Diffusion tensor imaging (DTI)-based white matter mapping in brain research: a review. *J Mol Neurosci* 34:51-61.
11. Avram AV, Guidon A, Liu C, Song AW (2011a) Multi-TE Diffusion Tensor Imaging in Vivo. In: *Proceeding of the 19th Annual Meeting of the International Society for Magnetic Resonance in Medicine* Montreal, Canada.
12. Avram AV, Guidon A, Petrella J, Morgenlander J, Song AW (2010a) Magnetization Transfer DTI in Multiple Sclerosis. In: *Proceedings of the 18th Annual Meeting of the ISMRM*, p 4316 Stockholm, Sweden.
13. Avram AV, Guidon A, Song AW (2008) Magnetization Transfer Prepared Diffusion Tensor Imaging In: *Proceedings of the 16th Annual Meeting of the ISMRM*, p 765 Toronto, Canada.
14. Avram AV, Guidon A, Song AW (2009) Stimulated-Echo DTI with Magnetization Transfer Contrast for Myelin Specificity. In: *Proceedings of the 17th Annual Meeting of the ISMRM*, p 3523 Honolulu, Hawai'i, USA.
15. Avram AV, Guidon A, Song AW (2010b) Myelin water weighted diffusion tensor imaging. *Neuroimage* 53:132-138.
16. Avram AV, Guidon A, Song AW (2010c) Myelin water weighted diffusion tensor imaging. *Neuroimage* 53:132-138.
17. Avram AV, Truong TK, Guidon A, Liu C, Song AW (2011b) Dynamic and Inherent B0 correction for DTI using stimulated echo spiral imaging. In: *Proceedings of the 19th Annual Meeting of the International Society for Magnetic Resonance in Medicine* Montreal, Canada.
18. Azevedo FAC, Carvalho LRB, Grinberg LT, Farfel JM, Ferretti REL, Leite REP, Jacob W, Lent R, Herculano-Houzel S (2009) Equal Numbers of Neuronal and Nonneuronal Cells Make the Human Brain an Isometrically Scaled-Up Primate Brain. *Journal of Comparative Neurology* 513:532-541.

19. Barkovich AJ (2000) Concepts of myelin and myelination in neuroradiology. *AJNR Am J Neuroradiol* 21:1099-1109.
20. Barmet C, De Zanche N, Wilm BJ, Pruessmann KP (2009) A transmit/receive system for magnetic field monitoring of in vivo MRI. *Magnet Reson Med* 62:269-276.
21. Barnea-Goraly N, Eliez S, Hedeus M, Menon V, White CD, Moseley M, Reiss AL (2003a) White matter tract alterations in fragile X syndrome: preliminary evidence from diffusion tensor imaging. *Am J Med Genet B Neuropsychiatr Genet* 118B:81-88.
22. Barnea-Goraly N, Kwon H, Menon V, Eliez S, Lotspeich L, Reiss AL (2004) White matter structure in autism: preliminary evidence from diffusion tensor imaging. *Biol Psychiatry* 55:323-326.
23. Barnea-Goraly N, Menon V, Krasnow B, Ko A, Reiss A, Eliez S (2003b) Investigation of white matter structure in velocardiofacial syndrome: a diffusion tensor imaging study. *Am J Psychiatry* 160:1863-1869.
24. Basser PJ, Jones DK (2002) Diffusion-tensor MRI: theory, experimental design and data analysis - a technical review. *NMR Biomed* 15:456-467.
25. Basser PJ, Mattiello J, LeBihan D (1994a) Estimation of the effective self-diffusion tensor from the NMR spin echo. *J Magn Reson B* 103:247-254.
26. Basser PJ, Mattiello J, LeBihan D (1994b) MR diffusion tensor spectroscopy and imaging. *Biophys J* 66:259-267.
27. Basser PJ, Pierpaoli C (1998) A simplified method to measure the diffusion tensor from seven MR images. *Magn Reson Med* 39:928-934.

28. Baumann N, Pham-Dinh D (2001) Biology of oligodendrocyte and myelin in the mammalian central nervous system. *Physiol Rev* 81:871-927.
29. Beaulieu C (2002) The basis of anisotropic water diffusion in the nervous system - a technical review. *NMR Biomed* 15:435-455.
30. Bhagat YA, Beaulieu C (2004) Diffusion anisotropy in subcortical white matter and cortical gray matter: changes with aging and the role of CSF-suppression. *J Magn Reson Imaging* 20:216-227.
31. Biton IE, Duncan ID, Cohen Y (2006) High b-value q-space diffusion MRI in myelin-deficient rat spinal cords. *Magn Reson Imaging* 24:161-166.
32. Blezer EL, Bauer J, Brok HP, Nicolay K, t Hart BA (2007) Quantitative MRI-pathology correlations of brain white matter lesions developing in a non-human primate model of multiple sclerosis. *NMR Biomed* 20:90-103.
33. Bloch F, Hansen WW, Packard M (1946) The Nuclear Induction Experiment. *Physical Review* 70:474.
34. Bloembergen N, Purcell EM, Pound RV (1948) Relaxation Effects in Nuclear Magnetic Resonance Absorption. *Physical Review* 73:679.
35. Bodammer N, Kaufmann J, Kanowski M, Tempelmann C (2004) Eddy current correction in diffusion-weighted imaging using pairs of images acquired with opposite diffusion gradient polarity. *Magn Reson Med* 51:188-193.
36. Boltzmann L (1875) Über das Wärme gleichgewicht von Gasen auf welche äuszere Kräfte wirken. *Wien Ber* 72:427-457.
37. Boltzmann L (1877) Über die Beziehung swischen dem zweiten Hauptsatz der mechanischen Wärmetheorie und der Wahrscheinlichkeitsrechnung respektive den Sätzen über des Wärmegleichgewicht. *Wien Ber* 76:373-435.

38. Brant-Zawadzki M, Enzmann DR (1981) Using computed tomography of the brain to correlate low white-matter attenuation with early gestational age in neonates. *Radiology* 139:105-108.
39. Broca P (1861) Sur le siège de la faculté du langage articulé. *Bull Soc anat de Paris* 6:355.
40. Brochet B, Dousset V (1999) Pathological correlates of magnetization transfer imaging abnormalities in animal models and humans with multiple sclerosis. *Neurology* 53:S12-17.
41. Brown R (1828) A brief account of microscopical observations made in the months of June, July and August, 1827, on the particles contained in the pollen of plants; and on the general existence of active molecules in organic and inorganic bodies. In: *Phil Mag*, vol. 4, pp 161-173.
42. Callaghan PT (1991) *Principles of Nuclear Magnetic Resonance Microscopy*. Oxford, UK: Oxford University Press.
43. Callaghan PT, Coy A, MacGowan D, Packer KJ, Zelaya FO (1991) Diffraction-like effects in NMR diffusion studies of fluids in porous solids. *Nature* 351:467-469.
44. Carr HY, Purcell EM (1954) Effects of Diffusion on Free Precession in Nuclear Magnetic Resonance Experiments. *Physical Review* 94:630.
45. Chen B, Guo H, Song AW (2006) Correction for direction-dependent distortions in diffusion tensor imaging using matched magnetic field maps. *Neuroimage* 30:121-129.
46. Clausius RJE (1857) Über die Art der Bewegung, die wir Wärme nennen. *Annalen der Physik* 100:353-379.

47. Clausius RJE (1862) Über die Wärmeleitung gasförmiger Körper. *Annalen der Physik* 115:1-57.
48. Cohen MS, Weisskoff RM, Rzedzian RR, Kantor HL (1990) Sensory stimulation by time-varying magnetic fields. *Magn Reson Med* 14:409-414.
49. Cohen Y, Assaf Y (2002) High b-value q-space analyzed diffusion-weighted MRS and MRI in neuronal tissues - a technical review. *NMR Biomed* 15:516-542.
50. Counsell SJ, Allsop JM, Harrison MC, Larkman DJ, Kennea NL, Kapellou O, Cowan FM, Hajnal JV, Edwards AD, Rutherford MA (2003) Diffusion-weighted imaging of the brain in preterm infants with focal and diffuse white matter abnormality. *Pediatrics* 112:1-7.
51. Davidovitch M, Patterson B, Gartside P (1996) Head circumference measurements in children with autism. *J Child Neurol* 11:389-393.
52. Dayan P, Abbott LF (2005) *Theoretical Neuroscience: Computational and Mathematical Modeling of Neural Systems*: MIT Press.
53. Does MD, Beaulieu C, Allen PS, Snyder RE (1998) Multi-component T1 relaxation and magnetisation transfer in peripheral nerve. *Magn Reson Imaging* 16:1033-1041.
54. Ducreux D, Nasser G, Lacroix C, Adams D, Lasjaunias P (2005) MR diffusion tensor imaging, fiber tracking, and single-voxel spectroscopy findings in an unusual MELAS case. *AJNR Am J Neuroradiol* 26:1840-1844.
55. Einstein A (1905) Über die von der molekularkinetischen Theorie der Wärme geforderte Bewegung von in ruhenden Flüssigkeiten suspendierten Teilchen. *Annalen der Physik* 17:549-560.
56. Ellegood J, Hanstock CC, Beaulieu C (2006) Diffusion tensor spectroscopy (DTS) of human brain. *Magn Reson Med* 55:1-8.

57. Eng J, Ceckler TL, Balaban RS (1991) Quantitative 1H magnetization transfer imaging in vivo. *Magn Reson Med* 17:304-314.
58. Engelbrecht V, Scherer A, Rassek M, Witsack HJ, Modder U (2002) Diffusion-weighted MR imaging in the brain in children: findings in the normal brain and in the brain with white matter diseases. *Radiology* 222:410-418.
59. Farrell JA, Landman BA, Jones CK, Smith SA, Prince JL, van Zijl PC, Mori S (2007) Effects of signal-to-noise ratio on the accuracy and reproducibility of diffusion tensor imaging-derived fractional anisotropy, mean diffusivity, and principal eigenvector measurements at 1.5 T. *J Magn Reson Imaging* 26:756-767.
60. Feinberg DA, Kiefer B, Litt AW (1994) Dual contrast GRASE (gradient-spin echo) imaging using mixed bandwidth. *Magnet Reson Med* 31:461-464.
61. Feldman RE, Scholl TJ, Alford JK, Handler WB, Harris CT, Chronik BA (2011) Results for diffusion-weighted imaging with a fourth-channel gradient insert. *Magnet Reson Med* n/a-n/a.
62. Fick AE (1855a) On Liquid Diffusion. *Philos Mag J Sci* 10:31-39.
63. Fick AE (1855b) Über Diffusion. *Ann Phys Chem* 94:59-86.
64. Filippi CG, Lin DD, Tsiouris AJ, Watts R, Packard AM, Heier LA, Ulug AM (2003) Diffusion-tensor MR imaging in children with developmental delay: preliminary findings. *Radiology* 229:44-50.
65. Filippi M, Grossman RI (2002) MRI techniques to monitor MS evolution: the present and the future. *Neurology* 58:1147-1153.
66. Filley CM (2001) *The behavioral neurology of white matter*: Oxford University Press.

67. Fombonne E (2003) Epidemiological surveys of autism and other pervasive developmental disorders: an update. *J Autism Dev Disord* 33:365-382.
68. Fourier JBJb (1822) *Theorie analytique de la chaleur [microform]* / par M. Fourier. Paris :: F. Didot.
69. Frahm J, Haase A, Matthaei D (1986) Rapid three-dimensional MR imaging using the FLASH technique. *J Comput Assist Tomogr* 10:363-368.
70. Frahm J, Merboldt KD, Hänicke W, Haase A (1985) Stimulated echo imaging. *Journal of Magnetic Resonance (1969)* 64:81-93.
71. Frank LR (2001) Anisotropy in high angular resolution diffusion-weighted MRI. *Magn Reson Med* 45:935-939.
72. Frank LR (2002) Characterization of anisotropy in high angular resolution diffusion-weighted MRI. *Magn Reson Med* 47:1083-1099.
73. Frank LR, Jung Y, Inati S, Tyszka JM, Wong EC (2010) High efficiency, low distortion 3D diffusion tensor imaging with variable density spiral fast spin echoes (3D DW VDS RARE). *Neuroimage* 49:1510-1523.
74. Frankenhaeuser B, Huxley AF (1964) The Action Potential in the Myelinated Nerve Fiber of *Xenopus Laevis* as Computed on the Basis of Voltage Clamp Data. *J Physiol* 171:302-315.
75. Frey KA, Wieland DM, Brown LE, Rogers WL, Agranoff BW (1981) Development of a tomographic myelin scan. *Ann Neurol* 10:214-221.
76. Friede RL (1986) Relation between myelin sheath thickness, internode geometry, and sheath resistance. *Exp Neurol* 92:234-247.

77. Frullano L, Wang C, Miller RH, Wang Y (2011) A Myelin-Specific Contrast Agent for Magnetic Resonance Imaging of Myelination. *J Am Chem Soc.*
78. Gall FJ, Spurzheim JC (1810) *Anatomie und Physiologie des Nervensystems im Allgemeinen und des Gehirns insbesondere.* Paris: F. Schoell.
79. Gareau PJ, Rutt BK, Karlik SJ, Mitchell JR (2000) Magnetization transfer and multicomponent T2 relaxation measurements with histopathologic correlation in an experimental model of MS. *J Magn Reson Imaging* 11:586-595.
80. Gerlach W, Stern O (1922) Das magnetische Moment des Silberatoms. *Zeitschrift für Physik A Hadrons and Nuclei* 9:353-355-355.
81. Gersonde K, Felsberg L, Tolxdorff T, Ratzel D, Ströbel B (1984) Analysis of multiple T2 proton relaxation processes in human head and imaging on the basis of selective and assigned T2 values. *Magnet Reson Med* 1:463-477.
82. Gibbs JW (1873) A Method of Geometrical Representation of the Thermodynamic Properties of Substances by Means of Surfaces. *Transactions of the Connecticut Academy of Arts and Sciences* 2:382-404.
83. Glenn OA, Henry RG, Berman JI, Chang PC, Miller SP, Vigneron DB, Barkovich AJ (2003) DTI-based three-dimensional tractography detects differences in the pyramidal tracts of infants and children with congenital hemiparesis. *J Magn Reson Imaging* 18:641-648.
84. Gouy LG (1889) Sur le mouvement brownien. *Comptes Rendus Acad d Sci, Paris* 109:102.
85. Grossman RI (1999) Application of magnetization transfer imaging to multiple sclerosis. *Neurology* 53:S8-11.

86. Haacke EM (1999) Magnetic resonance imaging: physical principles and sequence design: J. Wiley & Sons.
87. Hagmann P, Thiran JP, Jonasson L, Vandergheynst P, Clarke S, Maeder P, Meuli R (2003) DTI mapping of human brain connectivity: statistical fibre tracking and virtual dissection. *Neuroimage* 19:545-554.
88. Hahn EL (1950) Spin Echoes. *Physical Review* 80:580.
89. Hamano K, Takeya T, Iwasaki N, Nakayama J, Ohto T, Okada Y (1998) A quantitative study of the progress of myelination in the rat central nervous system, using the immunohistochemical method for proteolipid protein. *Brain Res Dev Brain Res* 108:287-293.
90. Haselgrove JC, Moore JR (1996) Correction for distortion of echo-planar images used to calculate the apparent diffusion coefficient. *Magn Reson Med* 36:960-964.
91. Helms G (2001) Volume correction for edema in single-volume proton MR spectroscopy of contrast-enhancing multiple sclerosis lesions. *Magnetic resonance in medicine : official journal of the Society of Magnetic Resonance in Medicine / Society of Magnetic Resonance in Medicine* 46:256-263.
92. Henkelman RM, Huang X, Xiang QS, Stanisz GJ, Swanson SD, Bronskill MJ (1993) Quantitative interpretation of magnetization transfer. *Magn Reson Med* 29:759-766.
93. Henkelman RM, Stanisz GJ, Graham SJ (2001) Magnetization transfer in MRI: a review. *NMR Biomed* 14:57-64.
94. Herbert MR, Ziegler DA, Makris N, Filipek PA, Kemper TL, Normandin JJ, Sanders HA, Kennedy DN, Caviness VS, Jr. (2004) Localization of white matter volume increase in autism and developmental language disorder. *Ann Neurol* 55:530-540.

95. Herculano-Houzel S (2009) The human brain in numbers: a linearly scaled-up primate brain. *Frontiers in Human Neuroscience* 3.
96. Hildebrand C, Hahn R (1978) Relation between myelin sheath thickness and axon size in spinal cord white matter of some vertebrate species. *Journal of the Neurological Sciences* 38:421-434.
97. Hildebrand C, Remahl S, Persson H, Bjartmar C (1993) Myelinated nerve fibres in the CNS. *Progress in Neurobiology* 40:319-384.
98. Hodgkin AL, Huxley AF (1952) A quantitative description of membrane current and its application to conduction and excitation in nerve. *J Physiol* 117:500-544.
99. Holdsworth SJ, Skare S, Newbould RD, Guzman R, Blevins NH, Bammer R (2008) Readout-segmented EPI for rapid high resolution diffusion imaging at 3T. *European journal of radiology* 65:36-46.
100. Horsfield MA (2005) Magnetization transfer imaging in multiple sclerosis. *J Neuroimaging* 15:58S-67S.
101. Hukkanen V, Roytta M (1987) Autolytic changes of human white matter: an electron microscopic and electrophoretic study. *Exp Mol Pathol* 46:31-39.
102. Huppi PS, Warfield S, Kikinis R, Barnes PD, Zientara GP, Jolesz FA, Tsuji MK, Volpe JJ (1998) Quantitative magnetic resonance imaging of brain development in premature and mature newborns. *Ann Neurol* 43:224-235.
103. Huttenlocher PR, Dabholkar AS (1997) Regional differences in synaptogenesis in human cerebral cortex. *J Comp Neurol* 387:167-178.
104. Jensen JH, Helpert JA, Ramani A, Lu H, Kaczynski K (2005) Diffusional kurtosis imaging: the quantification of non-gaussian water diffusion by means of magnetic resonance imaging. *Magn Reson Med* 53:1432-1440.

105. Jezzard P, Barnett AS, Pierpaoli C (1998) Characterization of and correction for eddy current artifacts in echo planar diffusion imaging. *Magn Reson Med* 39:801-812.
106. Jones CK, Xiang QS, Whittall KP, MacKay AL (2004) Linear combination of multiecho data: short T2 component selection. *Magn Reson Med* 51:495-502.
107. Just MA, Cherkassky VL, Keller TA, Kana RK, Minshew NJ (2007) Functional and anatomical cortical underconnectivity in autism: evidence from an FMRI study of an executive function task and corpus callosum morphometry. *Cereb Cortex* 17:951-961.
108. Kadah YM, Hu X (1997) Simulated phase evolution rewinding (SPHERE): a technique for reducing B0 inhomogeneity effects in MR images. *Magn Reson Med* 38:615-627.
109. Kagan J, Herschkowitz EC (2005) *A young mind in a growing brain*. Mahwah, NJ: Lawrence Erlbaum.
110. Kandel ER, Schwartz JH, Jessell TM (2000) *Principles of Neuroscience*. New York: McGraw-Hill Professional.
111. Kilby PM, Bolas NM, Radda GK (1991) ³¹P-NMR study of brain phospholipid structures in vivo. *Biochim Biophys Acta* 1085:257-264.
112. Kim DH, Adalsteinsson E, Spielman DM (2003) Simple analytic variable density spiral design. *Magn Reson Med* 50:214-219.
113. Kirschner DA, Caspar DLD, Schoenborn BP, Nunes AC (1975) Neutron diffraction studies of nerve myelin. *Brookhaven Symp Biol* 27:III-68.

114. Klugmann M, Schwab MH, Pühlhofer A, Schneider A, Zimmermann F, Griffiths IR, Nave K-A (1997) Assembly of CNS Myelin in the Absence of Proteolipid Protein. *Neuron* 18:59-70.
115. Knauss R, Fleischer G, Grunder W, Karger J, Werner A (1996) Pulsed field gradient NMR and nuclear magnetic relaxation studies of water mobility in hydrated collagen II. *Magn Reson Med* 36:241-248.
116. Koshino H, Carpenter PA, Minshew NJ, Cherkassky VL, Keller TA, Just MA (2005) Functional connectivity in an fMRI working memory task in high-functioning autism. *Neuroimage* 24:810-821.
117. Labadie C, Ott DV, Jochimsen TH, Lee J-H, Möller HE (2008) Comparison of Myelin Water Fraction in Cross-Regularized T1-Relaxograms of Normal White Matter at 3T and 7T and of Normal-Appearing White Matter at 3T. Proceedings of the 16th Annual Meeting of ISMRM, Toronto, Canada 14376.
118. Lainhart JE, Piven J, Wzorek M, Landa R, Santangelo SL, Coon H, Folstein SE (1997) Macrocephaly in children and adults with autism. *J Am Acad Child Adolesc Psychiatry* 36:282-290.
119. Langevin P (1908) Sur la théorie du mouvement brownien. *Comptes Rendus Acad d Sci, Paris* 147:530-533.
120. Laule C, Leung E, Lis DK, Traboulsee AL, Paty DW, MacKay AL, Moore GR (2006) Myelin water imaging in multiple sclerosis: quantitative correlations with histopathology. *Mult Scler* 12:747-753.
121. Laule C, Vavasour IM, Kolind SH, Li DK, Traboulsee TL, Moore GR, MacKay AL (2007) Magnetic resonance imaging of myelin. *Neurotherapeutics* 4:460-484.
122. Laule C, Vavasour IM, Moore GR, Oger J, Li DK, Paty DW, MacKay AL (2004) Water content and myelin water fraction in multiple sclerosis. A T2 relaxation study. *J Neurol* 251:284-293.

123. Lauterbur PC (1973) Image Formation by Induced Local Interactions: Examples Employing Nuclear Magnetic Resonance. *Nature* 242:190-191.
124. Lee JE, Bigler ED, Alexander AL, Lazar M, DuBray MB, Chung MK, Johnson M, Morgan J, Miller JN, McMahon WM, Lu J, Jeong EK, Lainhart JE (2007) Diffusion tensor imaging of white matter in the superior temporal gyrus and temporal stem in autism. *Neurosci Lett* 424:127-132.
125. Liu C, Bammer R, Acar B, Moseley ME (2004a) Characterizing non-gaussian diffusion by using generalized diffusion tensors. *Magnet Reson Med* 51:924-937.
126. Liu C, Bammer R, Kim DH, Moseley ME (2004b) Self-navigated interleaved spiral (SNAILS): application to high-resolution diffusion tensor imaging. *Magn Reson Med* 52:1388-1396.
127. Liu C, Mang SC, Moseley ME (2010) In vivo generalized diffusion tensor imaging (GDTI) using higher-order tensors (HOT). *Magn Reson Med* 63:243-252.
128. Liu C, Moseley ME, Bammer R (2005a) Simultaneous Off-Resonance and Phase Correction for Multi-Shot DWI. Proceedings of the 13th Annual Meeting of ISMRM, Miami, Florida.
129. Liu C, Moseley ME, Bammer R (2005b) Simultaneous phase correction and SENSE reconstruction for navigated multi-shot DWI with non-cartesian k-space sampling. *Magnet Reson Med* 54:1412-1422.
130. Ljunggren S (1983) A simple graphical representation of fourier-based imaging methods. *Journal of Magnetic Resonance* 54:338-343.
131. Ma X, Kadah YM, LaConte SM, Hu X (2004) Enhancing measured diffusion anisotropy in gray matter by eliminating CSF contamination with FLAIR. *Magn Reson Med* 51:423-427.

132. MacKay A, Whittall K, Adler J, Li D, Paty D, Graeb D (1994) In vivo visualization of myelin water in brain by magnetic resonance. *Magn Reson Med* 31:673-677.
133. Mansfield P (1977) Multi-planar image formation using NMR spin echoes. *Journal of Physics C: Solid State Physics* 10:L55-L58.
134. Maxwell JC (1867) On the Dynamical Theory of Gases. *Philosophical Transactions of the Royal Society of London* 157:49-88.
135. McCulloch WS, Pitts W (1990) A logical calculus of the ideas immanent in nervous activity. 1943. *Bull Math Biol* 52:99-115; discussion 173-197.
136. Meiboom S, Gill D (1958) Modified Spin-Echo Method for Measuring Nuclear Relaxation Times. *Review of Scientific Instruments* 29:688-691.
137. Merboldt K-D, Hanicke W, Frahm J (1985) Self-diffusion NMR imaging using stimulated echoes. *Journal of Magnetic Resonance* (1969) 64:479-486.
138. Miller JH, McKinstry RC, Philip JV, Mukherjee P, Neil JJ (2003) Diffusion-tensor MR imaging of normal brain maturation: a guide to structural development and myelination. *AJR Am J Roentgenol* 180:851-859.
139. Miller KL, Pauly JM (2003) Nonlinear phase correction for navigated diffusion imaging. *Magn Reson Med* 50:343-353.
140. Min Y, Kristiansen K, Boggs JM, Husted C, Zasadzinski JA, Israelachvili J (2009) Interaction forces and adhesion of supported myelin lipid bilayers modulated by myelin basic protein. *Proc Natl Acad Sci U S A* 106:3154-3159.
141. Morell P, Quarles RH (1999) Myelin Formation, Structure and Biochemistry. In: *Basic Neurochemistry: Molecular, Cellular and Medical Aspects*, (Siegel, G. J. et al., eds) Philadelphia: Lippincott-Raven.

142. Mori S, Crain BJ, Chacko VP, van Zijl PC (1999) Three-dimensional tracking of axonal projections in the brain by magnetic resonance imaging. *Ann Neurol* 45:265-269.
143. Mori S, van Zijl PC (2002) Fiber tracking: principles and strategies - a technical review. *NMR Biomed* 15:468-480.
144. Mori S, Zhang J (2006) Principles of diffusion tensor imaging and its applications to basic neuroscience research. *Neuron* 51:527-539.
145. Moseley M (2002) Diffusion tensor imaging and aging - a review. *NMR Biomed* 15:553-560.
146. Mukherjee P, McKinstry RC (2006) Diffusion tensor imaging and tractography of human brain development. *Neuroimaging Clin N Am* 16:19-43, vii.
147. Mukherjee P, Miller JH, Shimony JS, Conturo TE, Lee BC, Almlí CR, McKinstry RC (2001) Normal brain maturation during childhood: developmental trends characterized with diffusion-tensor MR imaging. *Radiology* 221:349-358.
148. Mukherjee P, Miller JH, Shimony JS, Philip JV, Nehra D, Snyder AZ, Conturo TE, Neil JJ, McKinstry RC (2002) Diffusion-tensor MR imaging of gray and white matter development during normal human brain maturation. *AJNR Am J Neuroradiol* 23:1445-1456.
149. Mulkern RV, Vajapeyam S, Haker SJ, Maier SE (2005) Magnetization transfer studies of the fast and slow tissue water diffusion components in the human brain. *NMR Biomed* 18:186-194.
150. Murre JM, Sturdy DP (1995) The connectivity of the brain: multi-level quantitative analysis. *Biol Cybern* 73:529-545.

151. Nagy Z, Westerberg H, Klingberg T (2004) Maturation of White Matter is Associated with the Development of Cognitive Functions during Childhood. *Journal of Cognitive Neuroscience* 16:1227-1233.

152. Nave KA (1994) Neurological mouse mutants and the genes of myelin. *Journal of Neuroscience Research* 38:607-612.

153. Nelson C, Collins ML (2008) *Handbook of developmental cognitive neuroscience*. Cambridge, MA: MIT Press.

154. Niendorf T, Dijkhuizen RM, Norris DG, van Lookeren Campagne M, Nicolay K (1996) Biexponential diffusion attenuation in various states of brain tissue: implications for diffusion-weighted imaging. *Magn Reson Med* 36:847-857.

155. Noll DC, Pauly JM, Meyer CH, Nishimura DG, Macovski A (1992) Deblurring for non-2D Fourier transform magnetic resonance imaging. *Magn Reson Med* 25:319-333.

156. Nomura Y, Sakuma H, Takeda K, Tagami T, Okuda Y, Nakagawa T (1994) Diffusional anisotropy of the human brain assessed with diffusion-weighted MR: relation with normal brain development and aging. *AJNR Am J Neuroradiol* 15:231-238.

157. Norris DG, Börnert P, Reese T, Leibfritz D (1992) On the application of ultra-fast rare experiments. *Magnet Reson Med* 27:142-164.

158. Novak N, Bar V, Sabanay H, Frechter S, Jaegle M, Snapper SB, Meijer D, Peles E (2011) N-WASP is required for membrane wrapping and myelination by Schwann cells. *The Journal of Cell Biology* 192:243-250.

159. Ohm GS (1827) *Die galvanische Kette [microform] : mathematisch bearbeitet / von G.S. Ohm*. Berlin :: T.H. Riemann.

160. Ozarslan E, Mareci TH (2003) Generalized diffusion tensor imaging and analytical relationships between diffusion tensor imaging and high angular resolution diffusion imaging. *Magn Reson Med* 50:955-965.
161. Padrón R, Mateu L, Kirschner DA (1979) X-ray diffraction study of the kinetics of myelin lattice swelling. Effect of divalent cations. *Biophysical journal* 28:231-239.
162. Peled S (2000) Water diffusion, T(2) and compartmentation in frog sciatic nerve. *Magn Reson Med* 43:620.
163. Peled S, Cory DG, Raymond SA, Kirschner DA, Jolesz FA (1999) Water diffusion, T(2), and compartmentation in frog sciatic nerve. *Magn Reson Med* 42:911-918.
164. Peng SS, Lee WT, Wang YH, Huang KM (2004) Cerebral diffusion tensor images in children with tuberous sclerosis: a preliminary report. *Pediatr Radiol* 34:387-392.
165. Perrin J (1908) La loi de Stokes et le mouvement brownien. *Comptes Rendus Acad d Sci, Paris* 147:475-476.
166. Pezolet M, Georgescauld D (1985) Raman-Spectroscopy of Nerve-Fibers - a Study of Membrane-Lipids under Steady-State Conditions. *Biophysical Journal* 47:367-372.
167. Pfefferbaum A, Mathalon DH, Sullivan EV, Rawles JM, Zipursky RB, Lim KO (1994) A quantitative magnetic resonance imaging study of changes in brain morphology from infancy to late adulthood. *Arch Neurol* 51:874-887.
168. Pfefferbaum A, Sullivan EV, Hedehus M, Lim KO, Adalsteinsson E, Moseley M (2000) Age-related decline in brain white matter anisotropy measured with spatially corrected echo-planar diffusion tensor imaging. *Magn Reson Med* 44:259-268.

169. Pike GB (1997) Magnetization transfer imaging of multiple sclerosis. *Ital J Neurol Sci* 18:359-365.
170. Polleux F, Lauder JM (2004) Toward a developmental neurobiology of autism. *Ment Retard Dev Disabil Res Rev* 10:303-317.
171. Poon CS, Henkelman RM (1992) Practical T2 quantitation for clinical applications. *J Magn Reson Imaging* 2:541-553.
172. Pruessmann KP, Weiger M, Scheidegger MB, Boesiger P (1999) SENSE: sensitivity encoding for fast MRI. *Magn Reson Med* 42:952-962.
173. Purcell EM, Torrey HC, Pound RV (1946) Resonance Absorption by Nuclear Magnetic Moments in a Solid. *Physical Review* 69:37.
174. Rabi II (1937) Space Quantization in a Gyration Magnetic Field. *Physical Review* 51:652.
175. Rane S, Nair G, Duong TQ (2010) DTI at long diffusion time improves fiber tracking. *NMR Biomed* 23:459-465.
176. Ranvier L-A (1878) *Leçons sur l'histologie du système nerveux*, par M. L. Ranvier, recueillies par M. Ed. Weber. Paris.
177. Reese TG, Heid O, Weisskoff RM, Wedeen VJ (2003a) Reduction of eddy-current-induced distortion in diffusion MRI using a twice-refocused spin echo. *Magn Reson Med* 49:177-182.
178. Reese TG, Heid O, Weisskoff RM, Wedeen VJ (2003b) Reduction of eddy-current-induced distortion in diffusion MRI using a twice-refocused spin echo. *Magn Reson Med* 49:177-182.

179. Reynolds RJ, Little GJ, Lin M, Heath JW (1994) Imaging myelinated nerve fibres by confocal fluorescence microscopy: individual fibres in whole nerve trunks traced through multiple consecutive internodes. *J Neurocytol* 23:555-564.
180. Ritchie JM, Rogart RB (1977) Density of sodium channels in mammalian myelinated nerve fibers and nature of the axonal membrane under the myelin sheath. *Proc Natl Acad Sci U S A* 74:211-215.
181. Roemer PB, Edelstein WA, Hayes CE, Souza SP, Mueller OM (1990) The NMR phased array. *Magn Reson Med* 16:192-225.
182. Ronen I, Moeller S, Ugurbil K, Kim DS (2006) Investigation of multicomponent diffusion in cat brain using a combined MTC-DWI approach. *Magn Reson Imaging* 24:425-431.
183. Sakuma H, Nomura Y, Takeda K, Tagami T, Nakagawa T, Tamagawa Y, Ishii Y, Tsukamoto T (1991) Adult and neonatal human brain: diffusional anisotropy and myelination with diffusion-weighted MR imaging. *Radiology* 180:229-233.
184. Salat DH, Tuch DS, Greve DN, van der Kouwe AJ, Hevelone ND, Zaleta AK, Rosen BR, Fischl B, Corkin S, Rosas HD, Dale AM (2005) Age-related alterations in white matter microstructure measured by diffusion tensor imaging. *Neurobiol Aging* 26:1215-1227.
185. Schick F (1997) SPLICE: Sub-second diffusion-sensitive MR imaging using a modified fast spin-echo acquisition mode. *Magnet Reson Med* 38:638-644.
186. Schmierer K, Tozer DJ, Scaravilli F, Altmann DR, Barker GJ, Tofts PS, Miller DH (2007) Quantitative magnetization transfer imaging in postmortem multiple sclerosis brain. *J Magn Reson Imaging* 26:41-51.
187. Schmithorst VJ, Wilke M, Dardzinski BJ, Holland SK (2002) Correlation of white matter diffusivity and anisotropy with age during childhood and adolescence: a cross-sectional diffusion-tensor MR imaging study. *Radiology* 222:212-218.

188. Shen Y, Larkman DJ, Counsell S, Pu IM, Edwards D, Hajnal JV (2004) Correction of high-order eddy current induced geometric distortion in diffusion-weighted echo-planar images. *Magn Reson Med* 52:1184-1189.
189. Skudlarski P, Jagannathan K, Calhoun VD, Hampson M, Skudlarska BA, Pearlson G (2008) Measuring brain connectivity: Diffusion tensor imaging validates resting state temporal correlations. *Neuroimage* 43:554-561.
190. Sodickson DK, Manning WJ (1997) Simultaneous acquisition of spatial harmonics (SMASH): fast imaging with radiofrequency coil arrays. *Magn Reson Med* 38:591-603.
191. Song AW, Wong EC, Hyde JS (1994) Echo-volume imaging. *Magn Reson Med* 32:668-671.
192. Song SK, Sun SW, Ju WK, Lin SJ, Cross AH, Neufeld AH (2003) Diffusion tensor imaging detects and differentiates axon and myelin degeneration in mouse optic nerve after retinal ischemia. *Neuroimage* 20:1714-1722.
193. Song SK, Sun SW, Ramsbottom MJ, Chang C, Russell J, Cross AH (2002) Dysmyelination revealed through MRI as increased radial (but unchanged axial) diffusion of water. *Neuroimage* 17:1429-1436.
194. Stanisz GJ, Henkelman RM (1998) Diffusional anisotropy of T2 components in bovine optic nerve. *Magn Reson Med* 40:405-410.
195. Stanisz GJ, Kecojevic A, Bronskill MJ, Henkelman RM (1999) Characterizing white matter with magnetization transfer and T(2). *Magn Reson Med* 42:1128-1136.
196. Stanisz GJ, Odrobina EE, Pun J, Escaravage M, Graham SJ, Bronskill MJ, Henkelman RM (2005) T1, T2 relaxation and magnetization transfer in tissue at 3T. *Magn Reson Med* 54:507-512.

197. Stankoff B, Wang Y, Bottlaender M, Aigrot MS, Dolle F, Wu C, Feinstein D, Huang GF, Semah F, Mathis CA, Klunk W, Gould RM, Lubetzki C, Zalc B (2006) Imaging of CNS myelin by positron-emission tomography. *Proc Natl Acad Sci U S A* 103:9304-9309.
198. Stejskal EO, Tanner JE (1965) Spin Diffusion Measurements: Spin Echoes in the Presence of a Time-Dependent Field Gradient. *The Journal of Chemical Physics* 42:288-292.
199. Stevenson RE, Schroer RJ, Skinner C, Fender D, Simensen RJ (1997) Autism and macrocephaly. *Lancet* 349:1744-1745.
200. Stokes SGG (1850) On the effect of the internal friction of fluids on the motion of pendulums. *Trans of the Cambridge Phil Soc* IX:8-48.
201. Sundaram SK, Kumar A, Makki MI, Behen ME, Chugani HT, Chugani DC (2008) Diffusion tensor imaging of frontal lobe in autism spectrum disorder. *Cereb Cortex* 18:2659-2665.
202. Suzuki Y, Matsuzawa H, Kwee IL, Nakada T (2003) Absolute eigenvalue diffusion tensor analysis for human brain maturation. *NMR Biomed* 16:257-260.
203. Swift TJ, Fritz OG, Jr. (1969) A proton spin-echo study of the state of water in frog nerves. *Biophys J* 9:54-59.
204. Torrey HC (1956) Bloch Equations with Diffusion Terms. *Physical Review* 104:563.
205. Trapp B, Kidd G (2004) Structure of the myelinated axon. In: *Myelin Biology and Disorders*(Lazzarini, R., ed), pp 3-24 London, UK: Elsevier Academic.
206. Travis AR, Does MD (2005) Selective excitation of myelin water using inversion-recovery-based preparations. *Magn Reson Med* 54:743-747.

207. Truong TK, Chen B, Song AW (2008) Integrated SENSE DTI with correction of susceptibility- and eddy current-induced geometric distortions. *Neuroimage* 40:53-58.
208. Tuch DS (2004) Q-ball imaging. *Magn Reson Med* 52:1358-1372.
209. Tuch DS, Reese TG, Wiegell MR, Makris N, Belliveau JW, Wedeen VJ (2002) High angular resolution diffusion imaging reveals intravoxel white matter fiber heterogeneity. *Magnet Reson Med* 48:577-582.
210. Tuch DS, Reese TG, Wiegell MR, Wedeen VJ (2003) Diffusion MRI of complex neural architecture. *Neuron* 40:885-895.
211. Tuch DS, Wisco JJ, Khachaturian MH, Ekstrom LB, Kotter R, Vanduffel W (2005) Q-ball imaging of macaque white matter architecture. *Philos Trans R Soc Lond B Biol Sci* 360:869-879.
212. Twieg DB (1983) The k-trajectory formulation of the NMR imaging process with applications in analysis and synthesis of imaging methods. *Medical Physics* 10:610-621.
213. Upadhyay J, Hallock K, Erb K, Kim DS, Ronen I (2007) Diffusion properties of NAA in human corpus callosum as studied with diffusion tensor spectroscopy. *Magn Reson Med* 58:1045-1053.
214. van der Knaap MS, Valk J (1995) *Magnetic Resonance of Myelin, Myelination, and Myelin Disorders*. Berlin: Springer.
215. van Dusschoten D, Moonen CT, de Jager PA, Van As H (1996) Unraveling diffusion constants in biological tissue by combining Carr-Purcell-Meiboom-Gill imaging and pulsed field gradient NMR. *Magn Reson Med* 36:907-913.

216. Vargas ME, Barres BA (2007) Why Is Wallerian Degeneration in the CNS So Slow? *Annual Review of Neuroscience* 30:153-179.
217. Vasilescu V, Katona E, Simplaceanu V, Demco D (1978) Water Compartments in Myelinated Nerve .3. Pulsed Nmr Results. *Experientia* 34:1443-1444.
218. Vidarsson L, Conolly SM, Lim KO, Gold GE, Pauly JM (2005) Echo time optimization for linear combination myelin imaging. *Magn Reson Med* 53:398-407.
219. Villringer A, Planck J, Hock C, Schleinkofer L, Dirnagl U (1993) Near infrared spectroscopy (NIRS): a new tool to study hemodynamic changes during activation of brain function in human adults. *Neurosci Lett* 154:101-104.
220. Virchow RLC (1854) Über das ausgebreitete Vorkommen einer dem Nervenmark analogen Substanz in den tierischen Geweben. *Virchows Arch Pathol Anat* 6:562-572.
221. von Smoluchowski M (1906) Zur kinetischen Theorie der Brownschen Molekularbewegung und der Suspensionen. *Annalen der Physik* 326:756-780.
222. Waldman A, Rees JH, Brock CS, Robson MD, Gatehouse PD, Bydder GM (2003) MRI of the brain with ultra-short echo-time pulse sequences. *Neuroradiology* 45:887-892.
223. Wang C, Popescu DC, Wu C, Zhu J, Macklin W, Wang Y (2010) In situ fluorescence imaging of myelination. *J Histochem Cytochem* 58:611-621.
224. Wang HF, Fu Y, Zickmund P, Shi RY, Cheng JX (2005) Coherent anti-stokes Raman scattering imaging of axonal myelin in live spinal tissues. *Biophysical Journal* 89:581-591.
225. Webb S, Munro CA, Midha R, Stanisz GJ (2003) Is multicomponent T2 a good measure of myelin content in peripheral nerve? *Magn Reson Med* 49:638-645.

226. Wedeen VJ, Hagmann P, Tseng WY, Reese TG, Weisskoff RM (2005) Mapping complex tissue architecture with diffusion spectrum magnetic resonance imaging. *Magn Reson Med* 54:1377-1386.
227. Wedeen VJ, Wang RP, Schmahmann JD, Benner T, Tseng WY, Dai G, Pandya DN, Hagmann P, D'Arceuil H, de Crespigny AJ (2008) Diffusion spectrum magnetic resonance imaging (DSI) tractography of crossing fibers. *Neuroimage* 41:1267-1277.
228. Wessig C, Bendszus M, Stoll G (2007) In vivo visualization of focal demyelination in peripheral nerves by gadofluorine M-enhanced magnetic resonance imaging. *Exp Neurol* 204:14-19.
229. Whittall KP, MacKay AL (1989) Quantitative interpretation of NMR relaxation data. *Journal of Magnetic Resonance (1969)* 84:134-152.
230. Whittall KP, MacKay AL, Graeb DA, Nugent RA, Li DK, Paty DW (1997a) In vivo measurement of T2 distributions and water contents in normal human brain. *Magn Reson Med* 37:34-43.
231. Whittall KP, Mackay AL, Graeb DA, Nugent RA, Li DKB, Paty DW (1997b) In vivo measurement of T2 distributions and water contents in normal human brain. *Magnet Reson Med* 37:34-43.
232. Wolff SD, Balaban RS (1989) Magnetization transfer contrast (MTC) and tissue water proton relaxation in vivo. *Magn Reson Med* 10:135-144.
233. Wu C, Wang C, Popescu DC, Zhu W, Somoza EA, Zhu J, Condie AG, Flask CA, Miller RH, Macklin W, Wang Y (2010) A novel PET marker for in vivo quantification of myelination. *Bioorg Med Chem* 18:8592-8599.
234. Yankelov PI, Lecours AR (1967) The Myelogenetic cycles of regional maturation of the brain. In: *Regional development of the brain in early life*(Minkowski, A., ed) Philadelphia, PA: F. A. Davis Co.

Biography

Alexandru Vlad Avram was born on August 15, 1983 in Arad, Romania. He was raised by his parents Elisabeta and Iancu, and grew up along with his twin brother Sorin. After attending German primary school, he moved to Arad to enroll in Moise Nicoara High School where he took a strong interest in mathematics and physics. Alexandru won 6 Prizes at the Romanian National Mathematics Olympiad and numerous other awards in physics, chemistry and literature.

In 2002, he immigrated to the US to pursue his undergraduate studies at Duke University. Alexandru earned a Bachelor's degree in Biomedical Engineering and Electrical Engineering in May 2006. During his undergraduate studies, Alexandru worked in Dr. Scott Huettel's lab at the Brain Imaging and Analysis Center (BIAC) where he developed a strong curiosity in understanding how the brain works. After graduation, he continued his research working with Dr. Allen Song, director of BIAC at the Duke University Medical Center. In his Master's research project Alexandru investigated the possibility of detecting neuronal currents in ionic solutions using MRI, and co-authored a paper in the Journal of Magnetic Resonance.

In the following years he directed his efforts towards improving the clinical utility of diffusion tensor imaging (DTI) by sensitizing the measurement to myelin water. Alexandru became a student member of the International Society for Magnetic Resonance in Medicine (ISMRM) and was invited to present his work in numerous oral

and traditional posters at yearly conferences. Alexandru's research and collaborative projects have been published in Neuroimage and Magnetic Resonance in Medicine.

After receiving his Ph.D. in Biomedical Engineering, Alexandru will pursue a postdoctoral fellowship in neuroimaging, working with Dr. Peter Basser at the National Institute of Health.